PASSIVE RESONANT COIL BASED FAST REGISTRATION AND TRACKING SYSTEM FOR REAL-TIME MRI-GUIDED MINIMALLY INVASIVE SURGERY

by

Yunzhao Ma

A Thesis Submitted to the Graduate School of Worcester Polytechnic Institute
In Partial Fulfillment of the Requirements for the Degree of
Master of Science in Biomedical Engineering

May, 2013

Approved:

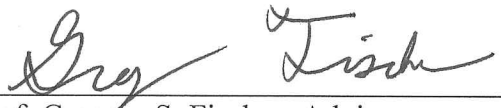

Prof. Gregory S. Fischer, Advisor

Prof. John M. Sullivan, Associate Head of ME Department

Prof. Glenn R. Gaudette, Committee Member

PASSIVE RESONANT COIL BASED FAST REGISTRATION AND TRACKING SYSTEM FOR REAL-TIME MRI-GUIDED MINIMALLY INVASIVE SURGERY

by

Yunzhao Ma

A Thesis Submitted to the Graduate School of Worcester Polytechnic Institute
In Partial Fulfillment of the Requirements for the Degree of
Master of Science in Biomedical Engineering

May, 2013

Approved:

_____
Prof. Gregory S. Fischer, Advisor

_____
Prof. John M. Sullivan, Associate Head of ME Department

_____
Prof. Glenn R. Gaudette, Committee Member

Abstract

This thesis presents a single-slice based fast stereotactic registration and tracking technique along with a corresponding modular system for guiding robotic mechanism or interventional instrument to perform needle-based interventions under live MRI guidance. The system can provide tracking of full 6 degree-of-freedom (DOF) in stereotactic interventional surgery based upon a single, rapidly acquired cross-sectional image. The whole system is constructed with a modular data transmission software framework and mechanical structure so that it supports remote supervision and manipulation between a 3D Matlab tracking user interface (UI) and an existing MRI robot controller by using the OpenIGTLink network communication protocol. It provides better closed-loop control by implementing a feedback output interface to the MRI-guided robot.

A new compact fiducial frame design is presented, and the fiducial is wrapped with a passive resonant coil. The coil resonates at the Larmor frequency for 3T MRI to enhance signal strength and enable for rapid imaging. The fiducial can be attached near the distal end of the robot and coaxially with a needle so as to visualize target tissue and track the surgical tool synchronously. The MRI-compatible design of fiducial frame, robust tracking algorithm and modular interface allow this tracking system to be conveniently used on different robots or devices and in different size of MRI bores.

Several iterations of the tracking fiducial and passive resonant coils were constructed and evaluated in a Phillips Achieva 3T MRI. To assess accuracy and robustness of the tracking algorithm, 25 groups of images with different poses were successively scanned along specific sequence in and MRI experiment. The translational RMS error along depth is 0.271mm with standard deviation of

0.277mm for a total of 100 samples. The overall angular RMS error is less than 0.426° with standard deviation of 0.526° for a total of 150 samples. The passive resonant coils were shown to significantly increase signal intensity in the fiducial relative to the surroundings and provide for rapid imaging with low flip angles.

Keywords

MRI guided intervention

Stereotactic surgery

Image based registration and tracking

Minimally invasive surgery

Passive imaging coil

Acknowledgments

First and foremost, I would like to thank my thesis advisor and AIM lab director Prof. Gregory S. Fischer. He provided me a liberal academic atmosphere and amazing research conditions. His advice and encouragement inspired me from time to time to reach my goals; his patience and able guidance have given me knowledge; his trust in me has furnished the necessary confidence in myself. I consider myself to be very fortunate to have him as my advisor.

I also would like to extend my grateful thanks to Prof. Glenn R. Gaudette and Prof. John M. Sullivan reading my thesis and serving on defense committee members. I would like to thank my lab mates for collaborative work, friendship and for sharing days and nights with me in the lab. In no particular order, I would like to thank Hao Su, Weijian Shang, Gang Li, Wenzhi Ji, Alex Camilo, Kevin Harrington, Satyanarayana Janga and Michael Delph. I also want to acknowledge Ivo Dobrev in the adjacent lab.

Special thanks for Prof. Reinhold Ludwig for using some of his lab's facilities. I express my gratitude to the members of University of Massachusetts Medical School, Department of Radiology who tolerate all my amateur ways and guided me many times. In particular, I would like to thank physicist Shaokuan Zheng in Advance MRI Center.

Words are not enough to express the depth of my gratitude to my wife and parents. You gave me everything I wanted, even before I asked for it, so that I always feel being covered with your love. You put up with my tantrums; you overcome the jet lag staying with me online on the other side of the planet; you did everything possible to make me feel no more loneliness on my bleakest possible day. It's your blessings that made me accomplish all that I did.

Thank you all, for everything!

Finally, this work was supported in part by the Congressionally Directed Medical Research Programs Prostate Cancer Research Program New Investigator Award W81XWH-09-1-0191, NIH Bioengineering Research Partnership 1R01CA111288-01A1, and WPI Backlin Scholarship Committee.

Contents

ABSTRACT ..... **II**

KEYWORDS ..... **IV**

ACKNOWLEDGMENTS ..... **V**

CONTENTS ..... **VII**

LIST OF FIGURES ..... **XI**

LIST OF TABLES ..... **XIV**

ACRONYMS ..... **XV**

CHAPTER 1 OVERVIEW **1**

1.1 CLINICAL BACKGROUND 1

1.1.1 Background on MRI-guided Minimally Invasive Surgery 1

1.1.2 Advantages of MRI for MIS 4

1.1.3 Motivation of Registration and Tracking System for MRI-guided Robots 5

1.2 LITERATURE REVIEW 8

1.2.1 Resonant Coil Marker Designs 8

1.2.2 Registration Fiducial Frame Designs 12

1.3 THESIS CONTRIBUTION 16

CHAPTER 2 DESIGN REQUIREMENTS **18**

2.1 MRI COMPATIBILITY 18

2.2 WORKSPACE 19

2.3 HIGH RESONANT FREQUENCY 20

CHAPTER 3 SYSTEM ARCHITECTURE 22

3.1 PANORAMA OF COOPERATION OF REGISTRATION AND TRACKING SYSTEM WITH SURGICAL ROBOT IN MIS 22

3.2 DICOM SEVER MODULE 25

3.3 TRACKING MODULE 25

3.4 USER INTERFACE MODULE 28

3.5 CORRECTION FEEDBACK MODULE 29

3.6 FIDUCIAL FRAME MODULE 29

3.7 DATA TRANSMISSION AND COORDINATION AMONG MODULES 30

CHAPTER 4 FIDUCIAL FRAME DESIGN 31

4.1 ANALYSIS OF INITIAL PROTOTYPE FIDUCIAL DESIGNS 31

4.1.1 Mesh Design of Six Identical Helical Curves 31

4.1.2 Mesh Design of Two Helical Curves and Two Straight Lines 32

4.1.3 Mesh Design of Four Various Gradient Helical Curves 33

4.1.4 Detection Robustness Analysis of Basic Fiducial Prototype Designs 34

4.2 PROPOSED FINAL FIDUCIAL DESIGN 36

4.2.1 Mechanic Structure 36

4.2.2 Manufacturing and Materials Parameters 41

4.3 APPLICATION IN MRI-COMPATIBLE SURGICAL ROBOTS 44

CHAPTER 5 STEREOTACTIC TRACKING METHODS 46

5.1 IMAGE RECOGNITION 46

5.1.1 Centroid Measurement 46

5.1.2 Ellipse Plane Reconstruction 49

5.2 MATHEMATIC MODEL 51

5.2.1 Reference Frame Definitions 51

5.2.2 Calculation of 3 Rotational DOF 52

5.2.3 Calculation of 3 Translational DOF 55
5.2.4 Calculation of Transformation Matrix 57
5.3 SIMULATION VERIFICATION 58
5.3.1 Simulation Method 58
5.3.2 Simulation Results 60
CHAPTER 6 TRACKING EXPERIMENTS AND RESULTS 66
6.1 EXPERIMENTS 66
6.2 ACCURACY ASSESSMENT 70
6.2.1 Evaluation of Translation 70
6.2.2 Evaluation of Rotation 73
6.2.3 Comprehensive Evaluation 75
CHAPTER 7 PASSIVE RESONANT COIL DESIGN 76
7.1 PROOF OF PRINCIPLE 76
7.1.1 Single Coil LC Circuit Implementation 76
7.1.2 MRI Results 78
7.2 ANALYSIS FOR ALTERNATIVE DESIGNS 80
7.2.1 Double Layers Coil with Reversely Wrapping Proposal 80
7.2.2 Interior Sub-coils Prototype 81
7.2.3 Exterior Sub-cols Prototype 83
7.3 FINAL IMPROVED DESIGN 84
7.3.1 Mechanic Structure 84
7.3.2 MRI Results 85
CHAPTER 8 CONCLUSION 88
8.1 SUMMARY OF WORK AND CONTRIBUTIONS 88
8.1.1 Summary 88

8.1.2 Impact and Contribution 89
8.2 FUTURE WORK 90
8.2.1 User Interface Enrichment 91
8.2.2 Fiducial Frame Size Diversification....91
8.2.3 Tracking Algorithm Platform Transplantation....92
BIBLIOGRAPHY....93
CURRICULUM VITA....97
PUBLICATIONS:....97

List of Figures

FIG. 1-1: THE PROTOTYPE ROBOT IN THE BORE OF A 3T MRI SCANNER DEVELOPED 2

FIG. 1-2: MRI-GUIDED SURGERY ROBOTS. 3

FIG. 1-3: MRI-GUIDED SURGICAL APPLICATION OF THE INNOMOTION ROBOTIC SYSTEM. 6

FIG. 1-4: NEUROARM ROBOT DEVELOPED AT UNIVERSITY OF CALGARY 7

FIG. 1-5: THE DIMENSIONS OF PASSIVE SINGLE MICRO-COIL MARKER DESIGN. 9

FIG. 1-6: THE LATEX COIL FORMER FILLS THE COIL. 9

FIG. 1-7: PHOTOGRAPH AND SCHEMATIC OF TUNED FIDUCIAL MARKERS. 10

FIG. 1-8: PHOTOGRAPH OF THE TWO OPPOSED SOLENOID ARRAYS 12

FIG. 1-9: DESIGN AND CROSS-SECTION OF THE Z-FRAME FIDUCIAL TARGET. 13

FIG. 1-10: 3D PRISM DESIGN AND A PLANAR 2D VERSION OF PRISM FIDUCIAL. 14

FIG. 1-11: ELLIPSE DESIGN IN MRI 14

FIG. 1-12: ELLIPSE DESIGN IN FLUOROSCOPY 15

FIG. 2-1: ILLUSTRATION OF LONG AND NARROW WORKSPACE INSIDE PHILLIPS 3T MRI SCANNER 20

FIG. 2-2: LC CIRCUIT SCHEMATIC DIAGRAM 21

FIG. 3-1: SYSTEM ARCHITECTURE AND DATA FLOW OF REGISTRATION AND TRACKING SYSTEM. 23

FIG. 3-2: THE PANORAMA OF REAL-TIME MRI-GUIDED ROBOTIC SURGERY SYSTEM SETTING. 24

FIG. 3-3: DICOM SEVER MODULE INTERIOR DATA FLOW 25

FIG. 3-4: ALGORITHM OF TRACKING MODULE TO DETECT AND LOCALIZE THE FIDUCIAL FRAME 27

FIG. 3-5: THE 3D VISUAL INTERFACE FOR REAL TIME STEREOTACTIC POST TRACKING. 28

FIG. 3-6: CAD DESIGN OF FIDUCIAL FRAME WITH COIL WRAP 30

FIG. 4-1: MESH DESIGN OF FOUR HELICAL CURVES 32

FIG. 4-2: MESH DESIGN OF TWO HELICAL CURVES AND TWO STRAIGHT LINES 33

FIG. 4-3: MESH DESIGN OF FOUR VARIOUS GRADIENT HELICAL CURVES 34

FIG. 4-4: ERROR OF FITTING CAUSED BY THE LACK OF NUMBER OF DETECTED POINTS. 35
FIG. 4-5: CHIC FRAME FIDUCIAL CAD MODEL AND ELLIPTICAL MESH PATTERN IN CROSS-SECTION. 37
FIG. 4-6: VIEW OF THE CHIC FIDUCIAL FRAME 38
FIG. 4-7: THE CAD DRAWING OF CHIC FIDUCIAL FRAME 39
FIG. 4-8: UNIQUE REGISTRATION PATTERN OF TUBULAR MESH. 40
FIG. 4-9: FURTHER DETECTION PROCESS IN THE IMAGE ANALYSIS 41
FIG. 4-10: MR-SPOTS MRI HIGH CONTRAST REGISTRATION FLUID 44
FIG. 4-11: CHIC FRAME FIDUCIAL FRAME INTEGRATED ON WPI AIM LAB'S ROBOTS 45
FIG. 5-1: MRI IMAGE AND CENTROID ESTIMATION OF THE Z-FRAME 47
FIG. 5-2: MRI IMAGE AND CENTROID ESTIMATION OF CHIC FIDUCIAL FRAME 47
FIG. 5-3: CENTROID ESTIMATION FROM GAUSSIAN DISTRIBUTION MODEL AND TRADITIONAL WAY. 49
FIG. 5-4: ELLIPSE PLANE RECONSTRUCTION AFTER IMAGE ANALYSIS 50
FIG. 5-5: REFERENCE FRAME FOR CHIC FIDUCIAL FRAME 52
FIG. 5-6: VIEW OF REFERENCE FRAME FOR ELEVATION AND AZIMUTH ANGLE EVALUATION 52
FIG. 5-7: ILLUSTRATION OF THREE INDIVIDUAL ROTATION STEPS ROTATING. 54
FIG. 5-8: THE ILLUSTRATION OF CORRECTION FROM ARBITRARY CROSS-SECTION TO NORMAL SECTION.. 56
FIG. 5-9: ARTIFICIALLY CREATED CROSS-SECTIONAL IMAGE 58
FIG. 5-10: IMAGES WITH ARTIFICIAL NOISE 58
FIG. 5-11: REGISTRATION OF CENTROIDS AND VARIOUS TYPES OF MARKERS 59
FIG. 5-12: FINAL REGISTRATION AND TRACKING RESULTS 59
FIG. 5-13: SIMULATION POSITIONING ACCURACY EVALUATION 61
FIG. 5-14: SIMULATION ORIENTATION ACCURACY EVALUATION 62
FIG. 5-15: AUTOMATICALLY TRACKING A SERIES OF ELEVATION ANGLE CHANGES. 65
FIG. 6-1: EXPERIMENT SCHEMATIC AND THE REAL INSTALLMENT OF THE WHOLE EXPERIMENT 67
FIG. 6-2: TYPICAL CHIC FIDUCIAL FRAME MR IMAGES AT DIFFERENT TILE AND TWIST ANGLES 69
FIG. 6-3: PRELIMINARY ANALYSIS ABOUT TRANSLATION ACCURACY 71
FIG. 6-4: ERROR MEASUREMENT RESULTS OF TRANSLATION DOF 72
FIG. 6-5: DETECTION OF MOTION IN DEPTH WITH 2MM REGULAR STEP LENGTH ALONG Z AXIS 72

FIG. 6-6: DETECTION OF MOTION IN TWIST ANGLE 73
FIG. 6-7: DETECTION OF MOTION IN ELEVATION ANGLE 74
FIG. 6-8: DETECTION OF MOTION IN DIRECTION ANGLE 74
FIG. 7-1: SINGLE-LAYER COIL AND CORRESPONDING INDUCTANCE APPROXIMATE FORMULA 77
FIG. 7-2: SINGLE COIL LC CIRCUIT WITH 6MM COIL DIAMETER AND 3MM COIL DIAMETER 78
FIG. 7-3: DIAGRAMMATIC DRAWING FOR SINGLE COIL LAYOUT IN MRI EXPERIMENT 79
FIG. 7-4: MR IMAGE OF CONTROL GROUP AND EXTERIOR COIL. 79
FIG. 7-5: AN ARRAY OF SUB-BRIGHT ARTIFACTS APPEARING AROUND REAL SPOT 80
FIG. 7-6: CAD VIEW OF CHIC FIDUCIAL FRAME WITH REVERSELY WRAPPING DOUBLE LAYERS COIL ... 81
FIG. 7-7: CAD DRAWING AND IMPLEMENTATION OF INTERIOR SUB-COILS CHIC FIDUCIAL FRAME 82
FIG. 7-8: CAD DRAWING AND IMPLEMENTATION OF EXTERIOR SUB-COILS CHIC FIDUCIAL FRAME 82
FIG. 7-9: FAST MRI RESULTS OF DIFFERENT COIL WRAPE 83
FIG. 7-10: LATERAL VIEW OF SUB-COIL CHIC FIDUCIAL FRAME 84
FIG. 7-11: TWO DIFFERENT CROSS-SECTIONS OF COIL MATERIALS 84
FIG. 7-12: CAD DRAWING AND IMPLEMENTATION OF IMPROVED EXTERIOR SUB-COILS FIDUCIAL 85
FIG. 7-13: IMPROVED EXTERIOR SUB-COILS CHIC FIDUCIAL FRAME IMAGING 86
FIG. 7-14: QUANTITATIVE ANALYSIS EXPERIMENT FOR IMPROVED EXTERIOR SUB-COILS FIDUCIAL 87
FIG. 7-15: IMAGING INTENSITY DIFFERENCE BETWEEN IMPROVED EXTERIOR SUB-COILS FIDUCIAL 87

List of Tables

TABLE 4-1 SEALANT MATERIALS AND PRODUCTS 42
TABLE 4-2 PERFORMANCE OF VARIOUS SEALING TECHNIQUES AND MATERIALS 43
TABLE 5-1 ORIGINAL MR IMAGE ACCURACY EVALUATION 63
TABLE 5-2 RECONSTRUCTED MRI POSITIONING AND ORIENTATION ACCURACY TEST 64
TABLE 6-1 PHILIPS 3T MRI SCANNER IMAGING PARAMETER 68
TABLE 6-2 25 GROUPS OF DIFFERENT COMBINATION OF TILT ANGLE AND TWIST ANGLE 68
TABLE 6-3 STATISTICAL ANALYSIS OF 6-DOF TRACKING ERRORS 75
TABLE 7-1 FAST LOW ANGLE SHOT (FLASH) PULSE SEQUENCE 78

Acronyms

CAD Computer-aided Design

CHIC Cylindrical Helix Imaging Coordinate

CT Computed Tomography

DBS Deep Brain Stimulation

DLL Dynamic Link Library

DOF Degree of Freedom

FDA Food and Drug Administration

MIS Minimally Invasive Surgery

MRI Magnetic Resonance Imaging

NIH National Institutes of Health

PET Positron Emission Tomography

RF Radio Frequency

RMS Root Mean Square

SNR Signal-to-Noise Ratio

SPECT Single Photon Emission Computed Tomography

US Ultrasound

XCT X-ray Computed Tomography

Chapter 1

Overview

Robot-assisted surgical interventions have been developed rapidly in the last decade, especially in minimally invasive surgery (MIS) [1]. Taking advantage of MRI, which has a high soft-tissue contrast, real-time interventions could be accomplished by image-guided surgical robots [2]. Although robots themself have a high targeting accuracy, how to acquire the position and orientation of a surgical tool with respect to the patient's anatomy is always a crucial challenge [3]. This results a need for highly accurate robot registration and tracking [4].

1.1 Clinical Background

1.1.1 Background on MRI-guided Minimally Invasive Surgery

Recently, MIS technologies have been widely used in clinical trials recently. They decrease the pain experienced by patients during treatment and significantly shorten recovery periods. MIS is an inherently stereotactic problem in many cases of therapy delivery to local lesions such as deep brain stimulation (DBS) [5], breast biopsies [6] and prostate intervention [7]. The effective image-guided methods are desired to facilitate the procedure accurately, which is the key to the efficiency of the therapeutic deliveries [8].

In 1908, Horsley and Clarke reported a frame with external markers that enabled them to assign a Cartesian space coordinate system to a monkey's head for neurological surgery [9]. This frame became known as the Horsley-Clarke stereotactic frame. It is still in use for neurological surgery,

such as DBS. The principles of frame-guided surgery were mainly used for neurosurgery because the skull can provide a rigid frame.

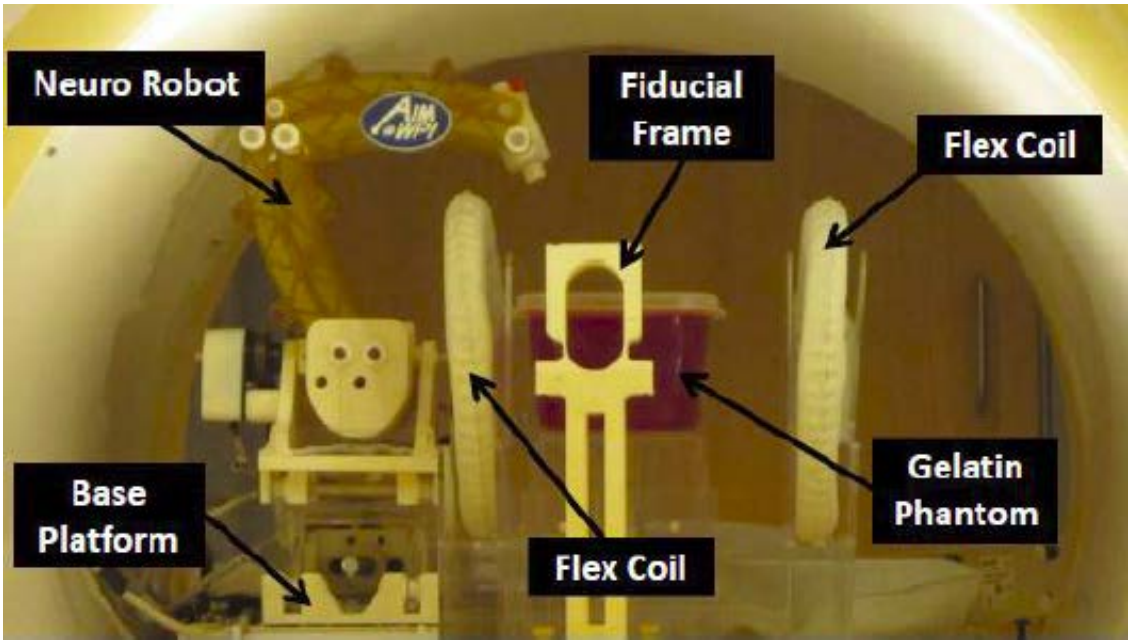

Fig. 1-1: The prototype robot in the bore of a 3T MRI scanner developed at Worcester Polytechnic Institute

With the invention of the MRI and the PC, the frame-guided field has extended to include MRI-guided surgery, which is widely used in neurosurgery, orthopedics, cardiac interventions and prostate interventions. MRI-guided surgeries are one of image-guided medical procedures in which medical images are provided by MRI based systems to assist the physician in precisely visualizing and targeting the surgical area [10]. The implantation of MRI-guided deep brain stimulator has become increasingly popular for movement-disorder surgery [11]. Cole, Wang and Fischer [12,13] designed a 5-DOF MRI-guided stereotactic robot that is kinematically identical to a Leksell frame with a high MRI-compatible control system. Fig. 1-1 shows the prototype robot in the bore of a 3T MRI scanner with phantom. Fischer et al also proposed a MRI-compatible robot system for transperineal prostate needle insertion using pneumatic actuation techniques [14].

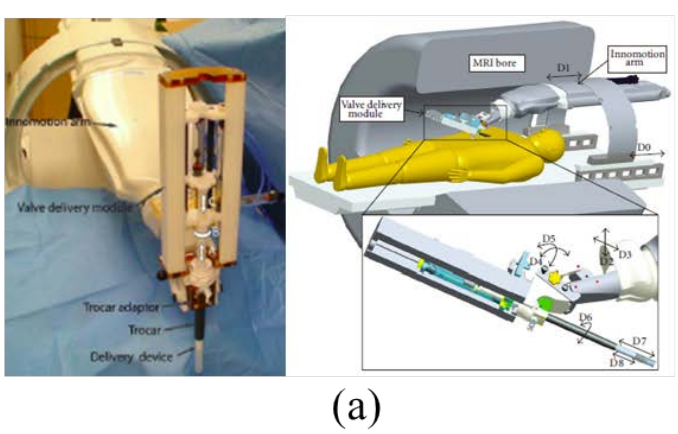

(a)

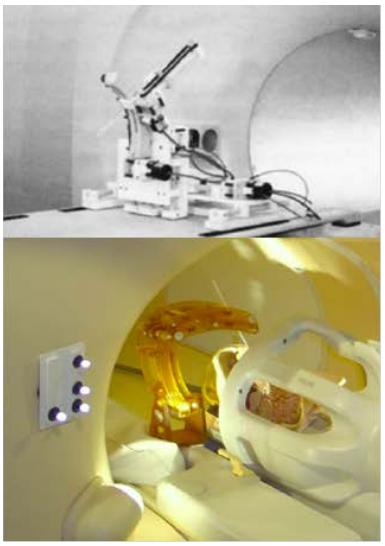

(b)

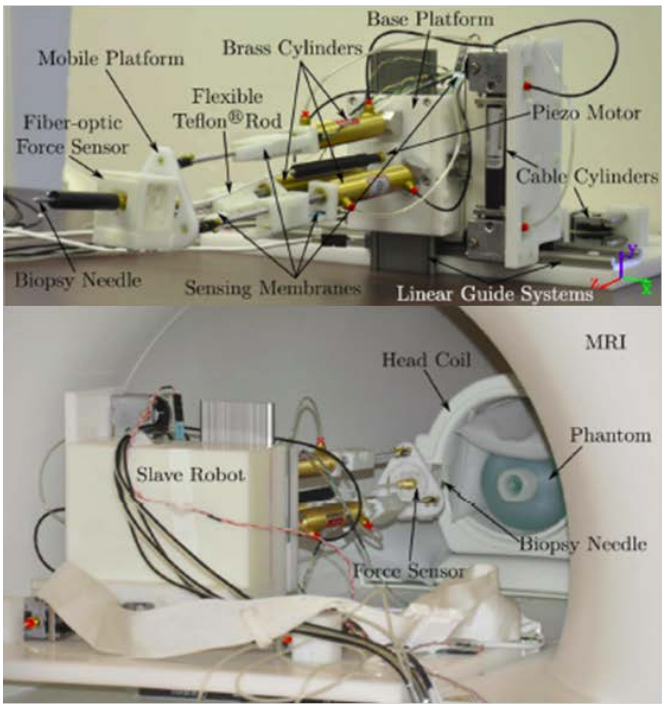

(c)

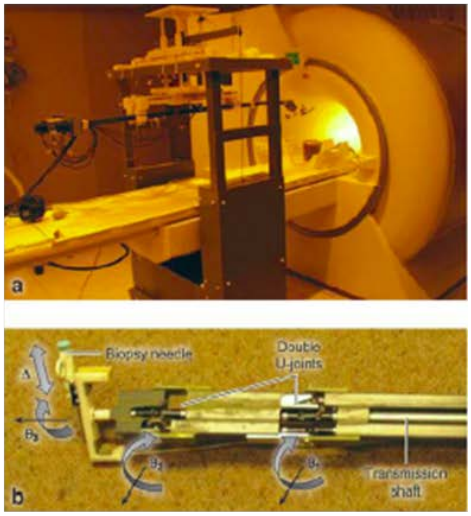

(d)

Fig. 1-2: (a) MRI-Guided Cardiothoracic Surgery Robot [15]. (b) MRI-Guided Neurosurgery Robot [12]. (c) MRI-Guided Breast Surgery Robot [16]. (d) MRI-Guided General Surgery Robot [17].

Although various image-guided surgery systems are developed for different surgical applications, most of them are still in the prototype stage, and few clinical trials have been conducted so far. Reliability and generality are still the two critical concerns for MRI-guided systems. Some MRI-guided surgery systems are shown in Fig. 1-2.

The typical work flow for MRI-guided MIS is shown as follows:

1. Acquire pre-operative image by MR scanner and then extract valid tracking area

2. Register and track the patient anatomy and surgery instrument from the valid image

3. Manipulate the tool to carry out the procedure under the guidance of marked MR images

1.1.2 Advantages of MRI for MIS

Nowadays, doctors achieve sophisticated clinical operations with the help of modern, complicated medical instruments, like surgery under MRI or Ultrasound guidance. They prefer to adopt minimally invasive procedures to decrease the possibility of patient injury. However, precise placement and operation of surgical tools inside a narrow device environment, like an MRI scanner, is a tough task due to restricted space and poor ergonomics. In many cases, the instrument based surgeries are limited by the inherently stereotactic problem. Therefore, effective tracking and image analysis methods are needed to facilitate the accurate placement and operation of surgical tools during therapy. The primary advantages of using MRI for guidance of MIS are due to the inherent physical principles of the MRI. The MRI-based medical paradigm offers several advantages over other imaging counterparts.

1) MRI has multiple mechanisms to provide high-fidelity soft tissue contrast and spatial resolution. It provides excellent soft tissue contrast that allows for visualization of tumors that are not visible using other modalities. Thus, it aids early diagnosis and treatment. Since it provides accurate positioning of targets, it is ideal for robot-assisted procedures as visual targets.

2) MRI provides the capability to sense a variety of physiological parameters. This includes temperature sensing (also known as MRI thermal imaging), or blood flow measurement within a vascular malformation. Similar to visual sensing of tissue and tools, this extraordinary sensing feature enables monitoring and control of therapeutic interventions. In particular, it can potentially be used for closed-loop robotic intervention to regulate or track physiological parameters.

3) MRI is capable of imaging both soft tissue and intervention tools on arbitrary planes. The MRI is a three-dimensional imaging modality that permits arbitrary imaging plane selection, even in a dynamic manner. It allows for localization of the interventional tools and allows for on-the-fly adjustment of the imaging plane. This feature is particularly favorable for robotic applications, which relies on MRI sensory feedback to guide and control robot motion to close the control loop;

4) MRI produces no ionizing radiation, and thus imposes no radiation safety hazard to the patient or practitioner. This is especially beneficial to patients who are imaged frequently, and to interventional radiologists who perform procedures on a regular basis.

1.1.3 Motivation of Registration and Tracking System for MRI-guided Robots

With these aforementioned advantages, robotics researchers worldwide have begun to design and utilize surgical robots for MRI procedures. Recently, almost all the tracking systems for surgical robots are custom-written for exclusive robot under specific image-guided environment. The Innomotion robot [18] is the first commercially available MRI-guided robot that utilizes pneumatic actuation and was recently acquired by Synthes Holding AG. As shown in Fig. 1-3, it has pneumatically actuated 5 DOF and manually actuated 2 DOF. The manual actuation is denoted with a red arrow for positioning at the orbit and a green arrow for positioning along the patient bed. The robot is attached to a 180° orbiting ring that is mounted to the patient table. The robot arm is fixed with a spring-loaded bolt and secured with a screw. The base of the robot provides XYZ Cartesian motion, while the end-effector is a 2-DOF remote center of motion mechanism. Although the robot itself has a high targeting accuracy, the intraoperative images about the position and orientation of the surgical tool with respect to the patient anatomy are always crucial.

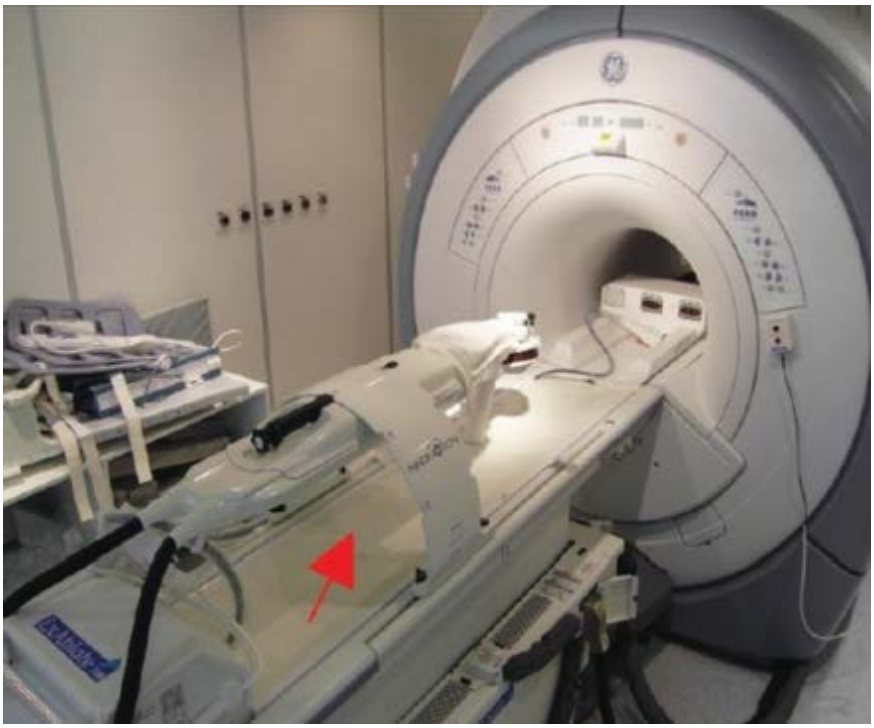

Fig. 1-3: MRI-guided surgical application of the Innomotion robotic system (red arrow). It has pneumatically actuated 5 DOF and manually actuated 2 DOF [18].

Besides the Innomotion robot, NeuroArm shown in Fig. 1-4 (a) (b) is another MRI-guided master-slave remote operation system for neurosurgical procedures. The surgeon's hand motions in 7 DOF are remotely mapped to the robotic manipulators. The system includes a workstation, a control cabinet, and two slave robot arms mounted on a mobile base. It provides functionalities such as tremor filtering and motion scaling to increase precision and accuracy. It also supports virtual fixtures (a mechanism that provides surgical no-fly zone) and mechanical locks to enhance safety. As shown in Fig. 1-4(c), the human machine interface includes two video monitors, two touch screen computer displays, and a stereoscopic display unit. The first clinical case, a tumor removal operation, was successfully carried out in May 2008 [19]. IMRIS, Inc. (Winnipeg, Canada) acquired the NeuroArm in February 2010, and is developing a next generation intraoperative MRI surgical robot in conjunction with MDA. However, all these sophisticated tracking systems are still feasible for specific robots and people can't conveniently reuse it with other MRI-guided robots or under different image-guided environment.

Fig. 1-4: (a) NeuroArm robot developed at University of Calgary. (b) CAD breakdown structure of NeuroArm robot with 7 DOF descriptions. (c) Human machine interface of NeuroArm robot [19].

1.2 Literature Review

Numerous registration and tracking technologies used in clinical surgeries have been described in literature. This literature review surveys and lists different kinds of resonant coil markers and registration fiducial frames which provide not only specific patters of fiducials to track but also the approaches to make those fiducials more readily visible. Following are some of them, along with brief analyses about their advantages and disadvantages.

1.2.1 Resonant Coil Marker Designs

Resonant coil markers are mainly use for enhancing visibility of stereotactic pattern. There are two types of resonant coil in MRI guidance: passive coil marker and active coil marker. Each one has their own merits and demerits that decide how people use them in specific clinical application.

- **Passive Single Micro-coil Marker**

Passive Single Micro-coil Marker is usually made out of non-ferromagnetic metal with contrast medium inside. It advantages are MRI scanner independent and easy integration. Fig. 1-5 shows a typical application of micro-coil in a spiral shape [20]. Researchers compared the ability of ten different image-processing algorithms to track these micro-coil fiducials with sub-pixel accuracy. This tiny coil marker has a diameter of 3mm and a pixel size of 1.1mm. A maximum error of 0.22mm was observed in fiducial localization for displacements up to 40mm.

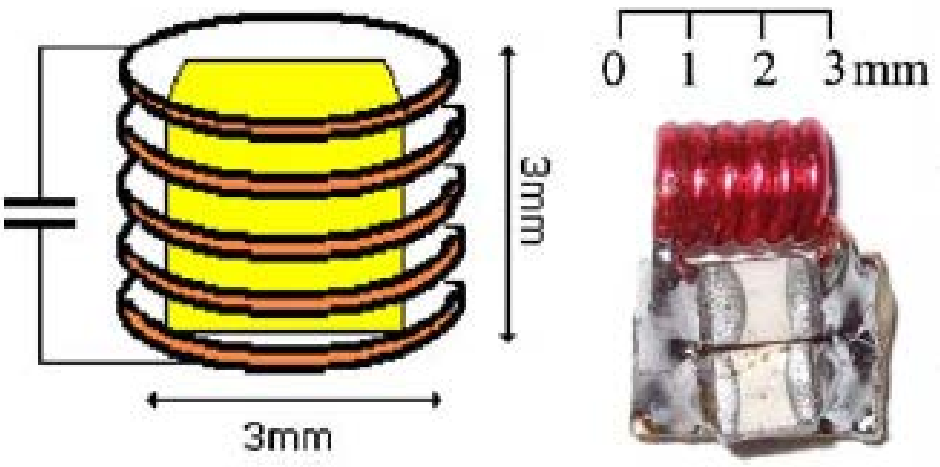

Fig. 1-5: Left diagram showing the dimensions of passive single micro-coil marker design, and right is an actual tuned micro-coil fiducial marker [20].

This fiducial prototype is compact, provides good contrast in the MRI, and has very little image distortion. However, its resonance frequency is fixed to serve for specific MR scanner but not adjustable. Another drawback is the fact that its shape in an MRI is just a point. To apply it to more complicated and reliable stereotactic registration, too many coils would be needed.

- **Active Single Micro-coil Fiducial Marker**

Active single micro-coil marker is another commonly used tracking methods with high brightness and space expansibility. The design, shown in Fig. 1-6, proposes an active micro-coil filling with semisolid method to do localization and tracking for medical devices like application in air filled body cavities [21]. By a road mapping reconstruction, the micro-coil's trajectory could be visualized on a previously acquired reference image. It sets with a tracking rate of up to 60 Hz at a spatial resolution of better than 2mm. In a real-time tracking implementation, an image update rate of 4 Hz was achieved by combining the tracking with a fast real-time imaging sequence.

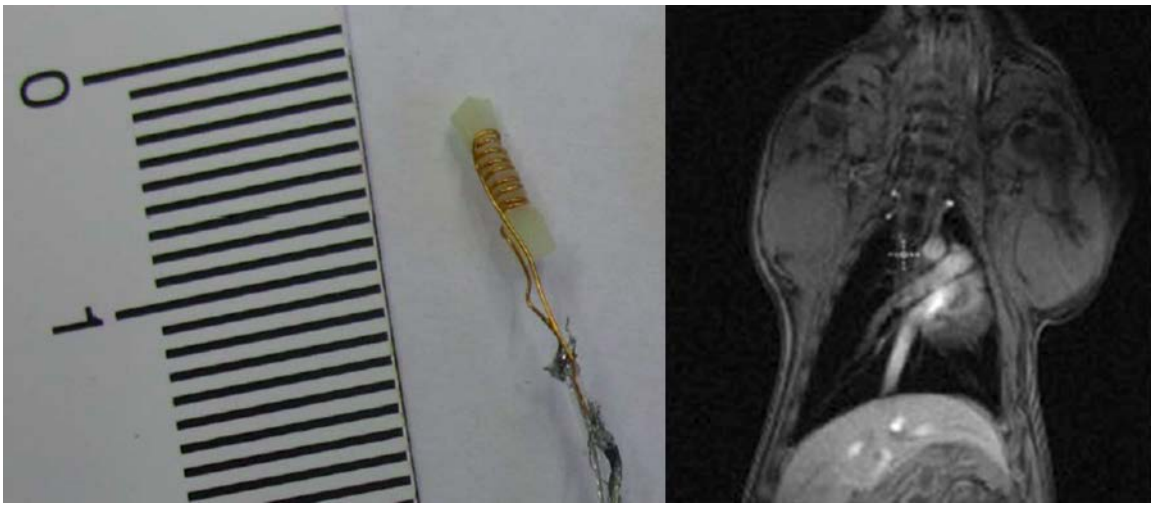

Fig. 1-6: The latex coil former (left) fills the coil and extends at its distal ends to cover the most sensitive regions of the solenoid. Real-time tracking images (right) with micro-coil at different positions in the pig's trachea and lungs. The slice position is automatically adapted to the micro-coil position [21].

One advantage of active micro-coils is a longer imaging dimension and a brighter tracking spot than can be achieved with passive coils. It is possible to form active micro-coils into many arbitrary

shapes using in the imaging application. Yet the drawback of active micro-coil is also obvious. Their manufacture is more sophisticated than passive coils since they need inputs to coordinate their resonances.

- **Passive Multiple Coil Fiducial Markers**

Passive multiple coil fiducial markers are cooperation of many passive single coil to achieve complex tracking goal. The design, shown in Fig. 1-7, demonstrates the feasibility of using three wireless, long dimension coils as fiducial markers [22]. It supports fast imaging with limited projection reconstruction to accurately obtain tracking information in an MRI. The position and tracking of a rigid interventional instrument can be uniquely evaluated from the 3D coordinates of three fiducial markers mounted in a known configuration on that instrument. Three fiducial markers were tuned to the resonant frequency in a 0.2T open MR scanner and wrapped to the surface of a cylindrical water phantom.

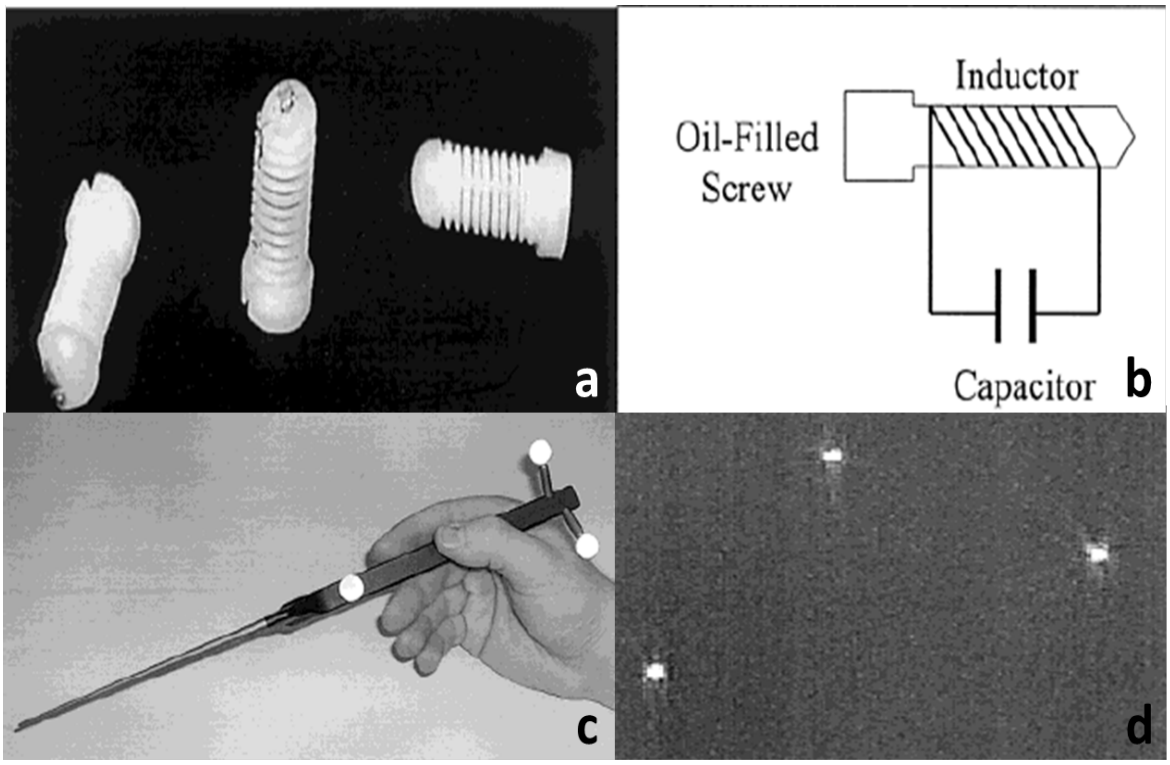

Fig. 1-7: Photograph (a) and schematic (b) of tuned fiducial markers. The resonant frequency of each marker consistently couples with MRI scanner and enhances magnetic field to amplify the internal marker signal (oil) relative to any other signal source. Photograph (c) of a localizing wand is used by an optical tracking system

(Aesculap Pointer FS613, Siemens Medical Engineering Group, Erlangen, Germany). Cross-sectional image (d) reconstructed from LPR-FISP algorithm with 180 projections of three fiducial markers mounted onto a water phantom. The image was acquired with a 7° tip angle [22].

These three tuned fiducial markers adopt a localization algorithm to accurately calculate the 3D coordinates of the fiducial markers in two orthogonal scan planes. Meanwhile, their short sequence repetition time (TR = 21ms) and rapid projection reconstruction time (about 170ms) allow them to achieve real-time tracking with high accuracy, with error within 3 mm on a 0.2T MR system. The only limitation is its unique algorithm to process projection reconstruction for correction, its strong MR scanner dependence, and the fact that it's not very ideal for stereotactic tacking.

- **Active Multiple Coil Fiducial Markers**

Active multiple coil fiducial markers is emerging technology in MRI guidance at present. The Fig. 1-8 shows a multi-element coil design with two sub-coil markers in the array for active MR device tracking [23]. The device consists of two independent and opposed-solenoid phased coils which are wound in opposite directions and respectively connected to separate receive channels. During real-time catheter tracking, each element gave rise to a high-amplitude peak in its respective projection data, which enabled reliable and robust device tracking as well as automated slice positioning. The array's imaging performance was tested on a clinical 1.5 T MRI scanner, getting a high resolution micro imaging in vivo.

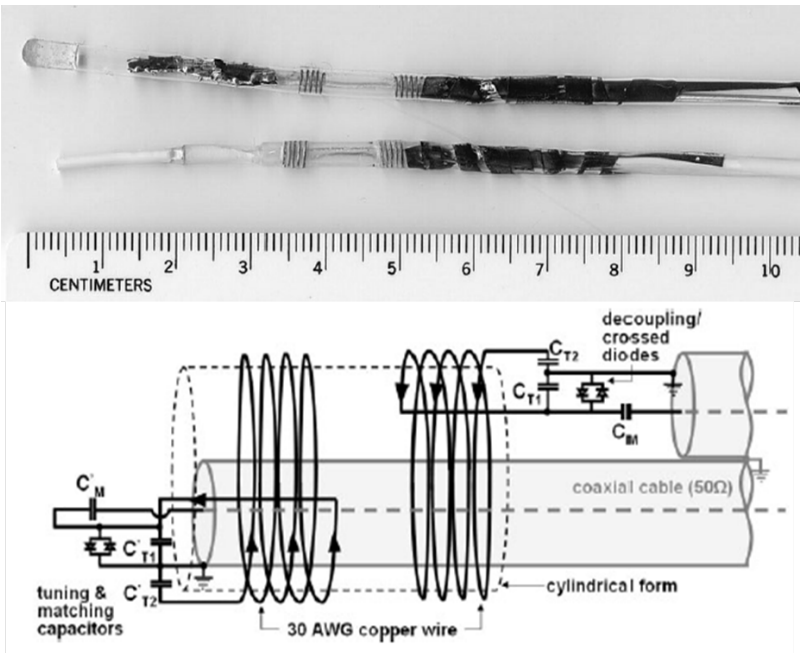

Fig. 1-8: Photograph (top) of the two opposed solenoid arrays (five windings per solenoid coil; gap between the two solenoid coils = 1 cm; coil diameter = 5 F; wire diameter = 30 AWG; independent tune -, match-, and decoupling circuit). Electrical schematic (bottom) of the opposed-solenoid phased array catheter coil. Two solenoid coils, counter wound from copper wire, are fixed on a cylindrical form. The coils are separately tuned to the MR scanner's resonance frequency of 63.65 MHz, using small ceramic capacitors [23].

This array coil has a relatively long structure compared to other coil based tracking markers, and needs custom-written ICE/IDEA tracking software for specific MR scanners. Yet it was proved to be practical enough in clinical guidance and imaging application like intravascular interventions. The independent coils could be used individually for tracking, or be combined for high-resolution stereotactic imaging.

1.2.2 Registration Fiducial Frame Designs

Fiducial frames provide necessary information in imaging slices to track target pose. There are many kinds of fiducial frame shape serving for different DOF registration and tracking requirement. Following are several configurations using in image-guided clinical applications.

- **Brown-Roberts –Wells (Z-frame) Fiducial**

The most common fiducial frame is the so-called Brown-Roberts-Wells fiducial frame, or the Z-frame fiducial [24,25]. It consists of 3 planar Z-shaped fiducial patterns that are connected together in a rectangular shape, as show in Fig. 1-9.

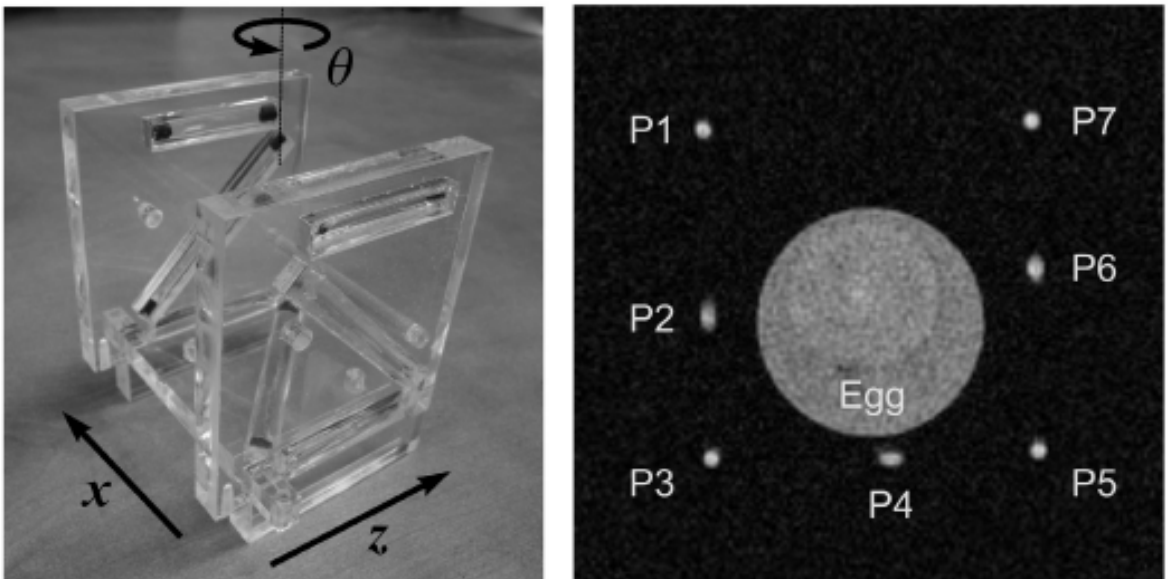

Fig. 1-9: Z-frame (left) and typical MRI reading of a cross-section of the Z-frame fiducial target (right) [24].

The target is very common mainly because it's relatively easy to describe mathematically and thus to interpret the MRI scans in the tracking process. One of its main disadvantages is that its sensitivity on the Z-axis (along the cross-sectional direction of the body and the MRI) is dependent on its length in that direction, relative to its height on the Y-axis. This makes the target design relatively bulky and unsuitable for applications that have tight size constrains.

- **The Prism Fiducial**

This design is intended for preoperative tracking. It has a planar 2D version for interpretive adjustment of the tracking process in case there are discrepancies in the preoperative tracking [26], as shown in Fig. 1-10. The target is intended for use in x-ray but it can also be applied to MRI.

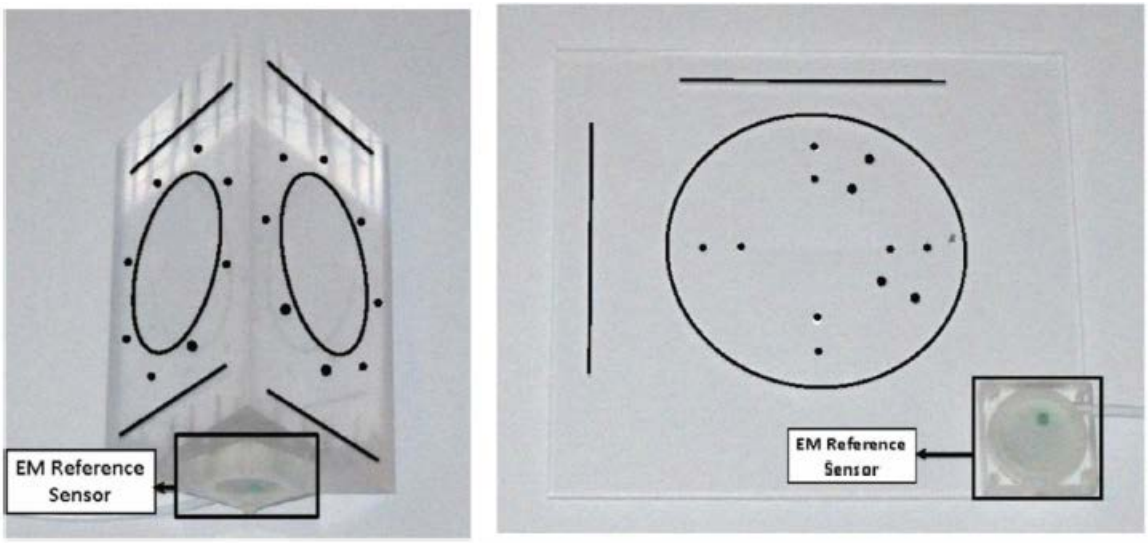

Fig. 1-10: 3D prism design (left) and a planar (right) 2D version of prism fiducial [26].

The advantage of this design is that it provides higher complexity and greater variety of features for detection, which provides better accuracy. However the tracking evaluation is somewhat complicated. The design itself is also physically large and thus not suitable for small volumes.

- **Two Types of Ellipse fiducial**

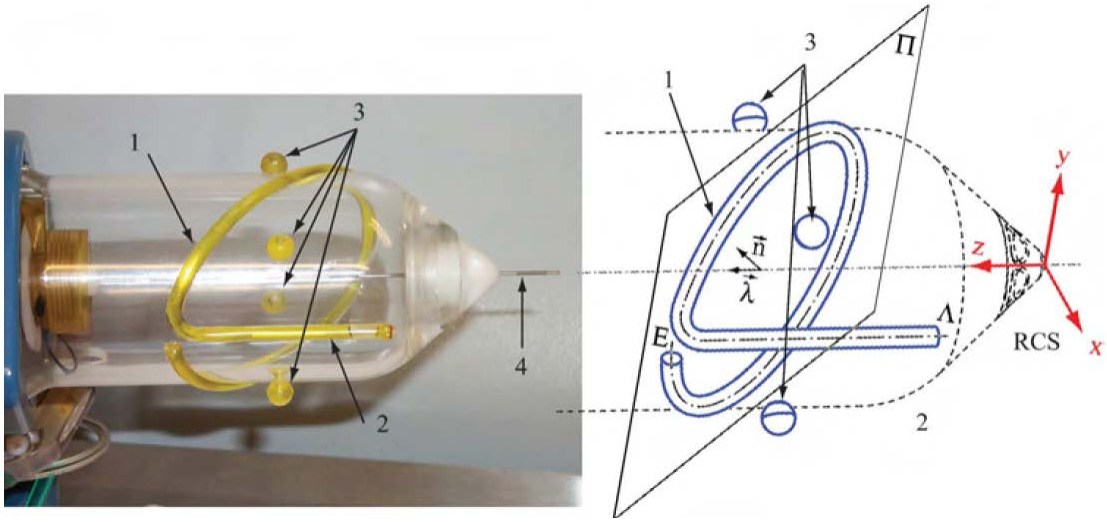

Fig. 1-11: Ellipse design in MRI [27].

A more elaborate yet compact design offers the tracking accuracy advantages of complex targets in a relatively small design space [27]. The design incorporates several types of features

similar to the prism design, but they are wrapped in a cylinder configuration, shown in Fig. 1-11. This is achieved by making custom tubing to hold MRI high contrast liquid in combination with standard ball-shaped markers.

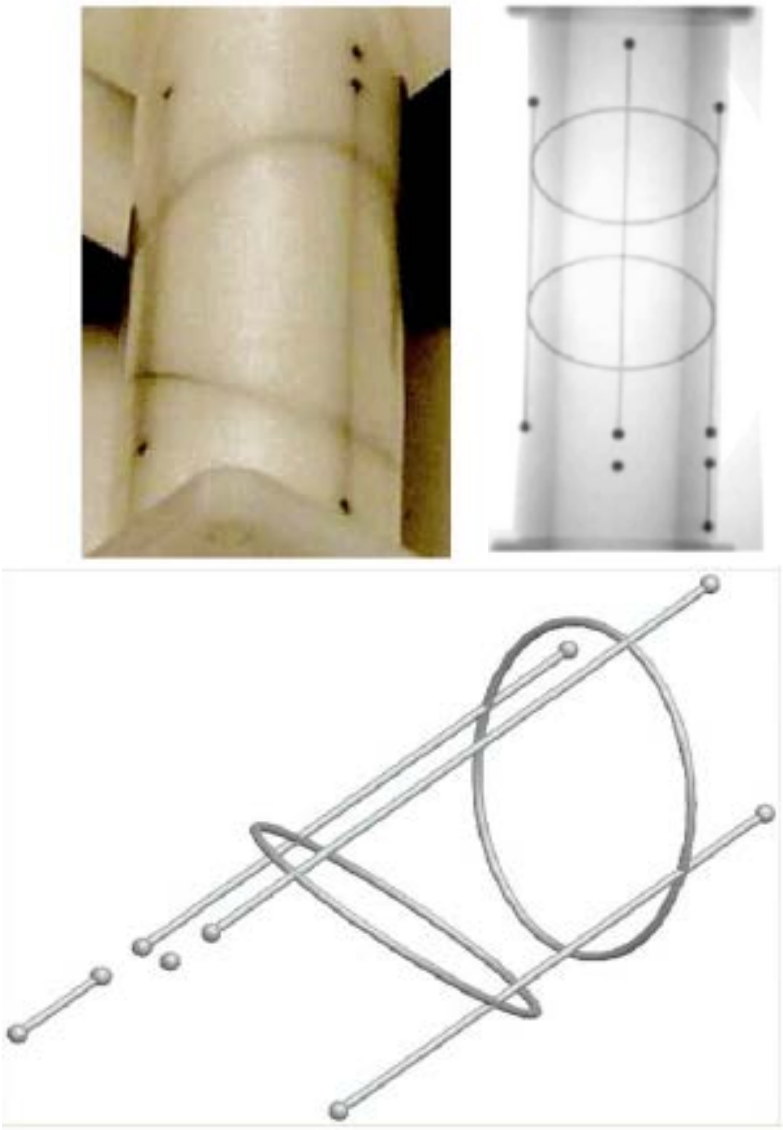

Fig. 1-12: Ellipse design in fluoroscopy [28].

A very similar idea is shown in Fig. 1-12 as a design that combines two ellipses and several straight lines. This design is based on thin metal wires that have been placed in a precisely machined feature-holding body for tracking in fluoroscopy [28]. While this second version of the ellipse design is even more elaborate and complicated to manufacture, it offers even better tracking accuracy. The

design ideology of the ellipse was chosen as an essential preferred approach for the fiducial frame in this thesis. We aim to compress a complex tracking pattern to a more compact configuration, but with a relatively decreased manufacturing complexity. Our design approach will be explained in later chapters.

1.3 Thesis Contribution

As described previously, this thesis builds a commonly used real-time posture tracking system for MRI robots. With its help, the MRI-guided robot control will become a better loop system with both movement correction and visual feedback. It is also a modular system that adopts a standardized medical image communication protocol named OpenIGTLink to do network data transmission among modules. Hence, it is remote control feasible and MR scanner independent. The primary contributions of this thesis are:

- **An exclusive 6-DOF registration and tracking fiducial frame and corresponding algorithm**

The fiducial frame of the registration and tracking system can be served for tracking full 6-DOF in stereotactic interventional surgery. The name of the registration and tracking fiducial frame is the Cylindrical Helix Imaging Coordinate (CHIC) fiducial frame. In the presented MRI-compatible embodiment of the fiducial design, there are nine tubes inside the frame which are all filled with high MRI contrast gelatin or gadolinium fluid to provide ample tracking spots in the cross-sectional image to guarantee detection accuracy and stability of the image analysis algorithm. The unique imaging pattern inside CHIC frame allows detection of all 6-DOF at any arbitrary pose by using only one slice image, so the corresponding algorithm is a single slice based image recognition technology.

- **A stand-alone registration and tracking system with modular framework**

To allow functional extension in the future, this system has been created with modular architecture. The modular system will provide high precision and remote tracking assisting to different types of MRI-guided robot in MIS. On one side, the software is constructed upon a modular

data transmission framework so that it supports remote supervision and manipulation between the 3D Matlab tracking user interface and robot controller using the OpenIGTLink network communication protocol. On the other side, the mechanical structure of fiducial frame module can take various forms based on the robot requirements and accuracy and configuration needs as well as it has high MRI compatibility which allows us to use it in 3 Tesla MR scanner.

- **A novel passive resonant coil to support real time MRI tracking**

The compact fiducial frame is wrapped with exterior resonant coil for supporting fast imaging. This passive tracking coil can sharply reduce imaging time by resonating with MRI main coil so that we can track rapid movement and extend its application fields to continuous freehand surgery. It has sophisticated stereotactic structure and almost symmetric distribution to counteract image distortion generating by each sub-coil. The rapid imaging ability of this resonant coil based tracking fiducial frame was evaluated under 3 Tesla MR scanner using real-time fast low-angle shot (FLASH) pulse sequences.

Chapter 2

Design Requirements

MRI-guided minimally invasive surgery allows interventional procedures with greater precision and superior outcomes by integrating medical imaging with the surgical workflow. However, developing real-time registration and tracking system for intraoperative MRI-guided surgery presents new challenges and limitation such as electromagnetic compatibility and mechanical constraints of the confined close-bore.

2.1 MRI Compatibility

MRI is an ideal guidance modality with the ability to perform high quality, volumetric, real-time, multi-parametric imaging with high soft tissue contrast without ionizing radiation. But it is a tough task when people implement any design working in the MRI environment where exits high static magnetic field (1.5T or greater) and pulsed radiofrequency (RF) field. A thorough description of the issues relating to MR Safety is described by Shellock [29]. The MR-Safe definitions are according to the ASTM Standard F2052 [30] while MR-compatible is the commonly used term:

MR-Safe: The device, when used in the MR environment, has been demonstrated to present no additional risk to the patient or other individual, but may affect the quality of the diagnostic information. The MR conditions in which the device was tested should be specified in conjunction with the term MR safe since a device that is safe under one set of conditions may not be found to be so under more extreme MR conditions.

MR-Compatible: A device is considered MR-compatible if it is MR safe and if it, when used in the MR environment, has been demonstrated to neither significantly affect the quality of the diagnostic information nor have its operations affected by the MR device. The MR conditions in which the device was tested should be specified in conjunction with the term MR-compatible since a device that is safe under one set of conditions may not be found to be so under more extreme MR conditions.

Currently, there is no generally accepted definition for MRI compatibility of interventional system, though the National Electronic Manufacturers Association (NEMA) standard for signal to noise ratio (SNR) is commonly used to assess image quality [31]. A review of MRI compatible system for image-guided interventions being developed to date has been performed by Tsekos et al [32]. Beyond the SNR standard of collected images, it is important to understand bidirectional feature of MRI compatibility that means both the device does not cause image artifacts during the scanner imaging and the scanner should also not disturb the device function. Ferromagnetic materials must be avoided completely, and nonferrous metals such as aluminum, brass, nitinol and titanium should also be used limitedly in certain MRI environment. In this system, whole registration and tracking fiducial frame are made out of high strength, MRI-compatible plastics with limited nonferrous coil.

2.2 Workspace

Besides the MRI compatibility, the limitation of workspace insider of the MR bore is another problem that cannot be ignored. Traditional MR scanner provides a long and narrow cylindrical valid imaging area so that the workspace is tightly constrained in the scanner bore. For implementing and testing, a Phillips Achieva 3T MRI scanner system was targeted. This scanner has a bore diameter of 60cm, however, with the bed in place, it just leaves about 50cm clearance for robot and registration and tracking system, see Fig. 2-1.

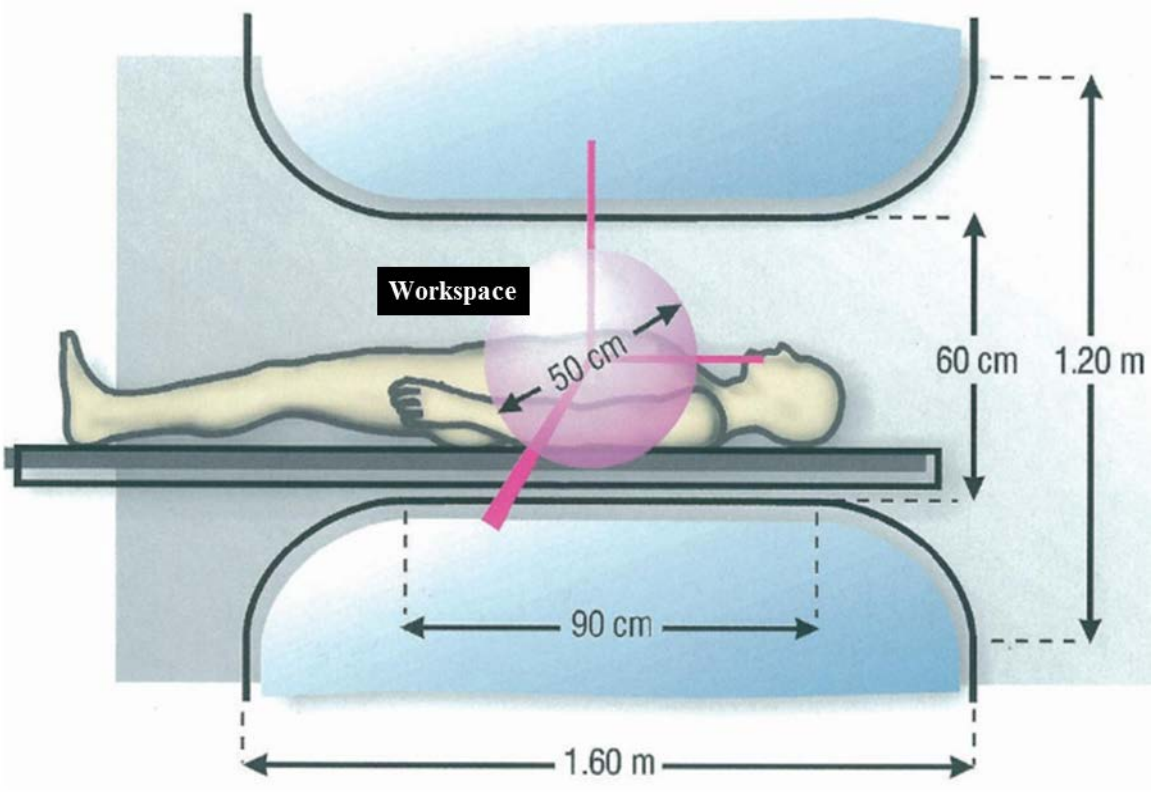

Fig. 2-1: Illustration of long and narrow workspace inside Phillips 3T MRI scanner [33].

2.3 High Resonant Frequency

Using passive resonant coil for MRI guidance is both scanner-independence for a small range of field strength and easier for integration than active resonant coil as well as it can decrease MR imaging time sharply providing a real-time tracking ability to fiducial frame. Although metal circuit caused compatibility issue can be ameliorated by utilizing limited non-ferromagnetic material, it still leads some distortion to MR images. In order to minimize image distortion, the diameter of coil also should be as small as possible. Meanwhile, the geometric shape of sub-coils should be symmetry with each other to counteract deforming influence.

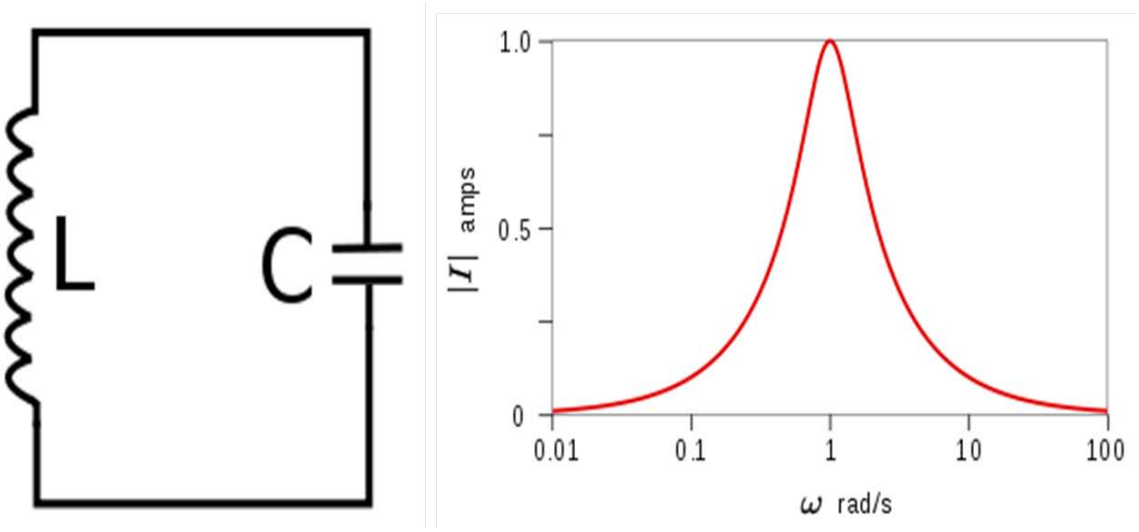

Fig. 2-2: LC circuit schematic diagram and current response analysis for exterior stimulate

Another challenge existing in passive resonant coil is its relative small tracking dimension compare with active imaging coil. This is because the LC circuit obeys the laws of physics to spark resonant current inside, which can be described as: $f = \frac{1}{2\pi\sqrt{LC}}$, see Fig. 2-2. In order to make the passive resonant coil work with the MR scanner, its resonant frequency should be close to MR scanner's imaging frequency. In light of the imaging frequency of MR scanner is usually very high reaching tens of MHz and some of high magnetic field MR scanner even over 100MHz under normal operating conditions while the tiny capacitor we can get just at least 1pF. It is an arduous task to make the dimension of passive resonant coil become large due to volume itself will generate high inductance breaking resonant requirement. To guarantee the generality of the system under some high frequency MR scanner, we take a relative tough requirement to design our passive coil working with 128 MHz Phillips Achieva 3T MRI scanner system which is the same facility as mention before. We can calculate that the inductance of our passive resonant coil have to no larger than 1.55μH by connecting with a tiny 1pF capacitor.

Chapter 3

System Architecture

The real-time registration and tracking system will operate with the surgical robot simultaneously in the confined MRI bore. On one side, the compact fiducial frame being wrapped with exterior resonant coil can be easily attached near the distal end of the robot arm for the purpose of imaging in the MRI slices synchronously. On the other side, its software system is a strong back up to surgeon supervising and manipulating robot during surgical process.

3.1 Panorama of Cooperation of Registration and Tracking System with Surgical Robot in MIS

The modular manner of system construction guarantees each functionalized module performs its own functions. Its software framework and corresponding workflow with robot is depicted in Fig. 3-1. To allow functional extension in the future, the registration and tracking system has been created by integrating five main modules: 1) green tracking module is the main body of registration and tracking algorithm; 2) aqua user interface module gives a visual description about the posture of robot back to operator; 3) orange DICOM server module which is the input interface of the system also acts as data base for whole system; 4) blue correction feedback module will output the correction transformation matrix to robot controller for adjusting robot movement; and 5) passive coil wrapped fiducial frame module is mounted on robot. The solid line represents communication between modules via cable while dashed line connected modules exchange information via network under

OpenIGTLink protocol. The OpenIGTLink protocol was adopted by wide variety of image-guided therapy (IGT) applications [34,35] to provide a standardized mechanism for communications from computers or devices in operating rooms to any terminal in network. The tracking module and user interface are isolated by network connection so that they support remote control and transplant main body of algorithm into other platforms, such as Linux, Mac etc.

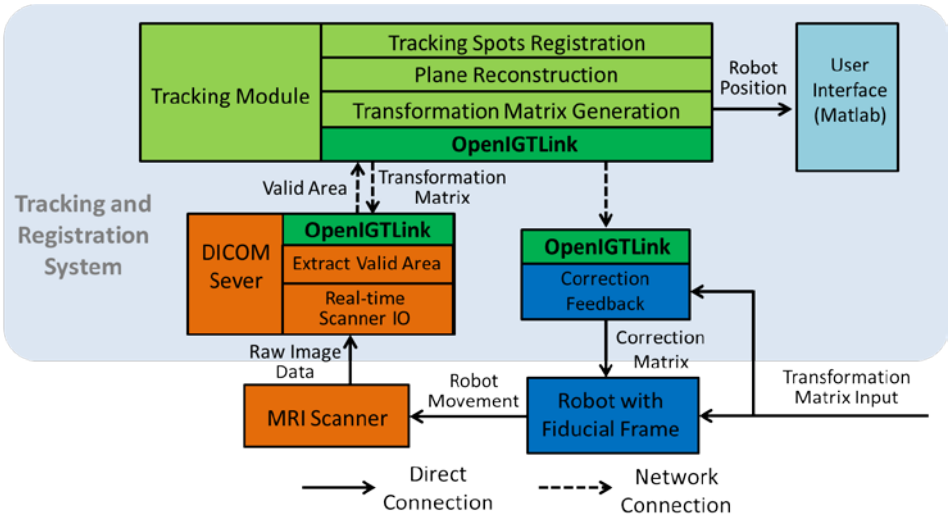

Fig. 3-1: System architecture and data flow of registration and tracking system. The modules in gray block constitute the software framework in the system where tracking module and user interface are isolated by network connection from other direct modules in operating rooms.

To piece all things together, Fig. 3-2 shows the setting of the whole real-time MRI-guided robotic surgery environment. This registration and tracking system aims to combine these two technologies together: robots and machine vision. We have developed a modular mechanical structure and software architecture, which is scanner independent and remote control feasible. In Fig. 3-2(a), the fiducial frame was adhered on a robot which was controlled from the console room Fig. 3-2(b). Although we can supervise 2D MR images from MRI console in operating room to manipulate robot, this just gives limited information about relative place of instrument and patient anatomy. While registration and tracking system will provide a 3D visual feedback to let surgeon know 6-DOF pose of instrument as well as a referential correction transformation matrix will be outputted to robot controller.

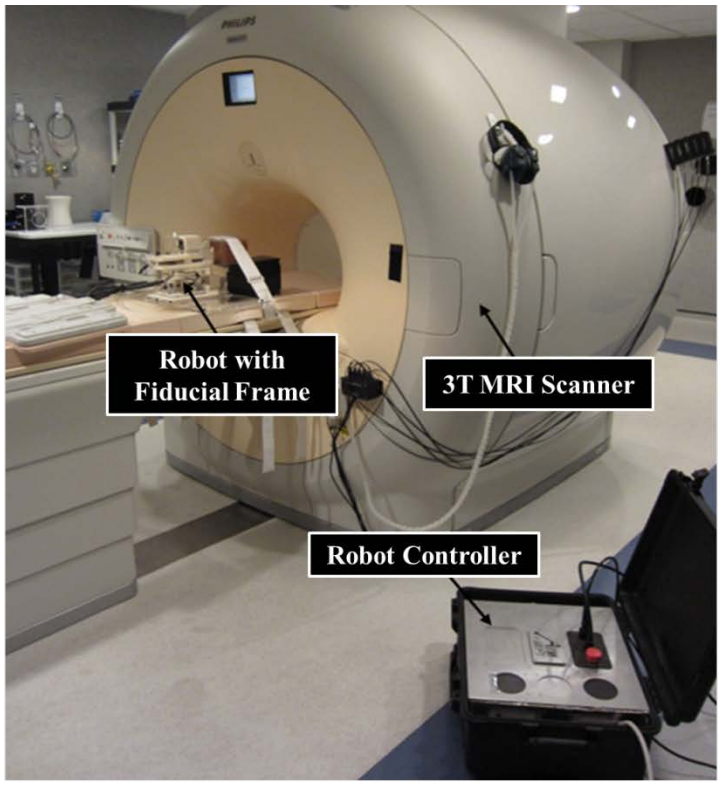

(a)

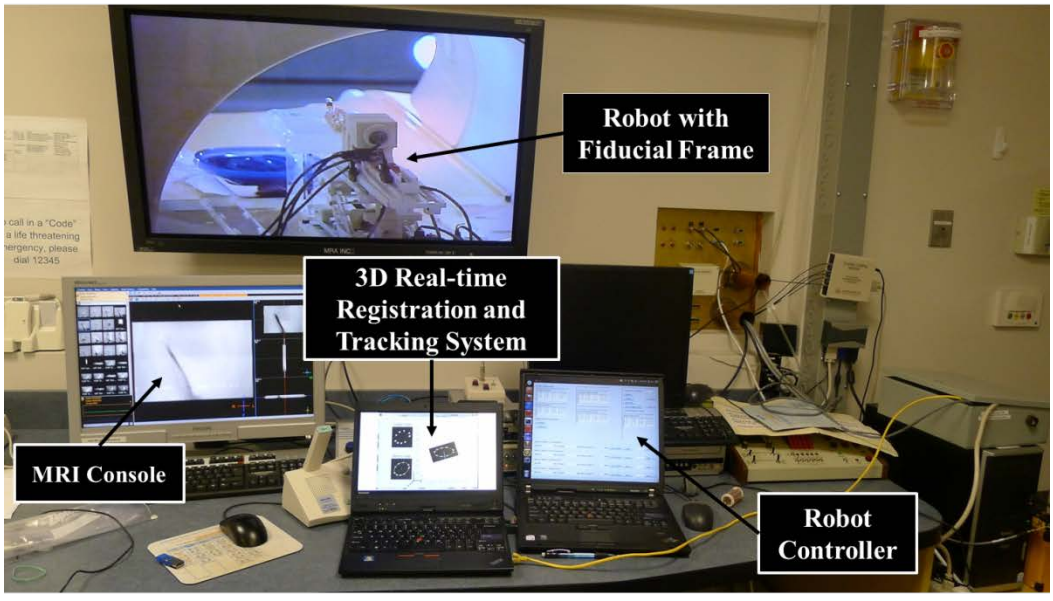

(b)

Fig. 3-2: The panorama of real-time MRI-guided robotic surgery system setting. (a) Robot with fiducial frame and robot controller inside the MR scanner room. (b) Robot controller user interface and real-time tracking system supervise and manipulate robot to do surgery remotely in the operation room.

3.2 DICOM Sever Module

The DICOM sever module could act as input interface and data base that undertakes bidirectional communication with internal module via network connection, as shown in Fig. 3-3. This module buffers a massive amount of raw MRI scanning images from MR scanner IO port. And an interior DICOM image data base storages buffered image stream in real time. Then it will extract small valid tracking area from large raw image data to track module processing. This step is critical process to shrink image processing time to support real-time tracking. Finally it would storage DICOM image with corresponding transformation matrix in the data base.

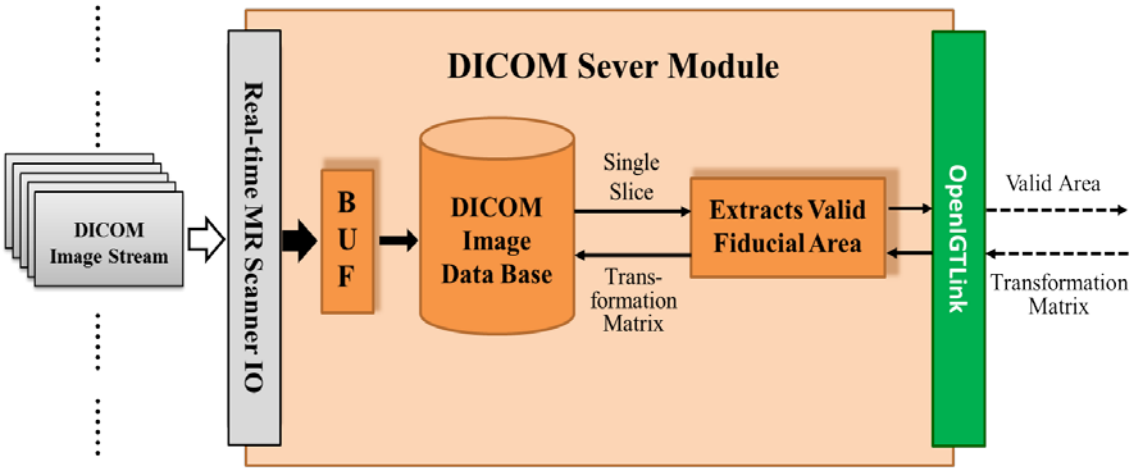

Fig. 3-3: DICOM sever module interior data flow

3.3 Tracking Module

The tracking module is the “brain” of registration and tracking system which is in charge of evaluating stereotactic information from sophisticated tracking spots pattern in 2D cross-sectional image. It is also an independent module isolated by network connection far from MR scanner. Besides image analysis function, it also undertakes bidirectional communication with DICOM sever module and tracking information output to two downstream modules. The algorithm of tracking module will be divided into three main steps: 1) tracking spots registration; 2) plane reconstruction;

and 3) transformation matrix generation, see Fig. 3-4. More detailed description for each steps are in Chapter 5.

The first step, tracking spots registration, is about feature extraction from input images. After a new slice of valid tracking area being loaded into tracking module, the software will identify all the tracking spots inside. In rare cases, we may meet tracking information deficiency because certain valid tracking areas could not be identified containing enough spots to rebuild feature pattern. So we have to push out these rags from further image analysis and reload new valid tracking area to keep the running robustness of whole system. If the tracking spots are countered completely, the software will do centroid measurement for each of spot. We proposed a new method which brings in statistic Gaussian model fitting to improve robustness of centroid measurement by anti-jamming from foaming phenomenon in contrast medium imaging. Its ins and outs will be discussed in Chapter 5.

The second step, plane reconstruction, is about information reversion from featured 2D plane pattern back to 3D pose. We will use least-square method to fit these centroids from nine separate tracking spots into a generalized ellipse equation. And reconstruction the tracking area with ellipse plane together. Then this general parametric form of ellipse equation combining with included angles of each two tracking spots with respect to center of ellipse could elicit enough information to rebuild stereo 6-DOF pose.

The last step, transformation matrix generation, is about tracking results synthesis and output. The software will generate rotation matrix from 3 DOF of rotation and then combine it with other 3 DOF of translation to constitute a transformation matrix for describing stereotactic pose in robotic manner since most of the robot controls are depended on transformation matrix. Finally, it will send these tracking results to relative modules by network and reload a new slice of tracking area recurrently.

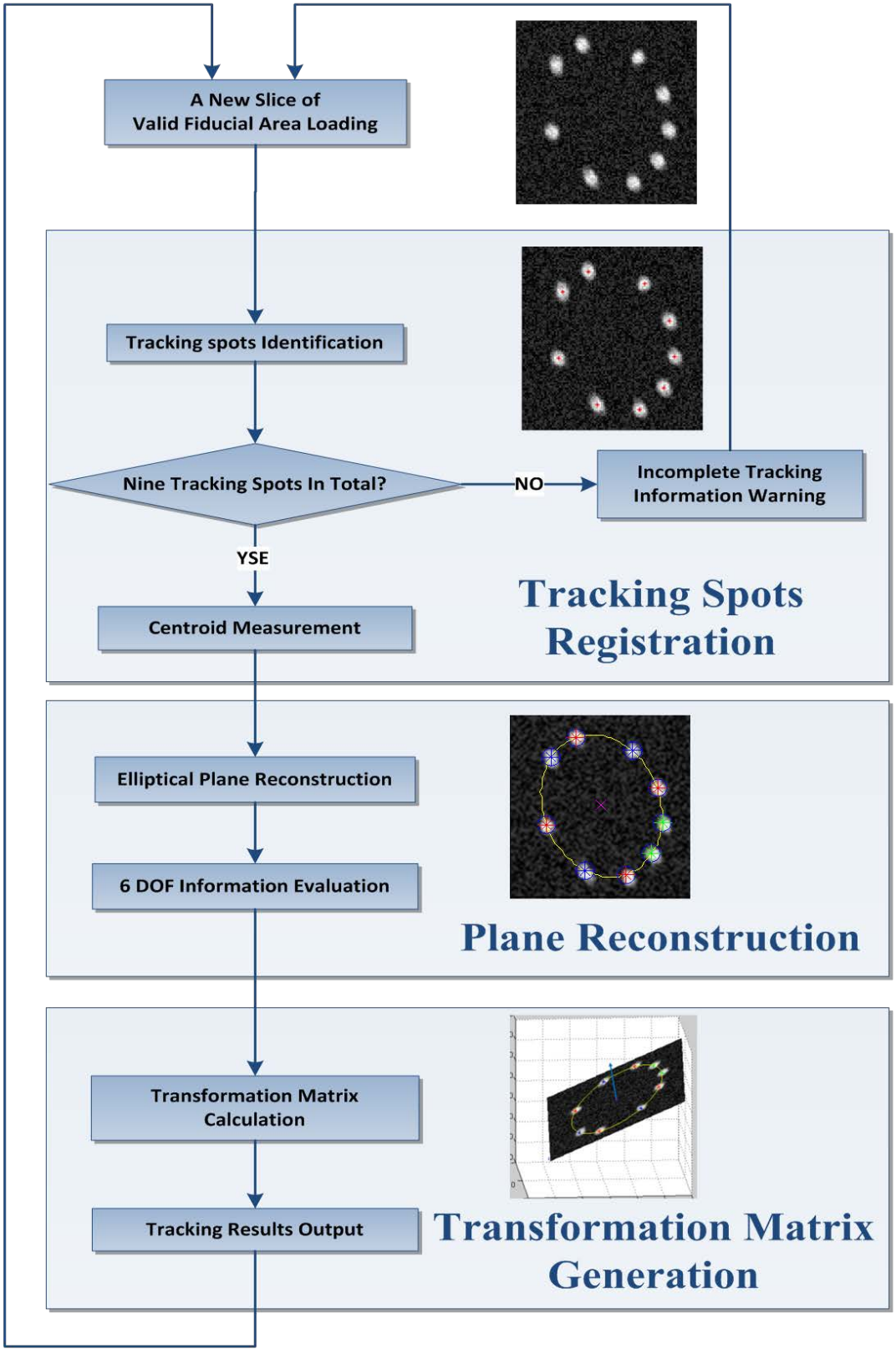

Fig. 3-4: Algorithm of tracking module to detect and localize the fiducial frame

3.4 1User Interface Module

The user interface module running on Matlab platform provides an intuitive sense for tracking surgical procedure in real time. A sample of visual feedback results are shown in Fig. 3-5. This visual display was implemented on Matlab platform which includes an OpenIGTLink plug-in module to receive tracking results from tracking module. It was integrated with tracking module together in remote control side so that surgeon could supervise operation process in the operating room where is far away from MR scanner.

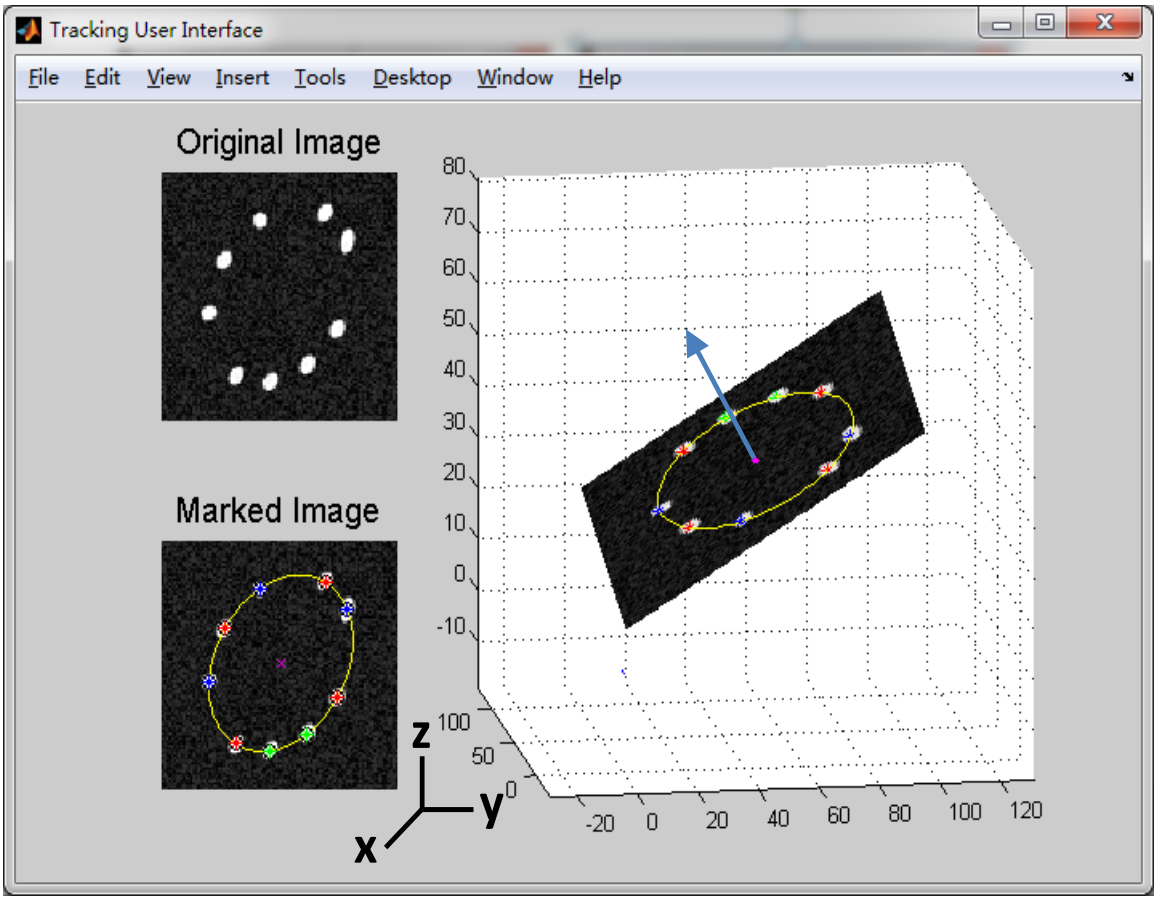

Fig. 3-5: The 3D visual interface for real time stereotactic pose tracking. It consists of three visual fields: original image, marked image and main 3D pose view

In Fig. 3-5, the main visual field on the right provides a 3D visual view about stereotactic pose of target. In this view, the cross-sectional plane will be automatically adapted to right steric configuration of target according to tracking results. There are two sub visual fields on the left

column: one is to show original valid tracking area and another is to show marked result after image analysis. This user interface could update images and 3D poses in real time so that it completely supports registration and tracking system to tack target in continuous freehand surgery.

3.5 Correction Feedback Module

Registration and tracking system not only provides a visual feedback interface about real pose of interest robot part to manipulator but also assists robot to adjust its movement during interventional operation. The blue correction feedback module receives both requested transformation matrix from manipulator and the real movement transformation matrix from tracking module. Then it will calculate correction between them and send that correction transformation matrix to robot controller for shrinking deviation. Since:

$$\boldsymbol{T_{Track}} \cdot \boldsymbol{T_{Correction}} = \boldsymbol{T_{Request}}$$

where $\boldsymbol{T_{Correction}}$ is the output correction transformation matrix, $\boldsymbol{T_{Request}}$ is the requested target transformation matrix, and $\boldsymbol{T_{Track}}$ is the real movement transformation matrix obtained by tracking module. So the calculation of correction matrix could be expression as:

$$\boldsymbol{T_{Correction}} = \boldsymbol{T_{Track}}^{-1} \cdot \boldsymbol{T_{Request}}$$

where $\boldsymbol{T_{Track}}^{-1}$ is inverse matrix of $\boldsymbol{T_{Track}}$. Then $\boldsymbol{T_{Correction}}$ will be outputted to downstream robot controller by an IO port for future use.

3.6 Fiducial Frame Module

The fiducial module is the only hardware part in system. It would typically be attached near the distal end of the robot arm for the purpose of getting target tissue image and surgical tool position synchronously. Moreover, resonant coil was wrapped on the exterior surface of the fiducial frame for decreasing imaging time so that this system could be used to tracking some real-time movement during surgery like involvement of freehand operation, see Fig. 3-6. The sophisticated design of fiducial frame with non-ferromagnetic resonant coil wrap will achieve high MRI compatibility and

full DOF tracking ability with minimal image distortion for MRI-guided surgery. Detailed description about fiducial frame is in Chapter 4 and resonant coil wrap is in Chapter 7.

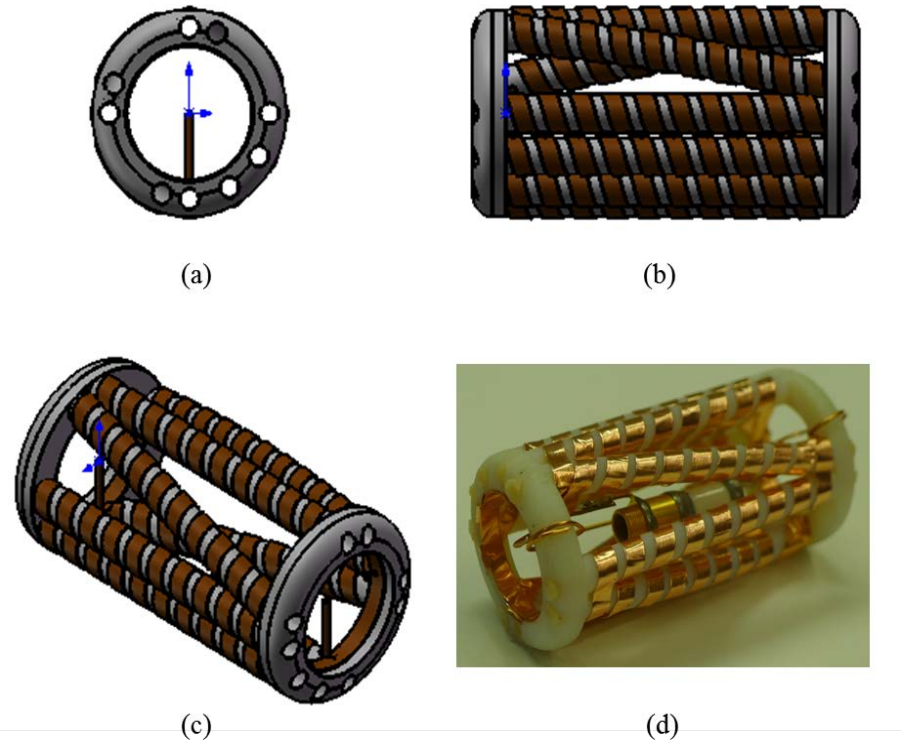

Fig. 3-6: CAD design of fiducial frame with coil wrap: (a) front view, (b) lateral view, (c) oblique drawing and (d) manufactured object.

3.7 Data Transmission and Coordination Among Modules

Different modules in the registration and tracking system achieve data communication with each other by two ways: direct connection and network link. Since direct connection undertakes to transmit massive DICOM image stream, direct modules should be set to not only connect with MR scanner computer or run on MRI console directly but also communicate on unidirectional transmission between each other in order to guarantee real-time processing. While network link would be allowed to exchange information among relative modules in bidirectional way as DIOCM sever buffers the DICOM image stream and shrink task load of data transmission to focus on small valid tracking area only. The data flow of whole system was optimized by rationally utilize these two connection methods.

Chapter 4

Fiducial Frame Design

In light of restricted workspace and 6-DOF stereotactic tracking requirement, the space-contracting multi-helix mesh was chosen as a preferred approach for our fiducial frame designs. We aimed to combine a complex registration pattern in a more compact configuration but with a relatively decreased manufacturing complexity. Many basic types of cylindrical helix mesh were designed and compared at early design stage. Then the final design was given after integrating their advantages.

4.1 Analysis of Initial Prototype Fiducial Designs

We are focusing on some similar designs all based on the elliptical and helix pattern configuration in Chapter 1. All of them are utilized cylindrical tube as main body shape with multi-helix or elliptical mesh inside to minimized volume taken by the fiducial itself in the assembly of the full system. All testing prototypes are design on a cylindrical tube with 15mm inner diameter, 5mm wall thickness and 5cm length for consistency in the evaluation, but the approach can be readily scaled up or down. The detectable and curved tubes inside are consisted of tunnels with 3mm diameter circular normal section.

4.1.1 Mesh Design of Six Identical Helical Curves

The first design is based on a simple straight wireframe that is wrapped around a cylinder. The geometry of the mesh is generated by projecting the six diagonals in the cylinder against its surface.

All helical curves have same screw pitch and precession direction but just equidistant initial phases. Adjacent helical curves keep the same phase difference with each other along the cylinder, see Fig. 4-1.

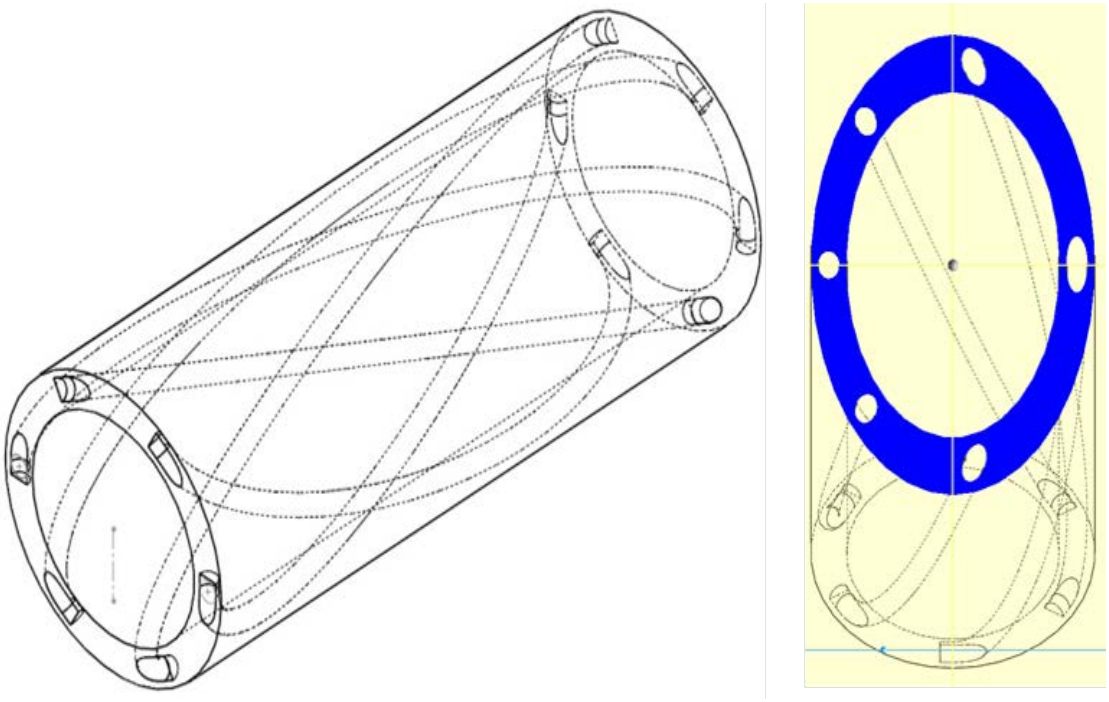

Fig. 4-1: Mesh design of six helical curves, isometric image (left) and example cross-section (right)

This design allows for high density mesh for more registration points per cross-section. A typical cross-section of the sample gives enough information to define two of the angles about the fiducial orientation in the 3D space. It also could elicit the 2D position of central axis in cylindrical plane, however, could not provide the cross-sectional depth along the central axis as well as twist of cylinder itself. Thus this fiducial will be suitable for only 4 DOF detection. So the geometry of this mesh cannot insure that all possible cross-sections are detectable.

4.1.2 Mesh Design of Two Helical Curves and Two Straight Lines

The second design is based on a standard planar Z-frame mesh as discussed in the Chapter 1. The planar shape is projected onto the cylindrical surface so that the tubular mesh pattern gets a better spatial filling across the surface of the cylindrical wall to maximize detectable readability. This mesh

is consisted with two helical curves and two straight lines. Two helical curves have same screw pitch and precession direction but with 180° phase difference. Two helical curves touch two straight lines at each end of cylinder, see Fig. 4-2.

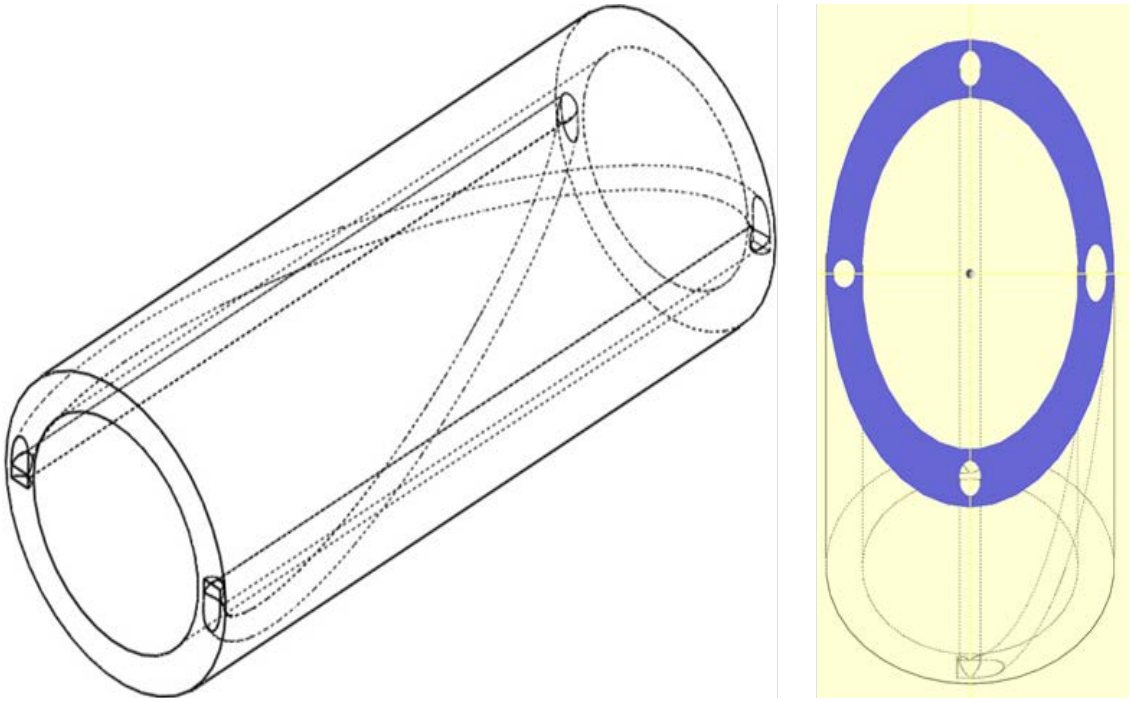

Fig. 4-2: Mesh design of two helical curves and two straight Lines, isometric image (left) and example cross-section (right)

This design allows for registration of all 6DOF of the fiducial pose theoretically as cross-section will directly give not only all three parameters for the rotation but also other two of the parameters for the position of the cylindrical axis. Especially, the varying spacing between the mesh grid tubes provides information for the position along the cylindrical axis in the coordinate space of the fiducial frame. One defect is this design provides a low density mesh to reconstruct cross-sectional ellipse duo to only four registration points per cross-section.

4.1.3 Mesh Design of Four Various Gradient Helical Curves

The third design is based on the design principle of multi-helix design. And more specifically to provide variation in the spacing between the mesh grid wires as a function of the position along the central axis. However, instead of projecting a planar Z-frame on a cylindrical surface, it utilizes

complex geometry typically described in a cylindrical coordinates – various gradient helical curves. The design utilizes four helical curves with incremental screw pitch and non-equidistant initial phases. All helical curves has slightly different pitch to each other which makes the relative circumferential position between them varies with the position along the central axis, yet none of them overlaps with other. The structure idea is shown in the Fig. 4-3.

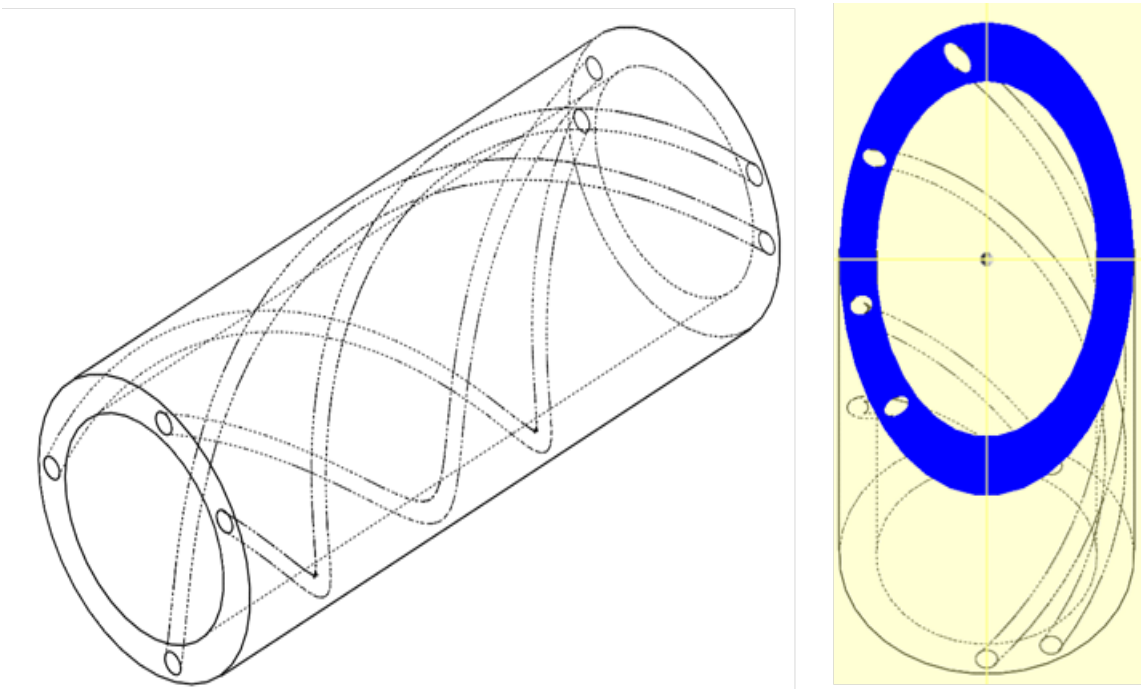

Fig. 4-3: Mesh Design of Four Various Gradient Helical curves, isometric image (left) and example cross-section (right)

Just like the second design, this design allows for the registration of all 6-DOF of the design in theory. The resulting geometry is almost identical in mathematics to the second design, but the geometrical generation is based on parameters in the cylindrical coordinate system rather than the Cartesian system as it is in the case of the second design. This simplifies the mathematical description of the fiducial and its error analysis in projected polar coordinates. But it will bring in many transformations in the image analysis which is using Cartesian system as coordinate system for each pixel. It will increase complexity and robustness of the tracking algorithm in the next step.

4.1.4 Detection Robustness Analysis of Basic Fiducial Prototype Designs

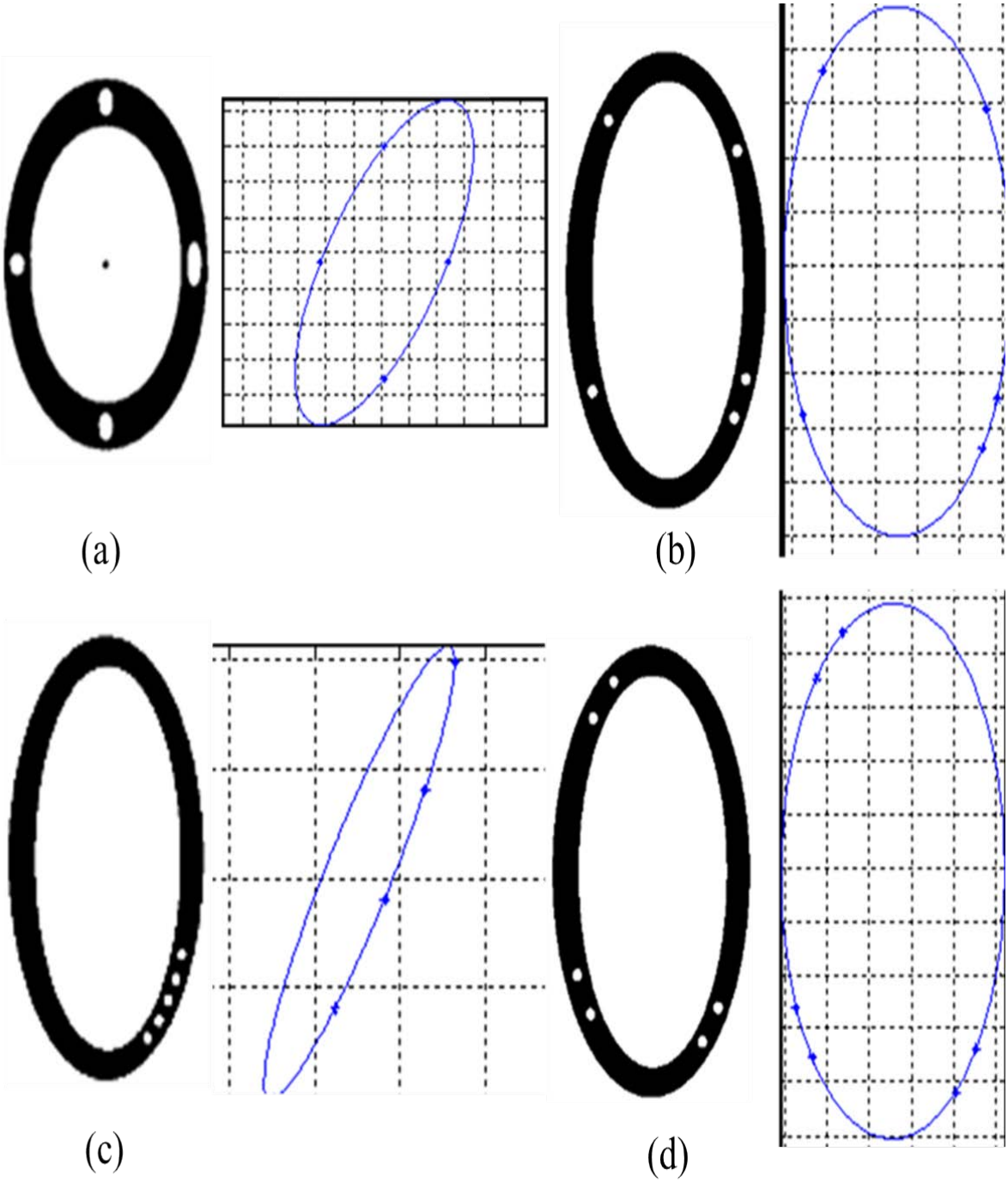

Fig. 4-4: Error of fitting caused by the lack of number of detected points (a) and poor distributions of detected points (c) for the ellipse detection. (b) and (d) are correct results after taking remedial measures.

The range of reliability of detection of the pose of the cross-sectional image is mainly based on the range of reliability of the detection of the cross-sectional ellipse which is fitting from mesh pattern. So the design of mesh pattern will directly determine the reliability of detection. Furthermore, ellipse fitting is closely dependent on the number and distribution of the detected spots around the circumference of the fiducial's cylindrical tubular mesh pattern. Fig. 4-4 lists two common errors and corresponding remedial methods causing by lack of number of detected points and poor distribution of detected points respectively.

All of prototype designs before suggested at least 4 points are necessary to accurately estimate centroid of the wire mesh points by fitting them into an ellipse, but this does not guarantee a precise estimation of the major and minor diameter of that ellipse, which will be strong relevant to the accuracy of detection procedure in the next step, see Fig. 4-4(a). So it was determined that at least 5 points are needed even though 4 points is enough for determining 6-DOF technically. The more points will better improve detection reliability and stability obviously since they narrow the fitting uncertainty. Besides the number of detected spots, how detected spots distribute is another essential factor which may cause unexpected problems, see Fig. 4-4(c). That is, whatever cross-sectional images we take, we have to make sure all detected points are distributed equably in at least three quadrants of transvers plane.

4.2 Proposed Final Fiducial Design

4.2.1 Mechanic Structure

The final design utilized the depth detection technique of identical multi-curves along with higher density mesh of mixture of straight lines and helical curves for improving both detection accuracy and stability in the detection algorithm. This design of registration and tracking fiducial frame is named as Cylindrical Helix Imaging Coordinate (CHIC) fiducial frame [36] which utilizes the similar technique as Brown-Roberts-Wells (Z-frame) did [25,37] to detect cross-sectional depth information by a higher density of tubular mesh shifting along central axis regularly, see Fig. 4-5.

The high density of mesh pattern has nine interior imaging tubes: six straight lines and three helical curves. The unique pattern of these tubes allows detection of all 6-DOF at any arbitrary pose by using only ONE slice image, so it's a single slice based image recognition technology.

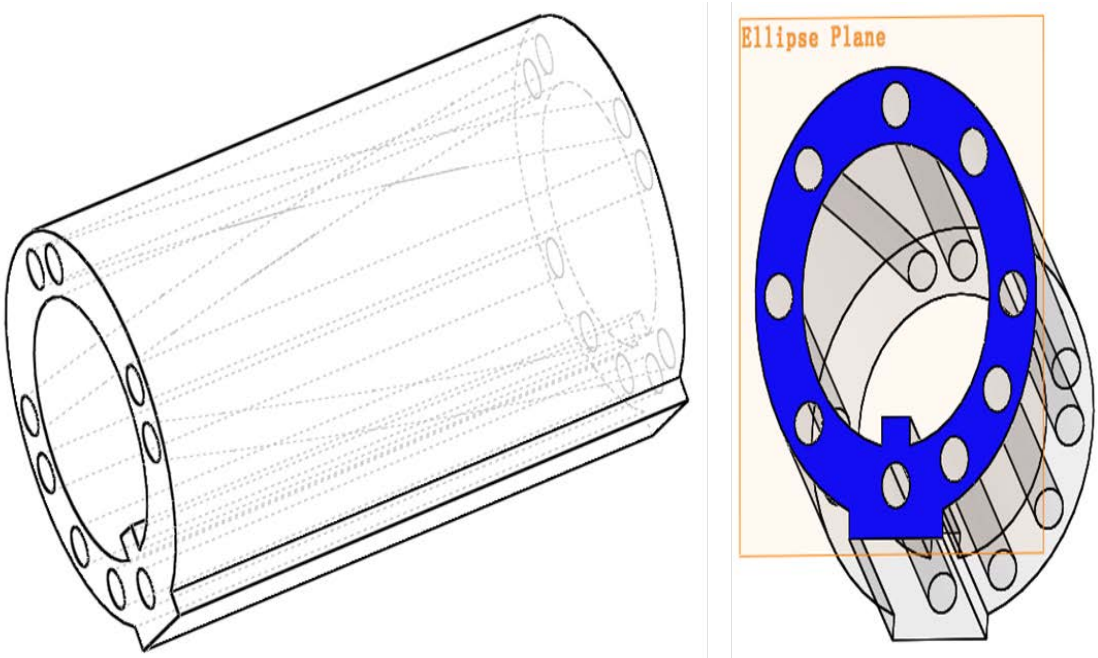

Fig. 4-5: CHIC frame fiducial CAD model (left) and unique registration elliptical mesh pattern in cross-section (right).

The main body of fiducial frame which was made by 3D printing is a tubular cylinder with height of 50mm, external diameter of 30mm, inner diameter of 20mm and tube mesh diameter of 3mm, yet all these sizes are scalable for other applications. Interior tubular mesh was filled with high MRI contrast gelatin or gadolinium fluid and provides ample tracking spots in the cross-sectional image to guarantee detection accuracy and stability of image analysis algorithm. For the sake of meeting the specifications listed in design requirement, the amended CHIC fiducial frame is extend to a tilt angle of 63.5˚ for a cross-sectional imaging in the midpoint of the fiducial center axis and to approximately 31˚ in the central range of 35mm along the axis where each blue helix tube shown in Fig. 4-7 doesn't touch close red straight tube at both end as shown in Fig. 4-6.

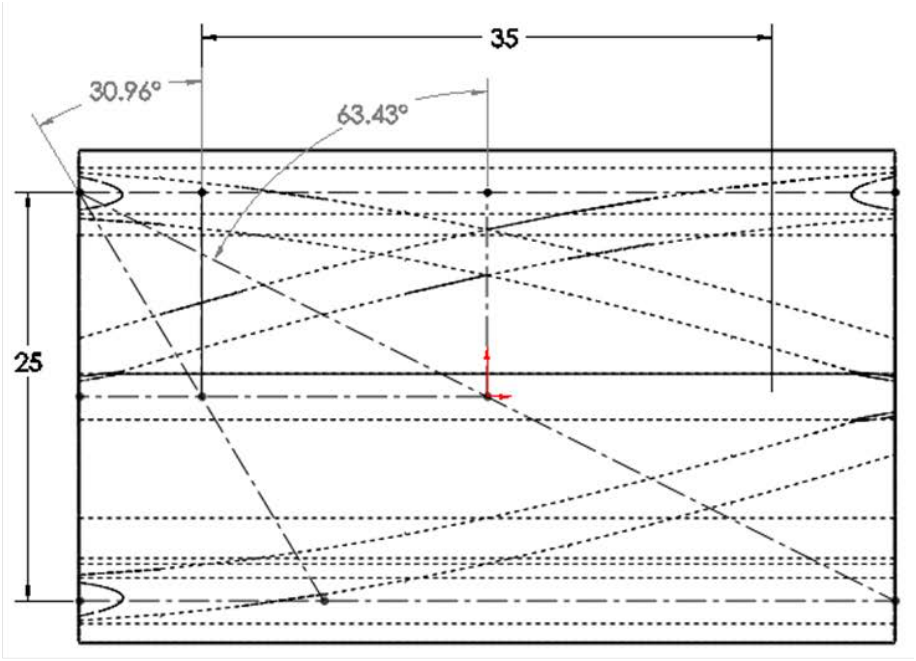

Fig. 4-6: (a) Lateral perspective view of the CHIC fiducial frame to show measurement range for the registration and tracking. (b) Real object of 3D printed CHIC fiducial frame. (c) Top view of CHIC fiducial frame with parameter annotation

Fig. 4-7 shows only three blue helix tubes change their position when cross-section shifts along the central axis. So the blue spots are used for getting cross-sectional depth information and called axial position markers. While there are four red straight tubes which always keep a cruciate position with each other. These fixed cruciate markers are mainly used for reconstructing ellipse in ellipse plane and reference points for calculating blue tubes' rotation angle. Each blue axial position marker keeps a 20° included angle offset δ with close red fixed cruciate marker respectively at both cylindrical ends in order to always keep identifiable distance for image recognition even at the extreme pose of the scanning plane. The last are two green straight tubes called axial twist markers which do not divide the quadrant where they belong equally but forms a 25° included angle with close red fixed cruciate marker at central point respectively. They make four quadrant of ellipse plane, whatever blue tubes shift, become an asymmetric distribution so that we can get the rotation of CHIC fiducial frame itself along central axis. And, they improve the accuracy of ellipse fitting, too.

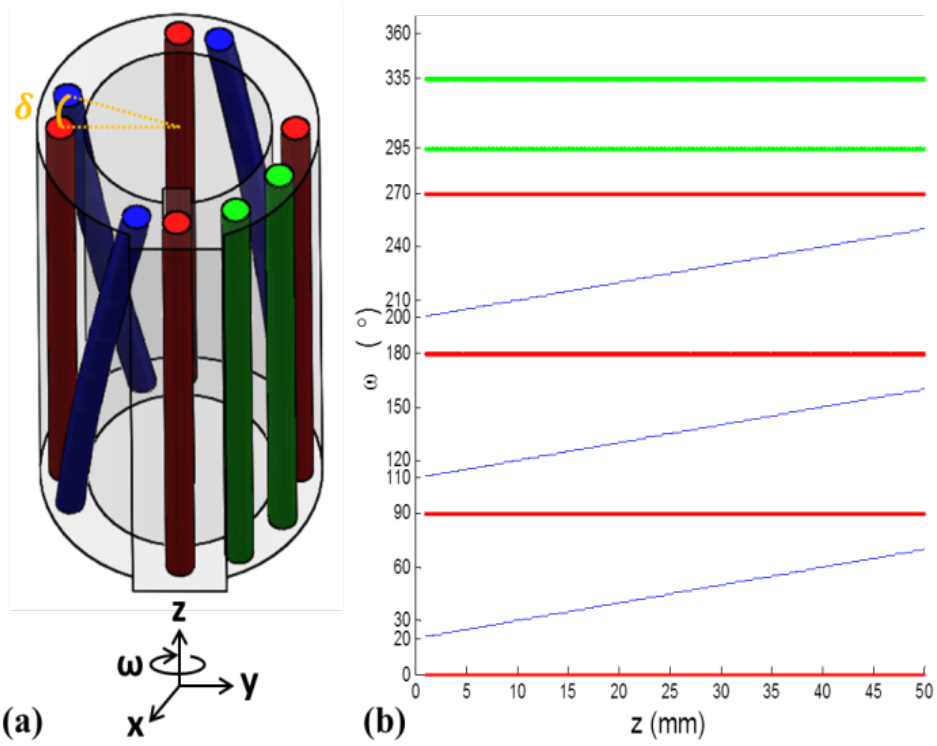

Fig. 4-7: Tubular mesh position, ω, shifts along central axis, z. The CAD drawing of CHIC fiducial frame includes different type of tubes with different colors in (a) and corresponding plot in (b).

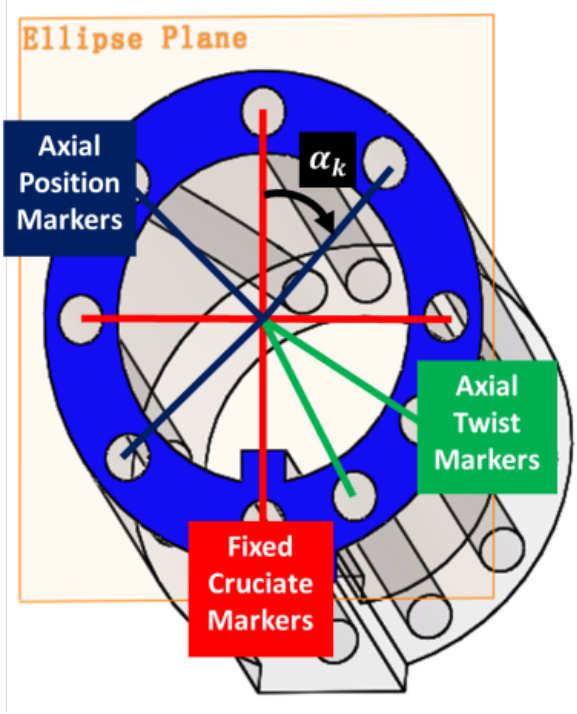

Fig. 4-8: Unique registration pattern of tubular mesh.

Detailed functional description of unique registration pattern of tubular mesh is shown in Fig. 4-8. Axial position markers (red cross) and axial position markers (blue line) to determine the depth along central axis, axial twist markers (green angle) to determine the twist angle and all centroid of tubes were fitted into elliptical curve to determine the pose of ellipse plane.

The further detection process relies on a machine vision techniques based image analysis for three aspects: the centroids measurement of each individual spots forming by detectable tubular mesh in cross-section, the central axis as well as corresponding depth information of the elliptical cross-sectional plane, and the determination of the 6-DOF pose (3 DOF in translation and 3 DOF in rotation), see Fig. 4-9. The systemic description of machine vision based image processing algorithm and mathematically stereotactic principle for using this fiducial data to estimate the full 6DOF parameter set are discussed in the Chapter 5.

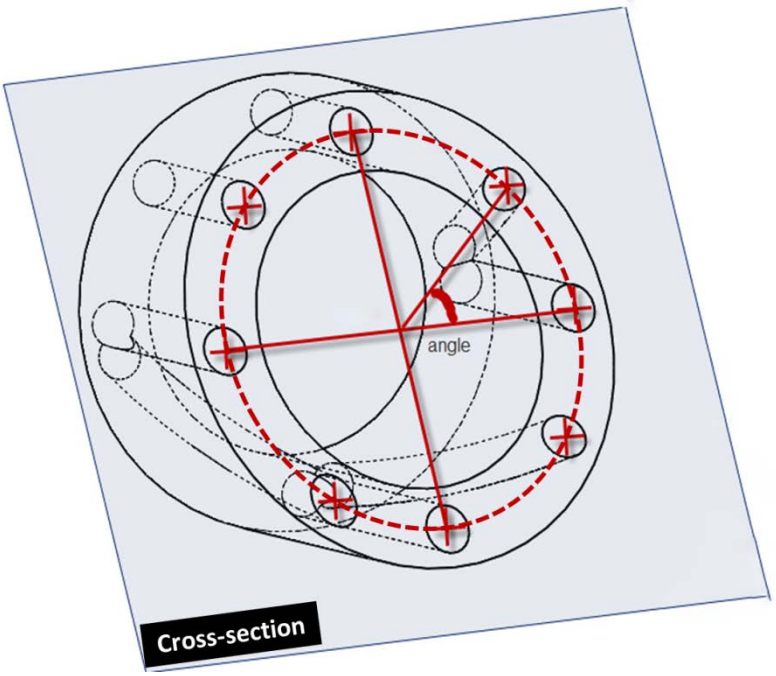

Fig. 4-9: Further detection process in the image analysis

4.2.2 Manufacturing and Materials Parameters

- **Main Body**

The fiducial is designed to be fabricated through a 3D printing process. The manufacturing of the initial prototype parts was based on 3D printing of the fiducial frame body by a fused deposition modeling (FDM) machine available at the facilities of the ME department of WPI (Stratysys Dimension SST 1200ES). Later prototypes of the CHIC fiducial used for MRI trials were manufactured on the newly arrived high resolution Objet260 Connex 3D printing machine. The Objet260 Connex is capable of spatial resolution better than 0.1mm with the horizontal layer thickness ranges from 0.025mm to 0.152. The typical accuracy for the machine is 20-85μm for features below 50mm, and up to 200μm for the full model. In practice a better resolution could be achieved by carefully aligning the crucial features of the design with the manufacturing axis.

Due to the physics of the deposition process of the FDM rapid prototype material, the structures may have tiny porous and will not hold liquid for long time. However, several treatment

techniques of the surface are available that can alleviate this problem and provide suitable manufacturing process for this and future designs [38]. This study also suggests a treatment process that relies on a mixture of one part commercially available sealant and 2 parts epoxy. Here are the materials that have been tested and listed in Table 4-1.

TABLE 4-1
SEALANT MATERIALS AND PRODUCTS [38]

Sealant	Density (g/cm^3)	Typical Applications
DEFT Clear Brushing Lacquer	0.90	Finish for interior wood surfaces.
IPS Weld-On 3 Cement	1.33	Cementing acrylic and other plastics; used in display items, containers, house wares, etc.
Minwax Sanding Sealer	0.85	Seals interior wood surfaces.
Minwax Oil Base Polyurethane	0.86	Protects interior wood surfaces.
PRO Finisher Water-Base Polyurethane	1.00	Coating hardwood floors and other interior wood surfaces.
Thompson's Multi-Surface Waterproofer	0.81	Protects and seals wood, brick and concrete.
BJB TC-1614 A/B	1.14	Seals porous to semi-porous material surfaces like plaster, wood, graphite and SLS models.
Hysol E-30CL	1.10	Bonding, small potting, laminating glass, ceramics, metals, and plastics.
Stycast W19 + Catalyst 9	1.09	Impregnates wrapped coils; small device potting; surface coating.
West Marine Penetrating Epoxy	0.93	Seals dry-rotted wood: repair transoms, decking, stringers and molding.
West System 105 Resin + 209 Hardener epoxy	1.15	Coating and bonding applications in extremely warm and/or humid conditions for fiberglass, composite materials, and a variety of metals.

All of these are commercially available materials and some similar items are already available at the AIM lab at WPI. Based on the study here is how these materials compare based on their pressure holding capabilities, see Table 4-2. This data is based on the ability of the treated parts to hold pressure for at least 5 minutes. In our case, we need a long term – several months or years, sealing at atmospheric pressure.

TABLE 4-2
PERFORMANCE OF VARIOUS SEALING TECHNIQUES AND MATERIALS [38]

	DEFT Clear Brushing Lacquer	IPS Weld-On 3 Cement	Minwax Sanding Sealer	Minwax Oil Base Polyurethane	PRO Finisher Water-Base Polyurethane	Thompson's WaterSeal Multi-Surface Waterproofer	BJB TC-1614 A/B	Hysol E-30CL	Stycast W19 + Catalyst 9	West Marine Penetrating Epoxy	West System 105 Resin + 209 Hardener epoxy
Brush: 1-Coat	X	X	O	O	O	X	√	X	√	X	O
Brush: 2-Coat	X	X	√√	√√	√√	X	√√√	O	√√	O	√√
Vacuum Infiltration	-	-	X	X	-	-	√√	-	√	-	O

Pressure Held, X=0-34, O=35-69, √=70-138, √√=139-207, √√√=208-276 (kPa)
X=0-5, O=5.1-10, √=10.1-20, √√=20.1-30, √√√=30.1-40 (psi)

- **Imaging Filler Inside Tubular Mesh**

To achieve good visibility of the registration, the mesh in the fiducial body will be filled with aqueous contrast medium. The design will utilize high MRI contrast gelatin or commercially gadolinium fluid (MR-Spots, Beekley Corp., Bristol, CT) as the one shown below in Fig. 4-10.

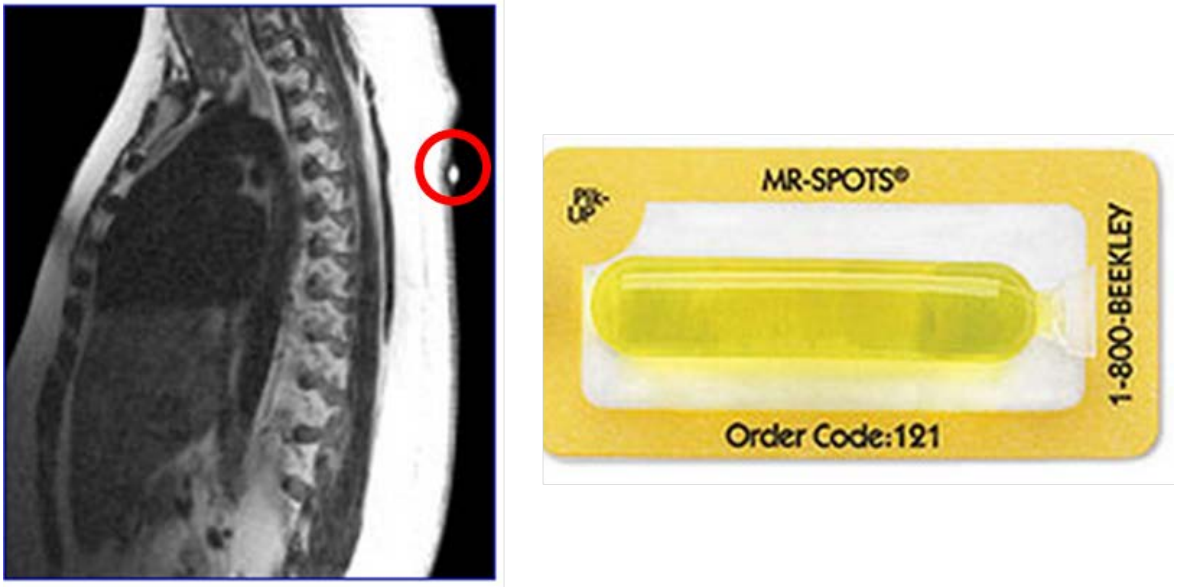

Fig. 4-10: MR-SPOTS MRI high contrast registration fluid

4.3 Application in MRI-compatible Surgical Robots

As we mentioned before, the size of CHIC frame is scalable for different applications. The CHIC frame was successively integrated on two of the WPI AIM Lab's MRI-guided surgical robots to do tracking and calibration under MRI guidance, see Fig. 4-11. Its powerful 6-DOF registration and tracking ability not only gives linear tracking for percutaneous interventions robot but also provides stereotactic location for neurosurgery robot. These examples are powerful demonstration that this compact fiducial frame could be widely implanted onto various robots or device for working synchronously in the restricted MR environment. Moreover, if we change the filler insider the tubular mesh into different contract media using for other imaging technique like CT or SPECT, the CHIC fiducial can be easily served for robot getting tracking information under guidance of corresponding imaging technique.

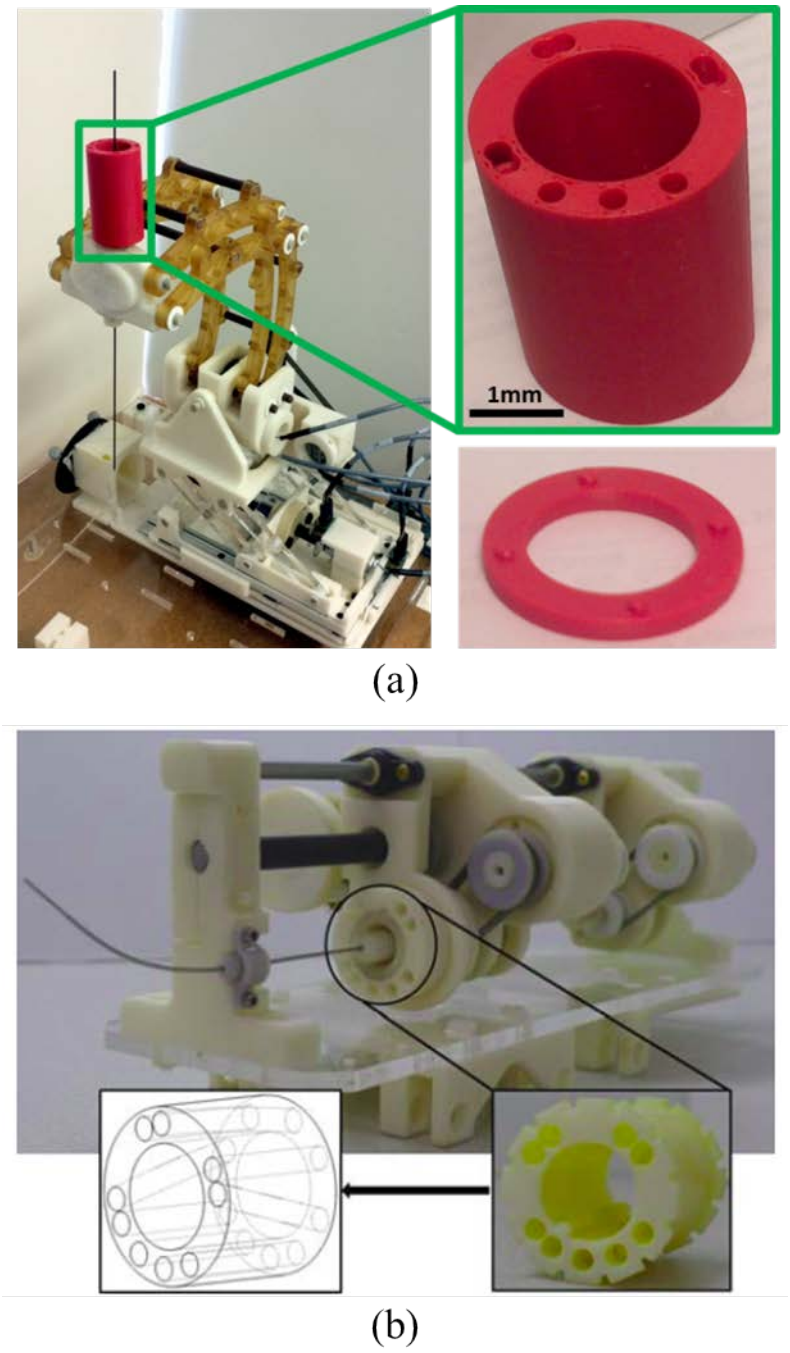

Fig. 4-11: CHIC frame fiducial frame integrated on WPI AIM Lab's (a) stereotactic neurosurgery robot [36] and (b) linear percutaneous interventions robot [39].

Chapter 5

Stereotactic Tracking Methods

The stereotactic detection procedure is divided in several sub-procedures and each one of them determines different parameters of the stereotactic 6DOF information from cross-sectional image step by step. Every one of them is limited in detection range by the geometry of the design of the fiducial frame. And then a software simulation was launched to generate many mock cross-sectional images under different pose with artificial MRI noise. The tracking algorithm will be run to evaluate these images with known pose to test the both accuracy and robustness of the tracking methods.

5.1 Image Recognition

The image recognition process relies on a machine vision technique which is realized on the Matlab platform. From only one slice of arbitrary cross-sectional image, it can automatically detect all the 6-DOF information of pose, which are three space angles of rotation: azimuth, elevation and twist, as well as three space coordinates of central point for translation: x_0, y_0 and z_0. The unique feature of this fiducial design, by the distribution of tubular mesh, will generates a one-to-one correspondence between tracking spots pattern and cross-sectional pose. Thus a single-slice based corresponding algorithm could be written to estimate the full 6-DOF parameter set for the arbitrary pose from cross-sectional imaging of the CHIC fiducial frame.

5.1.1 Centroid Measurement

The primary step of image recognition is centroid localization, which crucially decides the accuracy of algorithm. Therefore, it is also the major focus of many image preprocessing techniques.

- **Traditional Way**

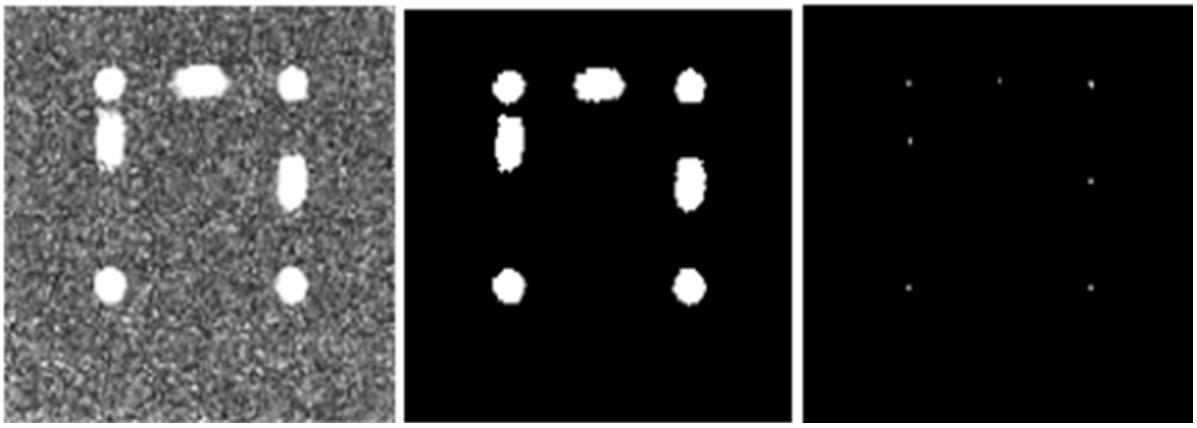

Fig. 5-1: MRI image of a transvers image of the Z-frame (left), filtration of its tubular mesh (middle) and corresponding centroid estimation (right)

A traditional way to localize the central point of each tracking spot is utilizing weighted geometric mean of valid pixel set in threshold-filtered image which is processed by using Otsus method as filter [40]. In the first step, the random noise from the MRI is filtered. This was done before on real images from Brown-Roberts –Wells (Z-frame) fiducial provided by several members of the AIM lab [41], see Fig. 5-1.

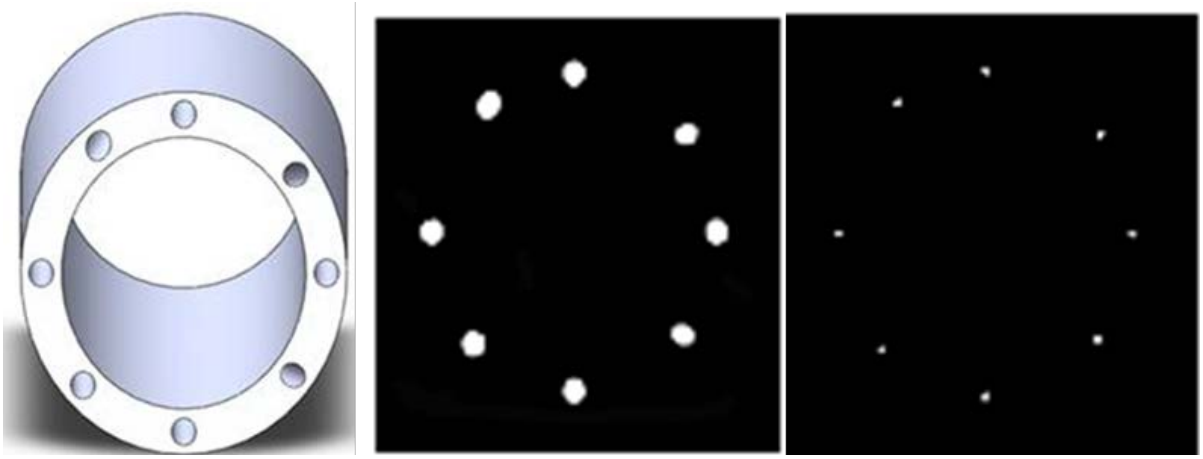

Fig. 5-2: CAD model of CHIC fiducial frame (left), an ideal cross-sectional image of its frame tubular mesh (middle) and corresponding centroid estimation (right)

The initial filtration step is capable of removing typical noise in MRI image so that software could find the cross-sections of the wire mesh and estimate the location of its centroids in image coordinate system later. The algorithm was then further developed to detect cross-section positions of

the wire mesh of simulated MRI cross-sectional images made from CHIC fiducial frame CAD model, see Fig. 5-2.

- **Gaussian distribution model**

Since it is hard to clean up some small bubbles in tracking gelatin or gadolinium fluid which could bring dark shadow in certain tracking spots during imaging which could introduce unexpected calculation error, we improved a novel method to increase the robustness of centroid measurement during raw images analysis. The intensity of each tracking spot is assumed to follow 2D Gaussian distribution. Least-square fitting is used to obtain variation range of the parameters in the following Gaussian distribution function from 5 groups, total 150 different shapes of tracking spots to build a Gaussian intensity distribution model with three known parameter spaces.

$$f(x,y) = \frac{1}{2\pi\sigma_x\sigma_y\sqrt{1-r^2}} exp\left[\frac{1}{1-r^2}\left(-\frac{(x-x_0)^2}{2\sigma_x^2} + \frac{r(x-x_0)(y-y_0)}{\sigma_x\sigma_y} - \frac{(y-y_0)^2}{2\sigma_y^2}\right)\right] \quad (1)$$

where r is correlation between x and y directions, σ_x and σ_y are standard deviation in x and y directions. x_0 and y_0 are the coordinates of tracking spot we expect to estimate from the registration.

Then we use this Gaussian intensity distribution model with three known parameter spaces to refit each single tracking spot orderly in the MRI images, see Fig. 5-3(a)(c). A comparison of centroid measurements by Gaussian model and traditional way for the same bubble affected tracking spot are shown in Fig. 5-3(b).So we can see the Gaussian model perform better especially in the situation when bubble or noise happens in the tracking spot.

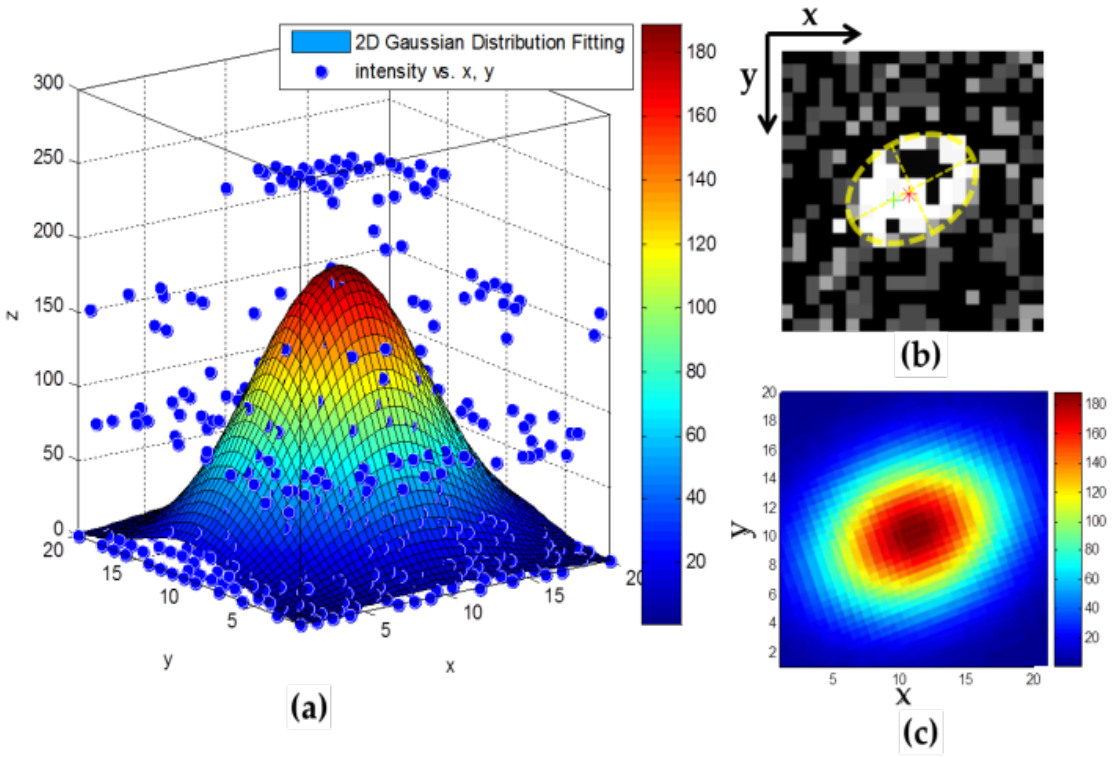

Fig. 5-3: (a) Using Gaussian distribution model to refit pixels' intensity for one bubble affected tracking spot. (b) "+": the centroid gets from traditional way. "*": the centroid gets from Gaussian intensity distribution model. (c) the aerial view of Gaussian distribution fitting results for the same tracking spot.

5.1.2 Ellipse Plane Reconstruction

The result of ellipse plane reconstruction also decides the accuracy of cross-sectional pose detection which in terms is dependent on the number and distribution of tracking spots generated by tubular mesh pattern around the circumference of cylindrical fiducial frame. The tubular mesh of CHIC fiducial frame provides adequate tracking spots in the cross-sectional image to guarantee very high robustness for ellipse plane reconstruction using least-square approach. Two types of failure in the ellipse fitting can be avoided: improper distribution and lack of tracking spots.

To classify tracking spots in the cross-sectional image into different types of markers, the first step is to counterclockwise arrange all tracking spots along ellipse by the coordinates of their centroids before exactly matching them into each type of markers. Then the four red fixed cruciate markers in Fig. 4-7 can be recognized by searching four tracking spots in the loops which have

successive odd or even serial number as well as the sum of included angle of each contiguous pair at central point is 360° (within a reasonable tolerance of σ = 0.5). We cannot judge fixed cruciate markers by just checking four spots which have cruciate diagonal line at central point as a result of this orthogonal cross may change to non-vertical decussation under certain cross-sectional tilt. Then the two green axial twist markers which make an asymmetric distribution within four cruciate quadrants will be found by checking the number of tracking spots in each cruciate quadrant. However, here we have to do a double-check to make sure we make right recognition at first step before marking the rest of spots as blue axial position markers because the blue spots may shift into certain conditions where they can form the same crossed diagonal line at central point together with one of green spots just totally same as four red fixed cruciate markers do. So we check whether the two included angles between each green axial twist marker and close red fixed cruciate marker at central point are both around 25° (within the same tolerance σ = 0.5), and we need to repeat the program to find next four crossed spots in loop if they are not. Once marking all type of markers, we can adopt least-square method to fit their centroids into an elliptical curve to reconstruct ellipse plane, see Fig. 5-4.

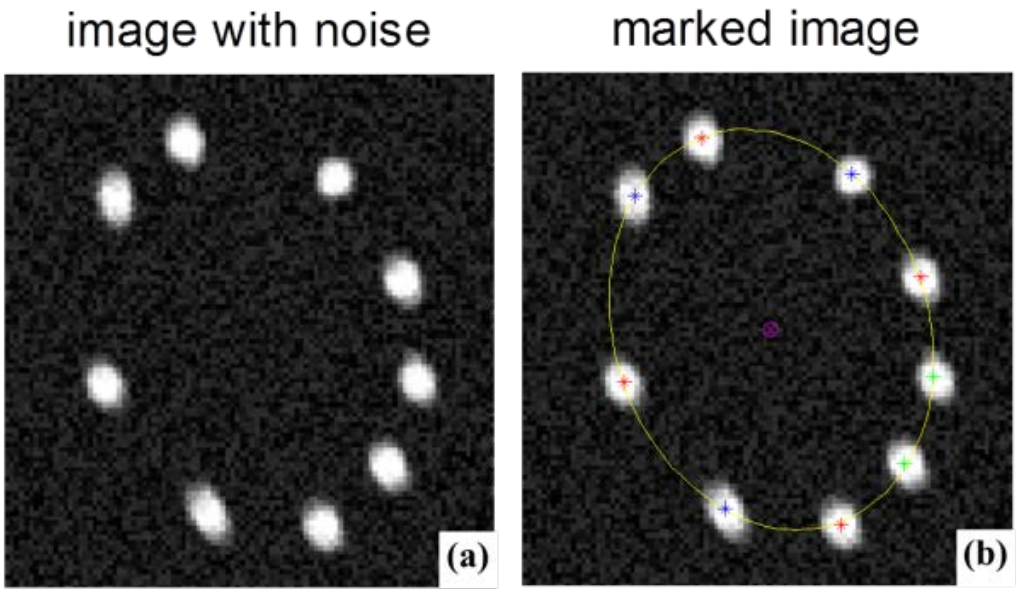

Fig. 5-4: (a) Valid tracking area with noise, (b) Ellipse plane reconstruction after measurement and classification of the centroids.

5.2 Mathematic Model

Unlike some of published approaches for image based registration adopting multi-slice images to improve accuracy of spatial information [42], the registration algorithm of this fiducial frame utilizes a single-slice based fiducial registration method which could skillfully extracts high-accuracy 6-DOF information from sophisticated spots pattern. The function of different markers will be explained in detailed through this part, including sections of reference frame for rotation and extraction of 6-DOF information.

5.2.1 Reference Frame Definitions

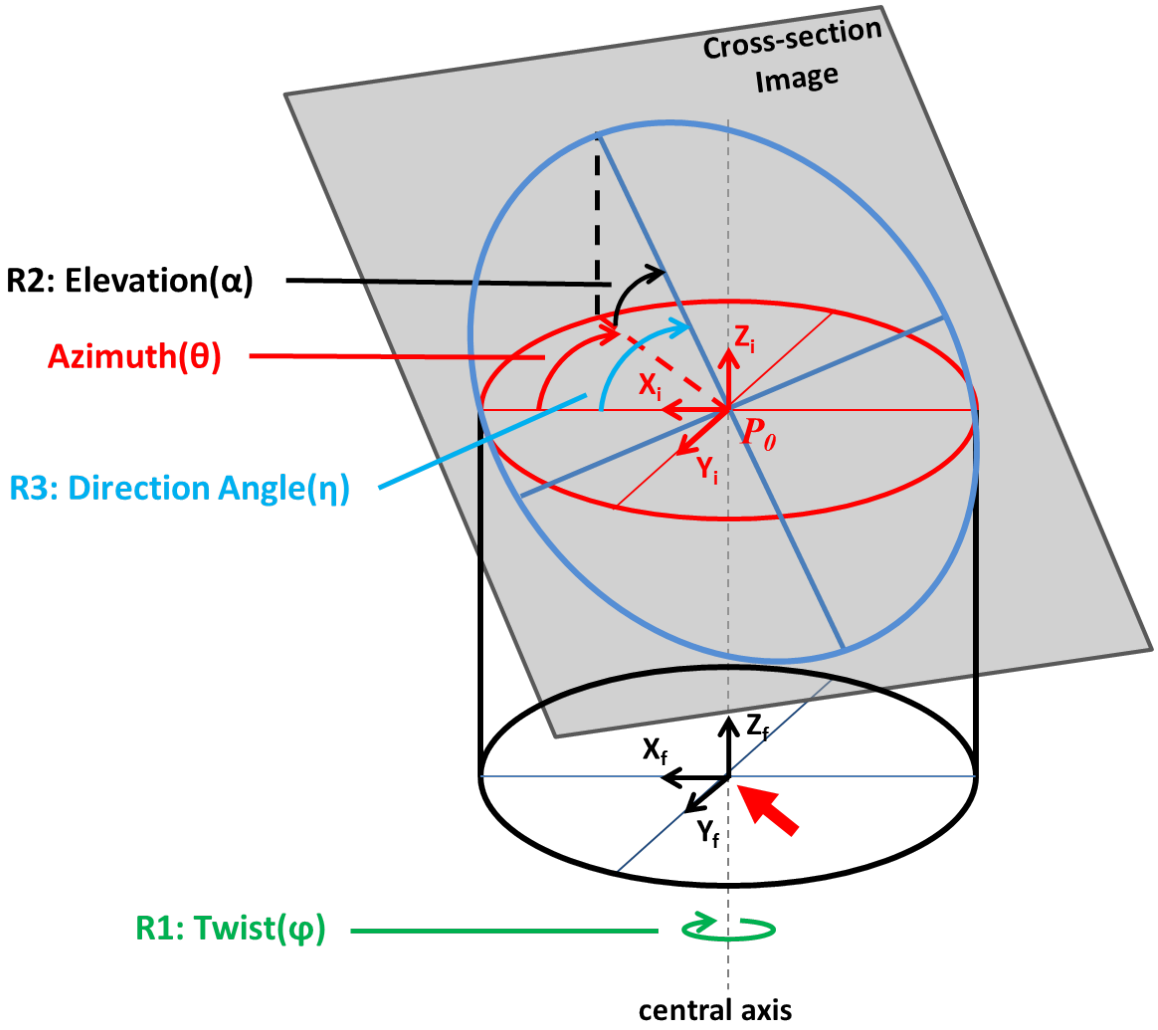

Fig. 5-5: Reference frame for CHIC fiducial frame. F_f (red arrow)is adhere to central point of cross-sectional image and it is the primary fixed frame adhering to initial point of robot arm or needle.

The Reference frame for Single-slice based Registration is illustrated in Fig. 5-5. The gray plane is cross-sectional image including a central point P_0 while red circle plane is corresponding normal projected plane for P_0. The black coordinate frame F_f (red arrow) on the bottom is set as primary fixed frame adhering to initial point of tubular robot end effector, and all steps of sub-rotation must be done with respect to it. The central point $P_0(x_0, y_0, z_0)$ where F_i adhered to, includes all three DOF information about translation. F_i is internally calibrated and related to the primary frame F_f with same x_0 and y_0 but a certain displacement along central axis which equals depth information z_0. Other three DOF about rotation will be achieved by three sub-rotation steps noted as R1: Twist (φ), R2: Elevation (α) and R3: Direction (η). Azimuth angle (θ) is a forward correction which cannot be measured directly from cross-sectional image and it will be introduced further later.

5.2.2 Calculation of 3 Rotational DOF

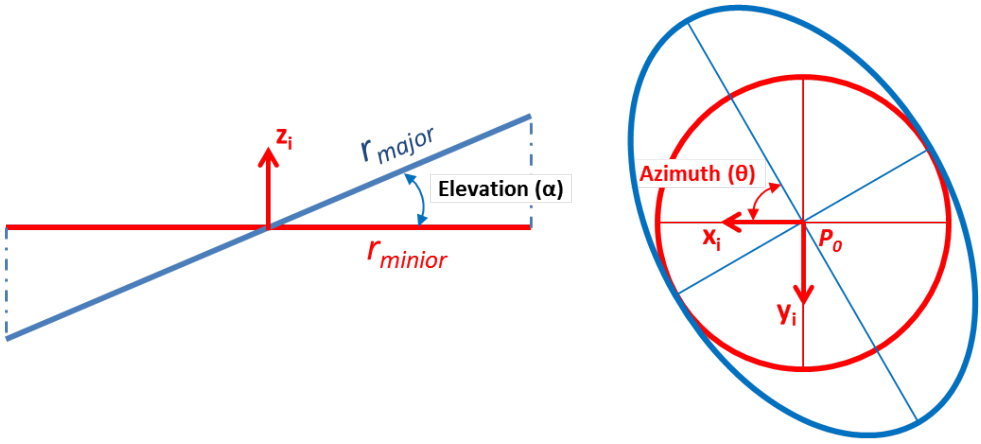

(a) (b)

Fig. 5-6: (a) Side view of reference frame for Elevation angle evaluation. (b) Top view of reference frame for Azimuth angle evaluation

The cross-sectional rotation can be described completely by three angles: twist angle (φ), elevation angle (α) and direction angle (η). The Twist angle can be directly measured by the mean

rotary angle of four red fixed cruciate markers diverging from each original 0°, 90°, 180° and 270° position referenced by two green axial twist markers. Here the pairwise symmetry of four fixed cruciate markers will counteract the distortion of included angle between each other which is caused by cross-sectional tilt during averaging process. The Elevation angle, just as its name suggesting, is the projective angle of the major to minor axis of the ellipse equation at central point P_0 after ellipse plane reconstruction, see Fig. 5-6(a):

$$Elevation\ (\alpha) = cos^{-1}\left(\frac{r_{minor}}{r_{major}}\right) \tag{2}$$

where r_{minor} and r_{major} are minor axis and major axis of ellipse equation respectively.

The direction angle can be immediately measured after ellipse plane reconstruction, and which is the angle between major axis of ellipse and x axis as shown as φ in general parametric form of ellipse equation:

$$\begin{cases} X(t) = X_c + a\cos t\cos\varphi - b\sin t\sin\varphi \\ Y(t) = Y_c + a\cos t\sin\varphi - b\sin t\cos\varphi \end{cases} \tag{3}$$

where parameter t varies from 0 to 2π. Here (X_c, Y_c) is the center of the ellipse, and φ is the angle between the X-axis and the major axis of the ellipse.

After the obtaining of three angles about rotation, we can reconstruct corresponding 6-DOF pose by just following a specific three steps of sub-rotation with respect to the fixed frame F_f in sequence of z, y and z again as Fig. 5-7 shows. Consider the last sub-rotation step will have after effect on twist angle that bring in an extra twist called azimuth angle (θ). Although the azimuth angle cannot be measured directly from cross-sectional image, it can be deduced by rotation rule: orbital movement will bring same spin effect on rigid body, see Fig. 5-6(b). The conversion equation can be finally simplified as:

$$\theta = \eta \tag{4}$$

therefore we have to add an amendment that subtracts the twist angle with azimuth angle to get twist angle in place of twist angle early in the first sub-rotation matrix shown in:

$$Twist^* = \varphi - \theta = \varphi - \eta \tag{5}$$

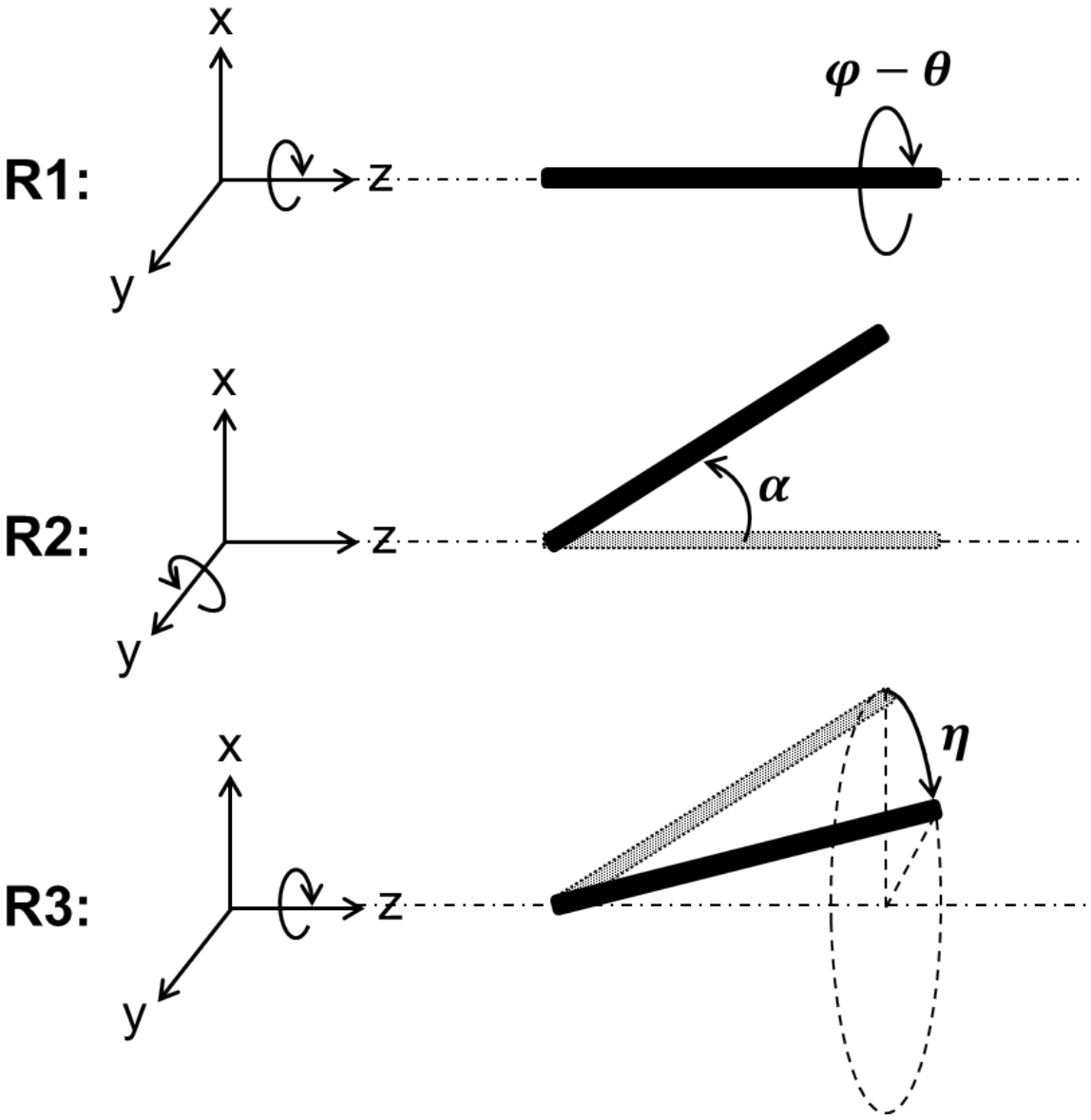

Fig. 5-7: Illustration of three individual rotation steps rotating with respect to the fixed frame F_f to achieve robot arm or needle into arbitrary pose.

Finally, because all sub-rotation are respect to the fixed frame, we multiply three sub-rotation matrixes inversely together to obtain total rotation matrix as following:

$$\boldsymbol{R}^1_{z,Twist^*} = \begin{pmatrix} \cos(\varphi-\theta) & -\sin(\varphi-\theta) & 0 \\ \sin(\varphi-\theta) & \cos(\varphi-\theta) & 0 \\ 0 & 0 & 1 \end{pmatrix} \tag{6}$$

$$\boldsymbol{R}^{2}_{y,Elevation} = \begin{pmatrix} 1 & 0 & 0 \\ 0 & \cos\alpha & -\sin\alpha \\ 0 & \sin\alpha & \cos\alpha \end{pmatrix} \tag{7}$$

$$\boldsymbol{R}^{3}_{z,Direction} = \begin{pmatrix} \cos\eta & -\sin\eta & 0 \\ \sin\eta & \cos\eta & 0 \\ 0 & 0 & 1 \end{pmatrix} \tag{8}$$

$$\boldsymbol{R} = \boldsymbol{R}^{3}_{z,Direction} \cdot \boldsymbol{R}^{2}_{x,Elevation} \cdot \boldsymbol{R}^{1}_{z,Twist^{*}} \tag{9}$$

5.2.3 Calculation of 3 Translational DOF

As we mentioned before, the central point P_0 includes all three DOF information about translation in its spatial coordinate x0, y0 and z0. The x0 and y0 can be straightforward obtained from ellipse equation after ellipse plane reconstruction while how to exactly estimate z0 is a geometric conundrum. Previous Fig. 5-8(b) in Chapter 4 shows the blue axial position markers shift their included angle with corresponding red fixed cruciate markers linearly along central axis. This can be formulized as:

$$z_k = \frac{\alpha_k - 2\delta}{\omega} \qquad (k = 1, 2, 3) \tag{10}$$

where α_k, see Fig. 4-8 in Chapter 4, is the included angle between one pair of blue and red spots, z_k is the space distance along central axis corresponding with α_k, see Fig. 4-7(a) in Chapter 4, δ is an initial angular offset which is equal in the both ends of the cylinder and ω is the pitch of the helix tube that defines this tubular mesh in dimensions of angle/distance (degree/mm). Since the length of CHIC frame is 50cm and the offset in each side is 20° which means the maximum shifting range of each blue axial position markers is 50°, the ω will be 1°/cm for every blue helix tube.

It should be noticed that this is defined on normal section along central axis of CHIC frame yet real cross-section usually stay in arbitrary pose which is not overlap with any normal section along central axis. Fig. 5-8(a) illustrates this difference: the gray plane with central point O is cross-sectional plane which contains a blue spot B cutting from one of axial position marker and a red spot R cutting from corresponding fixed cruciate marker of B. The red circle plane with central point O' is the normal section passes through B. We could only recognize dashed line angle $\angle BOR$ directly from

cross-sectional image, however, the conversion relation between space and rotation according to aforementioned definition force us to calculate solid line angle $\angle BO'R'$ where R' is projection of R on red normal section. Then we still have to calculate OO' to transfer $z_{o'}$ to z_o. The conversion from $\angle BOR$ to $\angle BO'R'$ as well as acquiring correction distance OO' will be illustrated by two steps, as shown in Fig. 5-8(b) and Fig. 5-8(c).

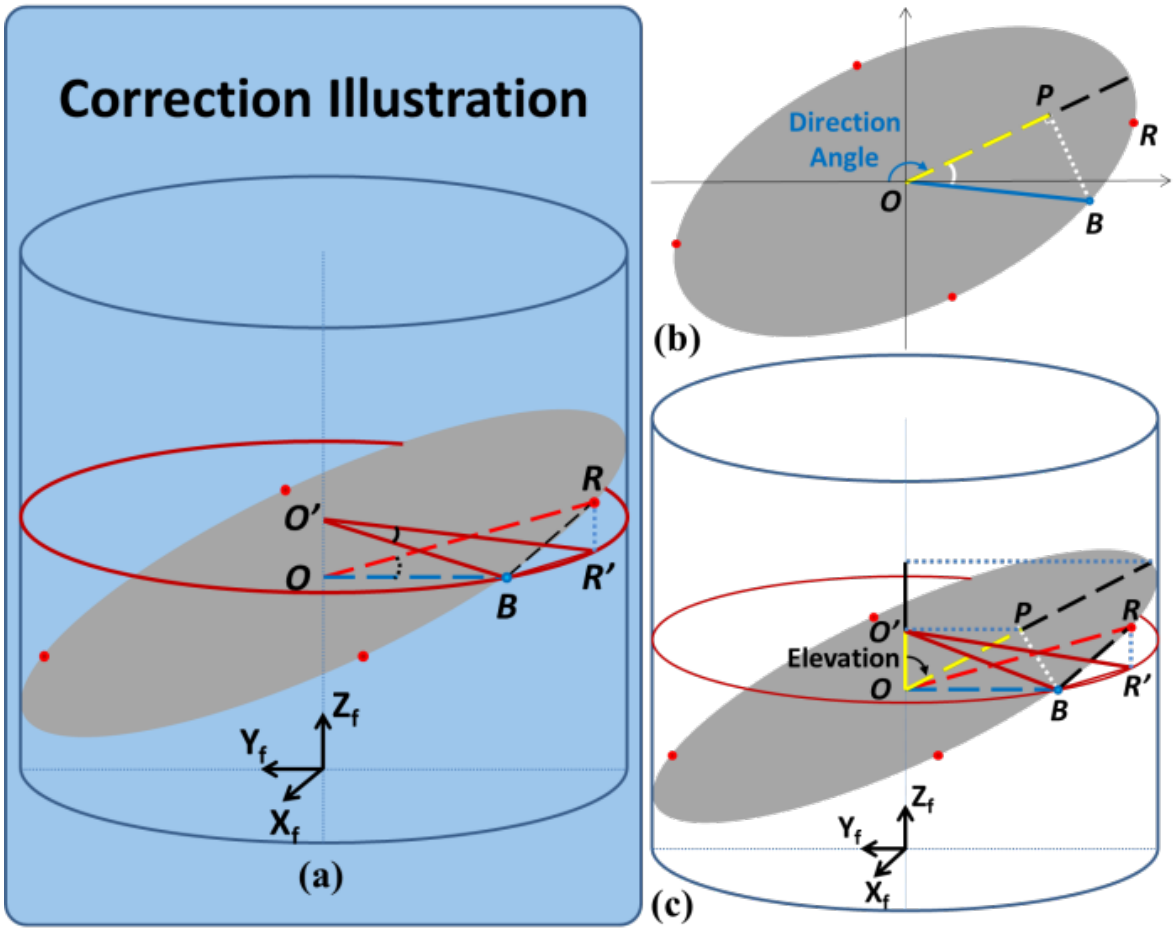

Fig. 5-8: (a) The illustration of correction from arbitrary cross-section to normal section. The gray plane with central pont O is cross-sectional plane where contains a blue spots B cutting from one of axial position marker and a red spots R cutting from corresponding fixed cruciate marker of B. The red circle plane with central pont O' is the normal section passes through B. R' is projection of R on red normal section. (b) and (c) are two steps to illustrate of conversion from ∠BOR to ∠BO′R′.

The first step will begin with the 2D cross-sectional image, see Fig. 5-8(b). OP can be calculated by:

$$OP = OB \cdot sin\angle BOP \tag{11}$$

where P is the projection of B on major axis of ellipse plane. Then we obtain OO' in the step (c):

$$OO' = OP \cdot sin(Elevation) = OP \cdot sin\alpha \tag{12}$$

where O' is the projection of P on central axis of CHIC fiducial frame. And we can do similar work to gain RR' which is projection of OR on red normal section. Next, we first get BR' by the Pythagorean Theorem:

$$BR'^2 = BR^2 - RR'^2 \tag{13}$$

Because there is $O'B = O'R = r_{minor}$ inside the red normal section, so we can reason out $\angle BO'R'$ by law of cosines:

$$\angle BO'R' = cos^{-1}\left(\frac{O'B^2 + O'R'^2 - BR'^2}{2 \cdot O'B \cdot O'R'}\right) \tag{14}$$

$$= cos^{-1}\left(\frac{2r_{minor}^2 - BR'^2}{2r_{minor}^2}\right) \tag{15}$$

Now plug $\angle BO'R'$ into (10) to estimate the depth of O' and then eliminate correction distance OO' to obtain depth of O:

$$z_k = z_{O'} - OO' = \frac{\angle BO'R' - 2\delta}{\omega} \qquad (k = 1, 2, 3) \tag{16}$$

In order to minimize error, repeat these same steps in (16) to estimate other two blue spots and finally the depth information z_0 of central point P_0 will be the average of three depth of O getting from three blue spots:

$$z_0 = \frac{\sum z_k}{3} \qquad (k = 1, 2, 3) \tag{17}$$

5.2.4 Calculation of Transformation Matrix

Most of the robot controls are depended on transformation matrix, so the last is to piece together a tracking transformation matrix T_{Track} from rotation matrix R and central point P_0:

$$T_{Track} = \begin{bmatrix} R & P_0' \\ 0 & 1 \end{bmatrix} \tag{18}$$

where R is rotation matrix, P_0' is transpose of central point vector and 0 is zero row vector with 3 dimension.

5.3 Simulation Verification

5.3.1 Simulation Method

To test the performance of the algorithm, artificial cross-sections from CAD drawings were made, see Fig. 5-9.

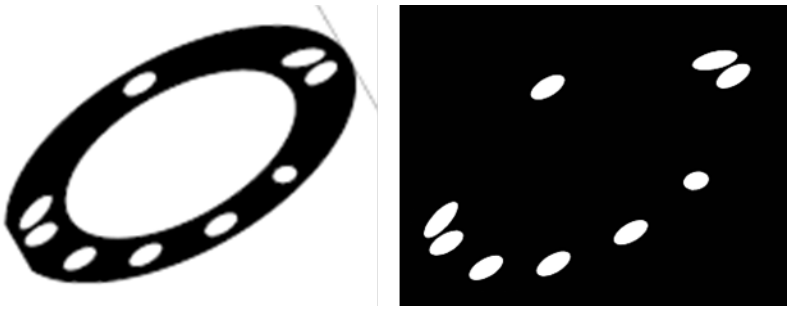

Fig. 5-9: Artificially created cross-sectional image

Artificially created white noise was added and the filtration capabilities of the registration algorithm were adjusted and tested, see Fig. 5-10.

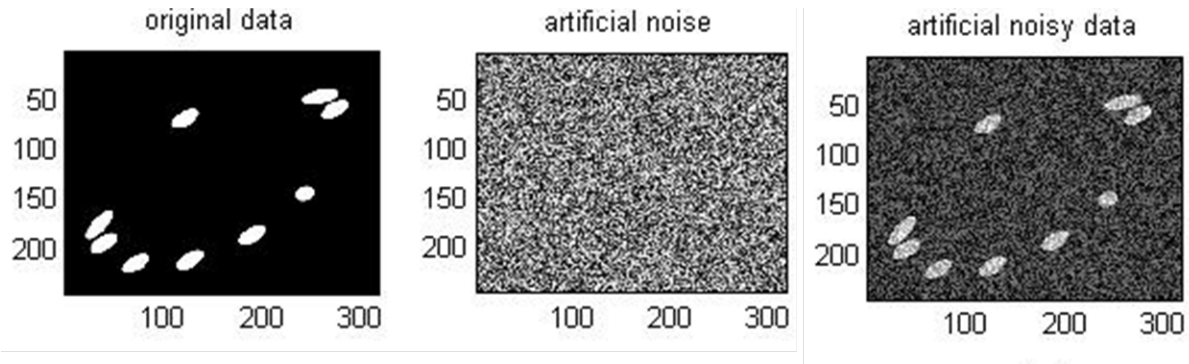

Fig. 5-10: Images with artificial noise

The tracking algorithm applies a combination of tracking spots registration, plane reconstruction and transformation matrix generation, see Fig. 5-11. The total processing time is less than 10ms.

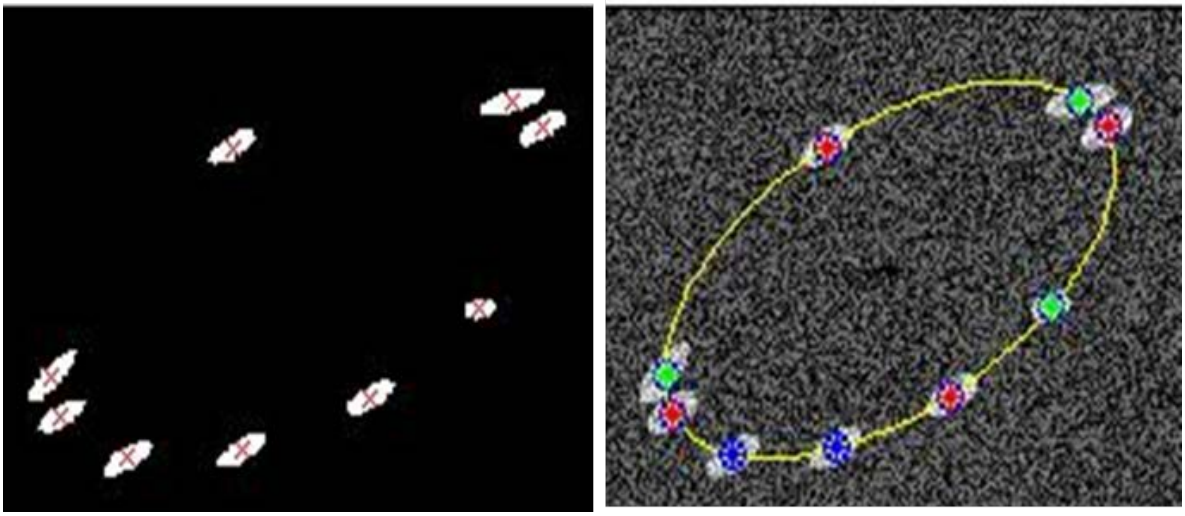

Fig. 5-11: Registration of centroids and various types of markers

At the end of the algorithm, it determines the pose and orientation of the cross-section and provides a normal vector of the cross-sectional image, see Fig. 5-12. The RMS of registration for this pose is within 0.2° for all the 3 rotational DOF.

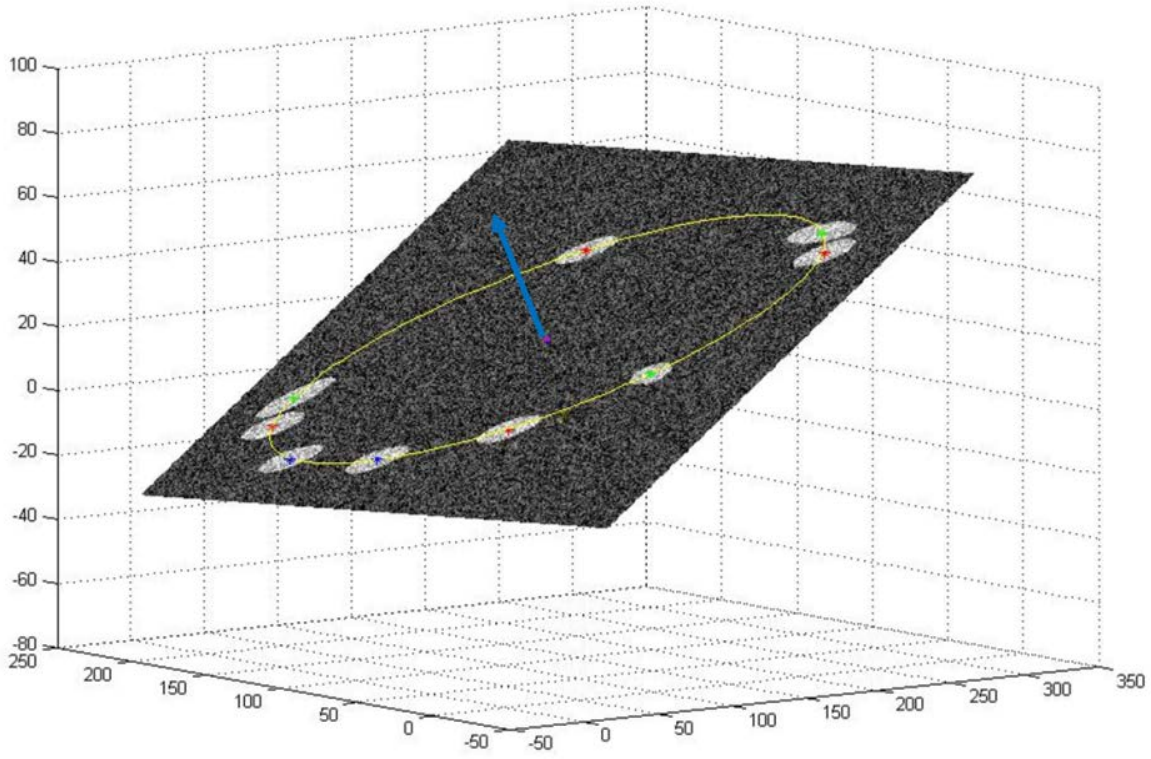

Fig. 5-12: Final registration and tracking results

5.3.2 Simulation Results

- **Artificially Generated Images for Reconstruction Simulation**

Four groups of simulation have been performed to evaluate the accuracy of the fiducial module: two groups for positioning error tests and two for orientation error tests. The simulated images setting and corresponding results are showing in Fig. 5-13.

A group of normal sections with known distances as shown in Fig. 5-13(top-left) was created. Cross-sections E to I with 5, 10, 20, 30 and 40mm to the end of the fiducial module are acquired from CAD model and used to create simulated images. The axial displacement error is shown in Fig. 5-9(bottom-left). The maximum error is 0.130mm with a standard deviation is 0.039mm.

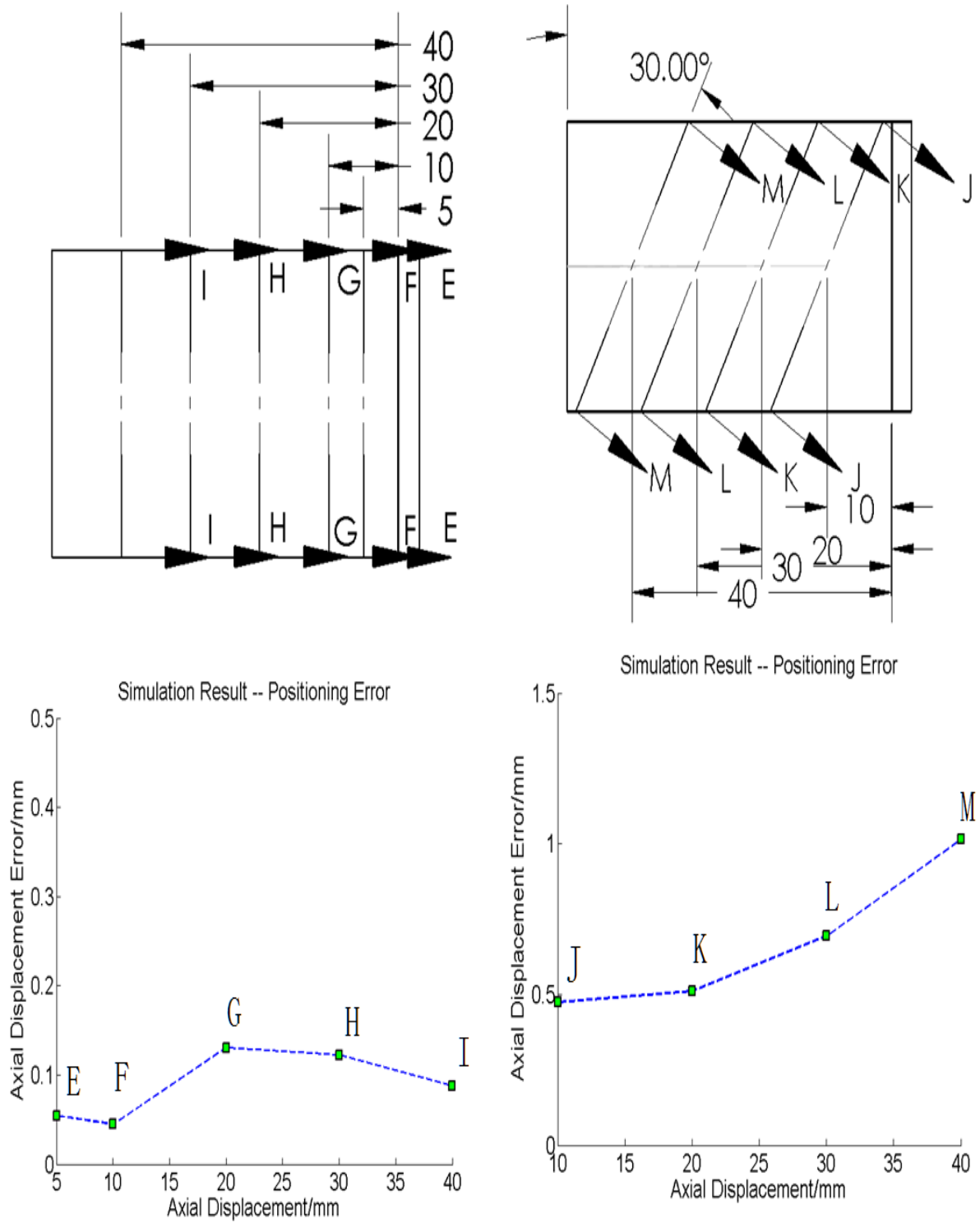

Fig. 5-13: Simulation positioning accuracy evaluation: Normal sections with known distances (top-left) and their axial displacement error (bottom-left). Tilted sections with known distances (top-right) and their axial displacement error (bottom-right).

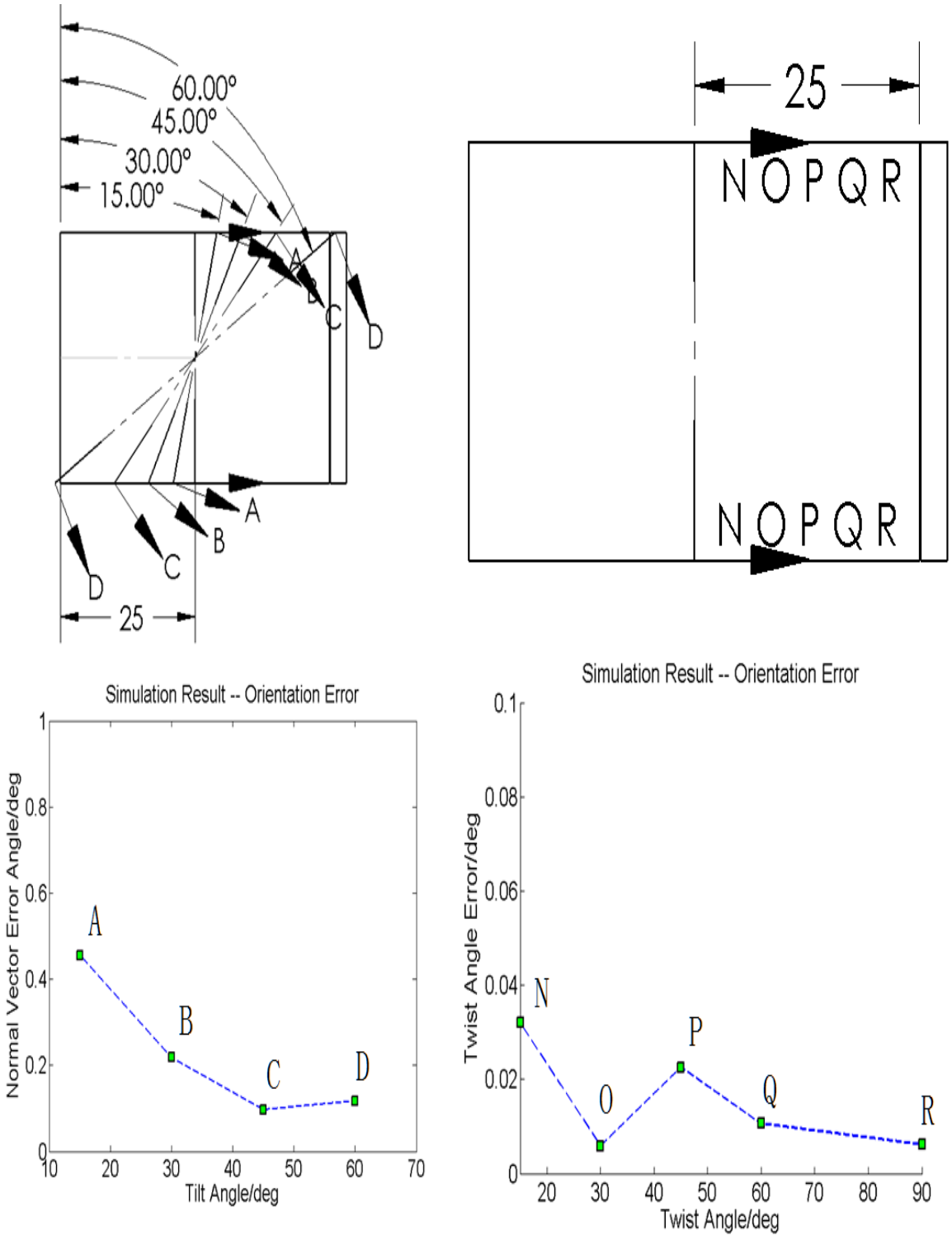

Fig. 5-14: Simulation orientation accuracy evaluation: A group of cross-sections with known tilt angles (top-left) and their normal vector error (bottom-left). A group of normal sections with known twist angles (top-right) and their twist angle error (bottom-right).

A group of tilted sections with known distances is tested to evaluate the positioning error. The cross-sections are shown in Fig. 5-13(top-right). Cross-sections J to M have the same tilt angle of 30° relative to normal section and they are 10, 20, 30 and 40mm to the end of the fiducial module. The axial displacement error is shown in Fig. 5-13(bottom-right). The maximum error is 1.015mm with a standard deviation of 0.247mm.

To evaluate orientation accuracy, a group of cross-sections A to D with known tilt angles of 15°, 30°, 45° and 60° is created as shown in Fig. 5-14(top-left). The angular error of normal vector is shown in Fig. 5-14(bottom-left). The maximum error is 0.456° with a standard deviation of 0.164°.

A group of normal sections with known twist angles was created to evaluate the twist angle error. The cross-sections of N to R with twist angles of 15°, 30°, 45°, 60° and 90° are shown in Fig. 5-14(top-right). The twist angle error is shown in Fig. 5-14(bottom-right). The maximum error is 0.032° with a standard deviation of 0.011°.

- **Original MR Images Simulation**

MR images of the fiducial module were acquired with a Philips 3T MRI scanner. The fiducial module was placed in the scanner at a random pose. The positioning and orientation accuracy are tested by taking a series of 14 images using a T2-weighted protocol, flip angle=45°, image size=256×256 pixels, pixel size=0.5×0.5mm, distance between slices=2mm. An assessment of relative accuracy on this set of images is shown in Table 5-1.

TABLE 5-1
ORIGINAL MR IMAGE ACCURACY EVALUATION

	x	y	z	Tilt	Twist
RMS Error	0.620mm	0.144mm	0.269mm	0.086°	0.006°
Standard Deviation	0.166mm	0.166mm	0.280mm	0.089°	0.006°

- **Reconstructed MR Image Simulation**

To further evaluate reliability on a large set of images with known poses, a high resolution MRI volume was acquired. This volume was then artificially resliced to generate reconstructed MR images of arbitrary, but known position and orientation. For a representative series of images reconstructed with a tilt angle of 15° relative to original MR images and with the same image and pixel size, the accuracy results are shown in Table 5-2.

TABLE 5-2
RECONSTRUCTED MRI POSITIONING AND ORIENTATION ACCURACY TEST

	x	y	z	Tilt	Twist
RMS Error	0.111mm	0.091mm	0.312mm	0.006°	0.161°
Standard Deviation	0.114mm	0.094mm	0.311mm	0.006°	0.157°

- **User Interface Tracking**

Besides static registration, we also tested the user interface module running on Matlab platform. To make sure it provided a successive result in real time to reflect target pose exactly as well as sent the corresponding correction transformation matrix to robot controller. A series of visual feedback results for tracking two DOF movements are serially shown in Fig. 5-15.

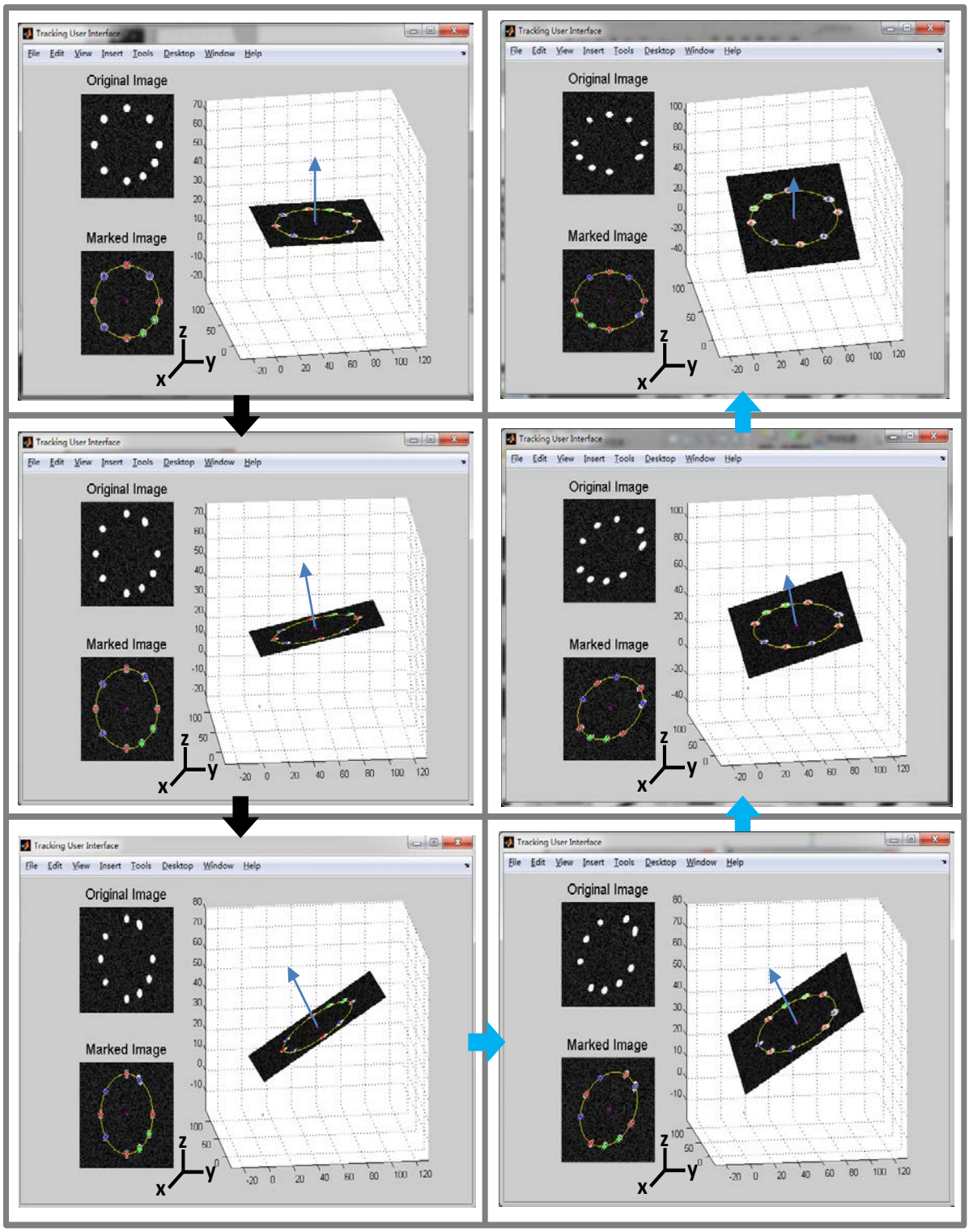

Fig. 5-15: The image plane is adapted to automatically tracking a series of elevation angle changes (black arrow) and direction angle changes (blue arrow) with respect to a fixed point.

Chapter 6

Tracking Experiments and Results

To demonstrate the tracking accuracy and MRI compatibility of this registration and tracking system, we performed many MRI scanning tasks for registration and tracking. 25 experimental groups with different poses are successively scanned along specific sequence in MRI experiment to evaluate the accuracy and robustness of tracking algorithm.

6.1 Experiments

We evaluated our registration and tracking system in a Philips 3T MRI scanner and all images were acquired with following imaging parameter: TR = 3000ms; TE = 90ms; flip angle = 90°; slice thickness = 2mm; pixel spacing = 0.5 × 0.5mm; FOV = 80 × 80mm; and matrix = 160 × 160, see Table 6-1. The experimental groups are successively scanned along depth axis $\boldsymbol{z_f}$ with fixed step length but invariable on both vertical axis $\boldsymbol{x_f}$ and horizontal axis $\boldsymbol{y_f}$. To evaluate the accuracy of the system at omnidirectional rotation within design requirement, we successively set scanning plane relative to CHIC fiducial frame at various tilt angles and twist angles to obtain a series of cross-sectional images, see Fig. 6-1(a). The alteration of tile angle after twist will lead to both elevation angle and direction angle change: both elevation and direction angle are equal to tilt angle at the same time. There are 5 control groups for tile angle and twist angle respectively (tilt angle at 0°, 10°, 20°, 30°, 40° and twist angle at 0°, 5°, 10°, 15°, 20°) forming 25 groups of different combination of tilt angle and twist angle in total, see Table 6-2 and Fig. 6-2.

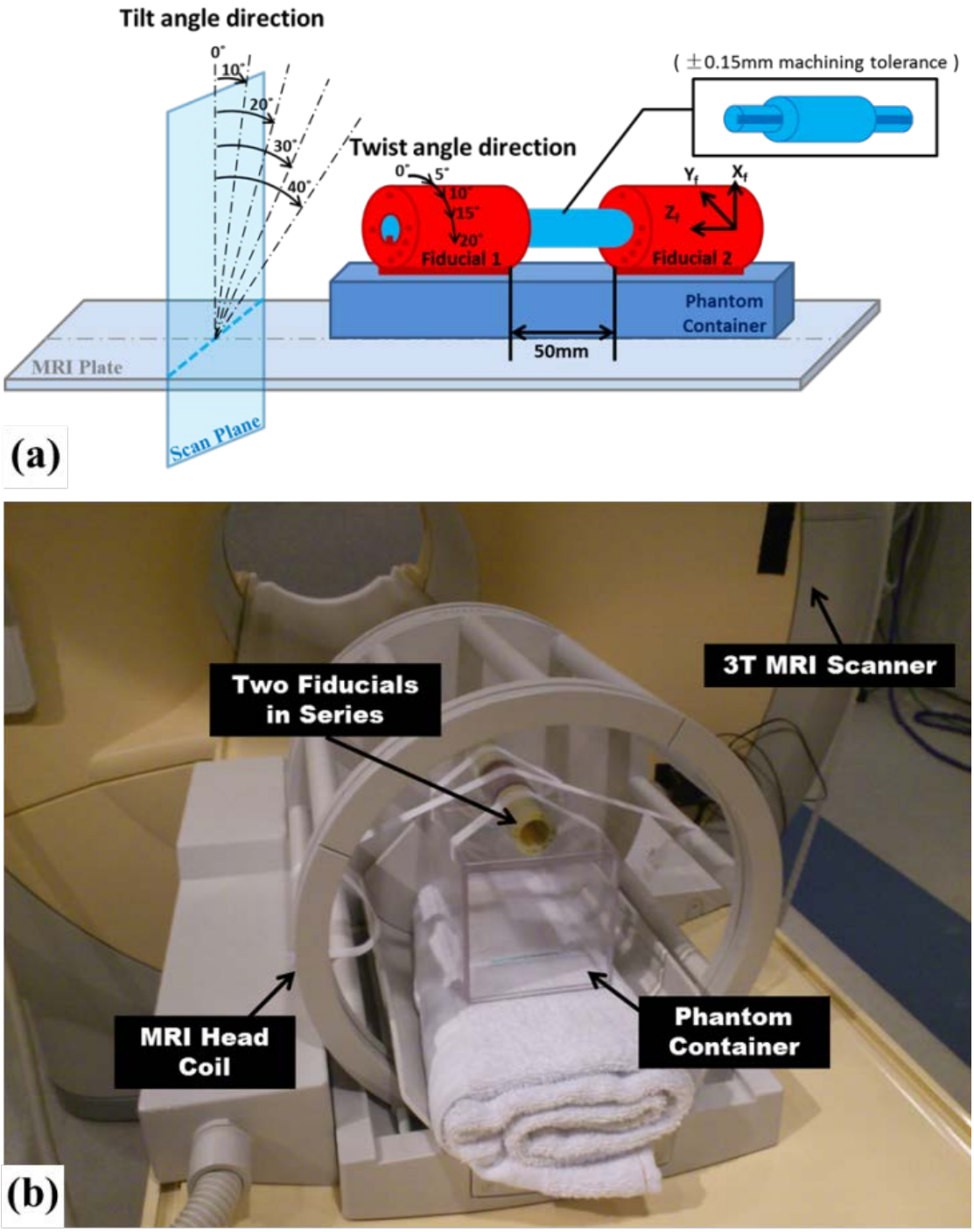

Fig. 6-1: (a) Experiment schematic. Two fiducials being connected in series by a 50mm long concentric connector are placed on a phantom container. (b) The photo of the real installment of the whole experiment setting. This experiment was extra using the MRI head coil inside 3T main coil to enhance imaging definition. And the phantom container is the place to put water bag into it for MRI scanner getting a proper imaging window of contrast ratio.

TABLE 6-1
PHILIPS 3T MRI SCANNER IMAGING PARAMETER

	FOV	TE	TR	FA	BW	Thickness	Space Between Slices	Receive Coil	Size	Pixel Spacing
T1_MYZ	--	90ms	3000ms	90°	444	2 mm	1.5mm	T/R Head	160*160	0.5*0.5

TABLE 6-2
25 GROUPS OF DIFFERENT COMBINATION OF TILT ANGLE AND TWIST ANGLE

Group #	Twist angle	Tilt angle	Description
1	0	0	Volume Scan Once
2	0	10	Volume Scan Once
3	0	20	Volume Scan Once
4	0	30	Volume Scan Once
5	0	40	Volume Scan Once
6	5	0	Volume Scan Once
7	5	10	Volume Scan Once
8	5	20	Volume Scan Once
9	5	30	Volume Scan Once
10	5	40	Volume Scan Once
11	10	0	Volume Scan Once
12	10	10	Volume Scan Once
13	10	20	Volume Scan Once
14	10	30	Volume Scan Once
15	10	40	Volume Scan Once
16	15	0	Volume Scan Once
17	15	10	Volume Scan Once
18	15	20	Volume Scan Once
19	15	30	Volume Scan Once
20	15	40	Volume Scan Once
21	20	0	Volume Scan Once
22	20	10	Volume Scan Once
23	20	20	Volume Scan Once
24	20	30	Volume Scan Once
25	20	40	Volume Scan Once

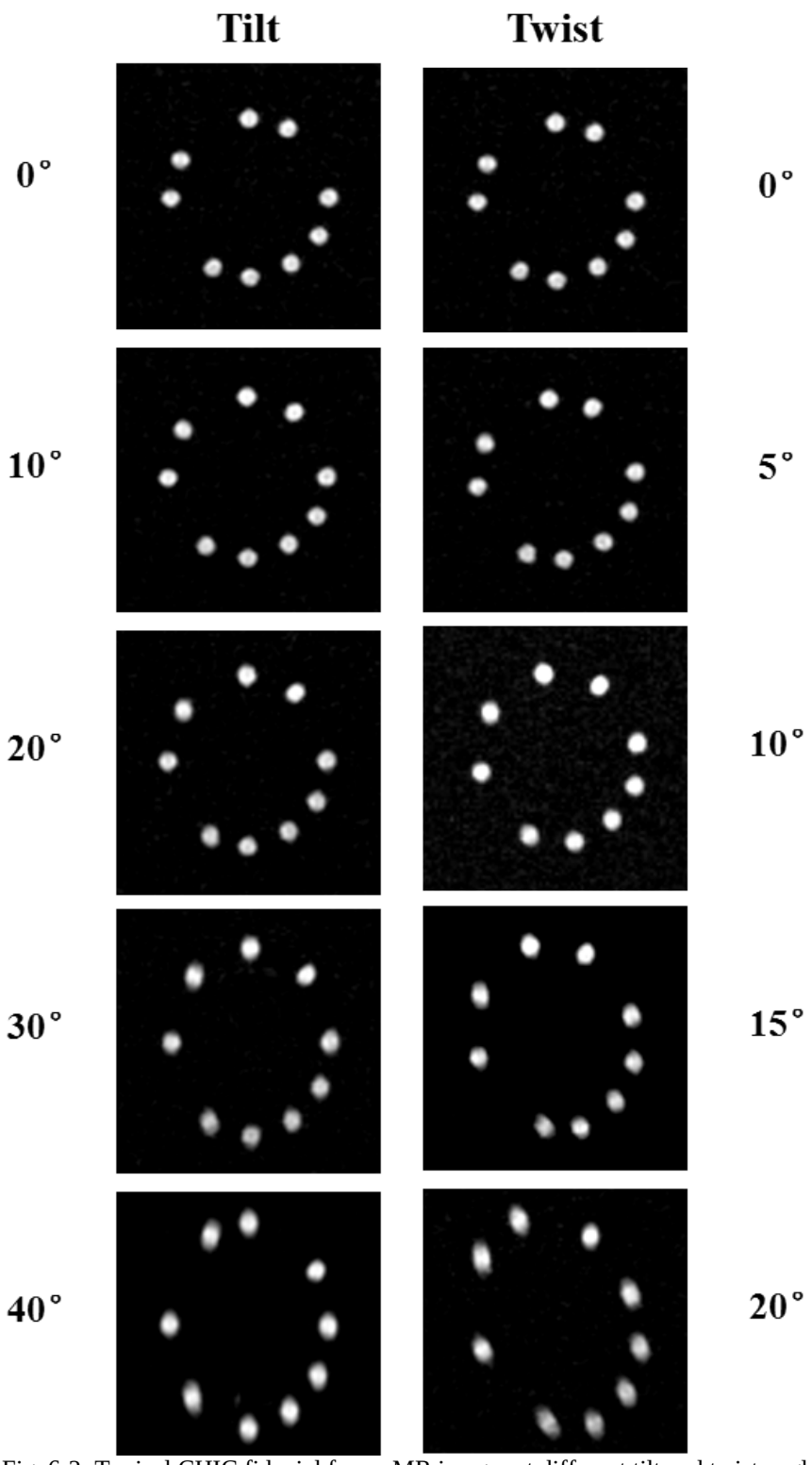

Fig. 6-2: Typical CHIC fiducial frame MR images at different tilt and twist angles

Furthermore, two CHIC fiducial frames are connected in series by a 50mm long concentric connector to make an interior contrast within a group and also test expansibility for long discrete measurement application along depth. The stepping rotation of both twist angles and tilt angles are achieved by MIR scanner itself which is more precisely than move fiducial frames manually. Fig. 6-1(b) is the photo of the real installment of the whole experiment setting. This experiment was extra using the MRI head coil to enhance imaging definition while we place the central axis of two concentric fiducial frames along the central axis of head coil. And the phantom container is the place where we put aqueous contrast medium into it for MRI scanner getting a proper imaging window of contrast ratio which is close to human tissue. By using image data provided by 25 groups, registration and tracking performance was evaluated into two aspects after: translation DOF and rotation DOF.

6.2 Accuracy Assessment

6.2.1 Evaluation of Translation

We selected 10 groups which include 5 groups of different twist angles and other 5 groups of different tilt angles, then picked 10 sequential slices from each group to evaluate the feature of translation tracking.

First, group with 0° tilt angle and 0° twist angle was selected for qualitatively analysis about translation accuracy, see Fig. 6-3. Each blue and red point in the middle diagram represents the coordinates of an image's central point getting from this selected group. And the numbers upon the line are corresponding average and standard deviation for these data. From the small wave of *x* and *y* curve, we can see the program hold a decent stability when we try to apply it to get results from many invariable input. Here you may find there is a little separation between two fiducial's *y* curve. It can be explained as double fiducial system may be placed a little bit skew initially along *y* direction. On the other side, the very smooth slop of *z* curve at top right graph shows the program can precisely measure the same gap between each slice.

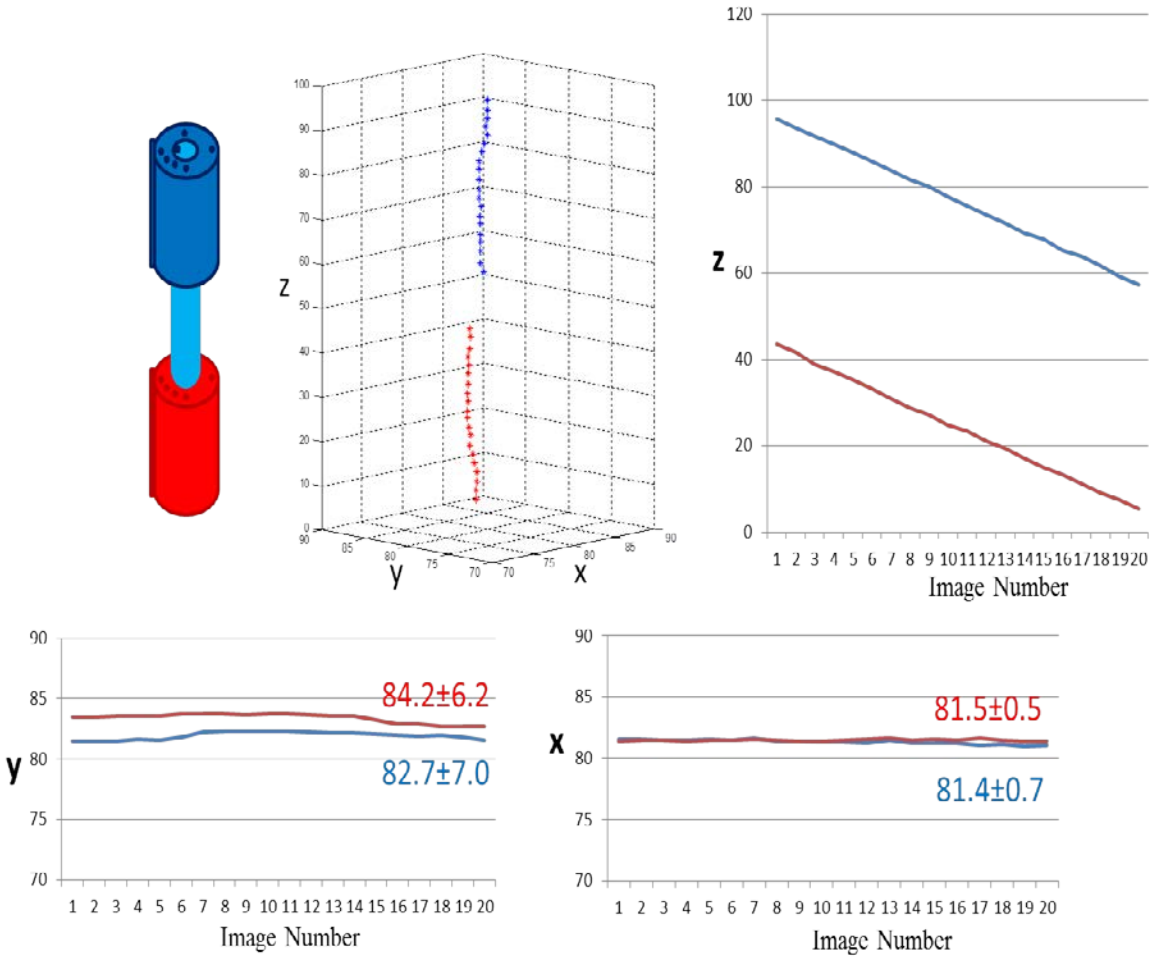

Fig. 6-3: Preliminary analysis about translation accuracy in 0° tilt angle with 0° twist angle group. The middle 3D plot shows position of all slices' central points. The three 2D plots around show the x, y and z information of all slices' central points respectively. The numbers upon the line are corresponding average and standard deviation for same color data.

Then we evaluate the translation tracking accuracy quantificationally for whole groups. We measured translation results from 100 random slices with different twist and tilt angles respectively. Since the 2D central point of each cross-sectional image should be unchangeable after registration and only cross-sectional depth variation, so we show the RMS error measurement of x_0, y_0 and z_0 together in Fig. 6-4. Then we present the detection of z_0 changing along central axis in Fig. 6-5

separately. There are 10 samples in each step which represents a set of slices scanning at same $\boldsymbol{z_0}$ position and the dash baseline marks out corresponding theoretical value.

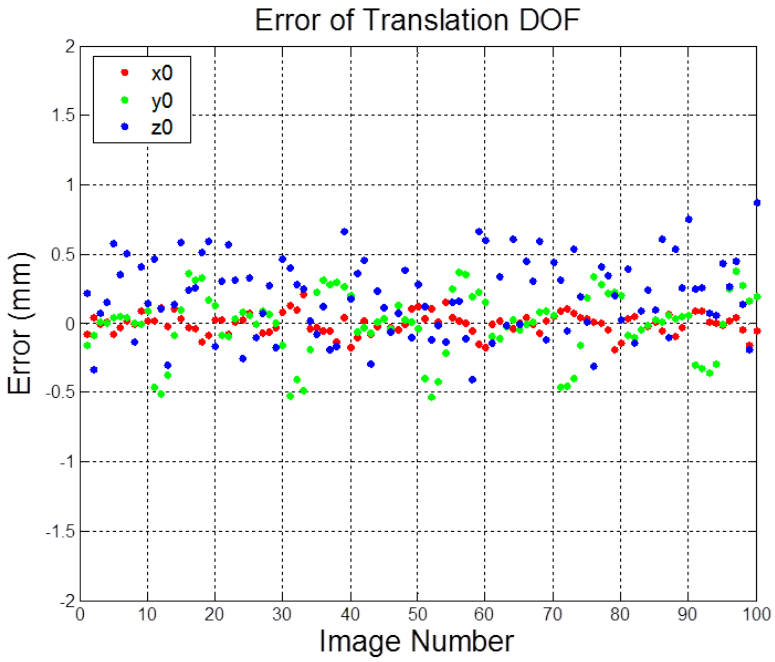

Fig. 6-4: RMS error measurement results of translation DOF from 100 slices under different twist and tilt angles. The RMS error of x_0, y_0 and z_0 is 0.074mm, 0.228mm and 0.271mm respectively.

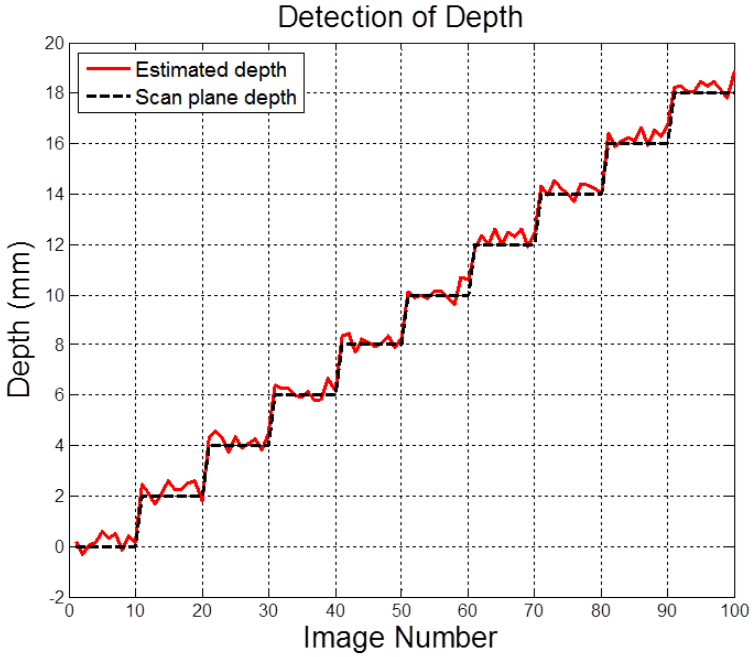

Fig. 6-5: Detection of motion in depth with 2mm regular step length along z axis with average error 0.298mm and standard deviation 0.277mm.

6.2.2 Evaluation of Rotation

Results of the rotation accuracy study are shown in three ladder-shaped plots separately. The detection of successive twist angles (φ), elevation angles (α) and direction angles (η) are list in Fig. 6-6, Fig. 6-7 and Fig. 6-8 respectively. In each case totally 50 slices are selected from five control groups of tilt or twist and the baseline of corresponding step length is also superimposed into the same plot. There are 10 samples in each step being taken from one of five groups and the dash baseline represents the corresponding ideal values they should be.

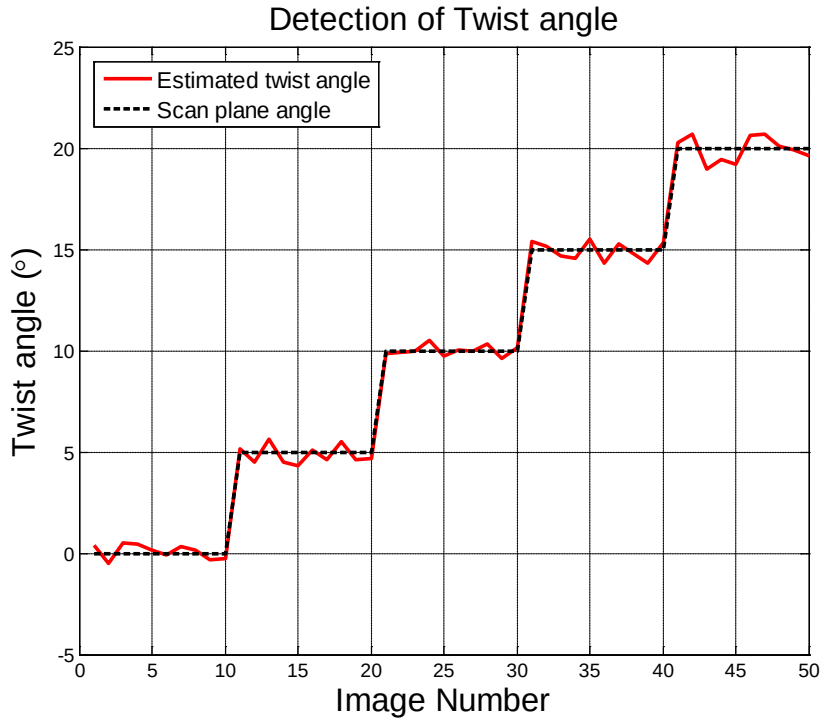

Fig. 6-6: Detection of motion in twist angle with average error 0.038mm and standard deviation 0.436mm.

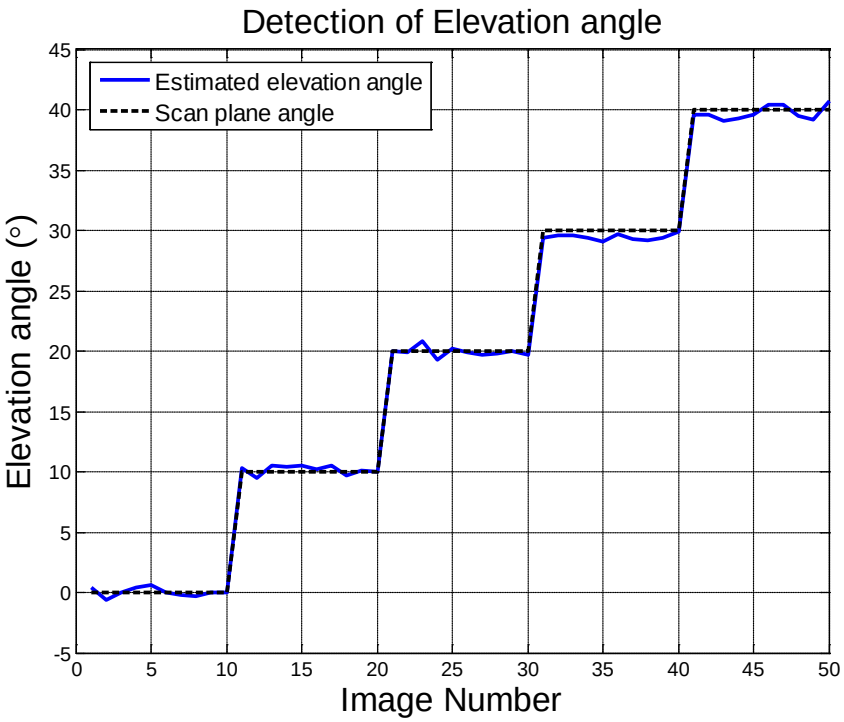

Fig. 6-7: Detection of motion in elevation angle with average error 0.146mm and standard deviation 0.458mm.

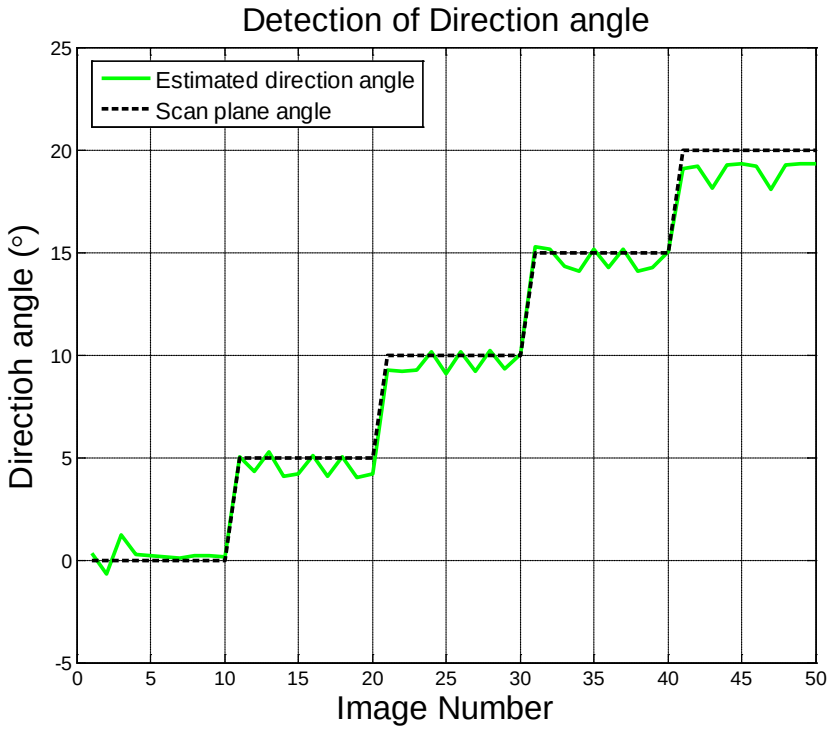

Fig. 6-8: Detection of motion in direction angle with average error 0.398mm and standard deviation 0.609mm.

6.2.3 Comprehensive Evaluation

Statistical analysis of all tracking errors is summarized in Table 6-3. We just obtain a series of relative values for x_0 and y_0 wihout its real valuse while other parameters we have fixed step length as real values. Each tracking angular error is with ±0.5° for 50 samples except standard deviation of direction angle is 0.609° due to direction angle is sensitive with any delicate error at completely vertical condition. The overall angular RMS error is 0.426° with standard deviation of 0.526° for totally 150 samples. The depth translation RMS error is 0.271mm with standard deviation of 0.277mm for totally 100 samples. But consider the dimension of fiducial frames caliber is 250mm, this defect cannot belittle virtues.

TABLE 6-3
STATISTICAL ANALYSIS OF 6-DOF TRACKING ERRORS

		Average Error	**Standard Deviation**	**RMS Error**	**Samples**
Translation	x_0	-	-	0.074mm	N = 100
	y_0	-	-	0.228mm	N = 100
	z_0 (depth)	0.198mm	0.277mm	0.271mm	N = 100
Rotation	twist	0.038°	0.436°	0.430°	N = 50
	elevation	0.146°	0.458°	0.383°	N = 50
	azimuth	0.398°	0.609°	0.470°	N = 50
	overall	**0.194°**	**0.526°**	**0.426°**	**N = 150**

Chapter 7

Passive Resonant Coil Design

To successfully perform minimally invasive surgeries by robots, fast and accurate registration and tracking for the invasive instrument is a necessary precondition. MRI offers an excellent soft tissue contrast and three-dimensional imaging capabilities, however, getting the high-definition of soft tissue images usually requires at least several seconds per slice due to MR imaging principle itself. Both gradient strength and achievable signal-to-noise ratios would be limited under fast MR imaging condition when soft tissue was the target. Under these circumstances, it is difficult to perform interventions in organs that are rapid and permanent moving, like the involvement of freehand surgery. One way to solve the problem is using resonant coil wrapping to increase change of local magnetic field gradients by arousing instant resonant magnetic field so that the contrast medium in the fiducial frame could emit more energy than general way to get higher definition imaging under fast MR imaging condition of small flip angle.

7.1 Proof of Principle

7.1.1 Single Coil LC Circuit Implementation

Single resonant coil fiducial markers were first used for localization in the 1990's, and are increasingly being used to track devices within MRI scanners [43,44]. Most systems use active method: small coil were connected into a receive channel on the scanner which record position dependent signals. Connecting the fiducials directly to the scanner allows them to be detuned during

the RF excitation. This ensures that they do not compromise images, but raises patient safety issues with the cabling, particularly for coils placed internally. In this thesis, we selected passive coil with a variable capacitor to constitute a close loop RC circuit resonating with MR scanner main coil. In light of Phillips Achieva 3T MRI scanner will working at 128MHz under normal operating conditions while the non-magnetic capacitor we can get is just at least 1 pF, the turns and length of coil is greatly limited as its inductance should be narrowed less than 1.55μH. According to coil inductance approximate formula as Fig. 7-1 shown, a 1.55μH pyknotic coil with 3mm diameter would just have about 6 turns. Although we prolonged its length to befittingly diminish inductance, it brought in another problem which will lead to non-uniform imaging along with coil we will discuss later.

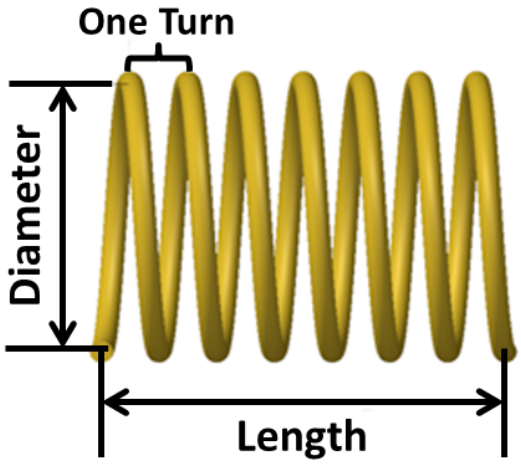

$$L = \frac{\text{Diameter}^2 \times 4\text{Turns}^2}{18\text{Diameter} + 40\text{Lenght}}$$

Fig. 7-1: Single-layer coil and corresponding inductance approximate formula

In order to be used for CHIC fiducial frame whose internal diameter of tubular mesh is 3mm, we first made a 3mm diameter sparse coil with 8 turns for interior filling of tube. On other side, we also made a 6mm diameter sparse coil with 3 turns for exterior wrapping since at least 1.5mm tube wall for each tubular mesh is just enough for its mechanical strength after 3D printer manufacture, see Fig. 7-2. The chosen variable capacitor supports capacitance changing within 1~6pF continuously.

Both them contained MRI high contrast registration fluid inside of the coil and were well-tuned with 128MHz resonant frequency.

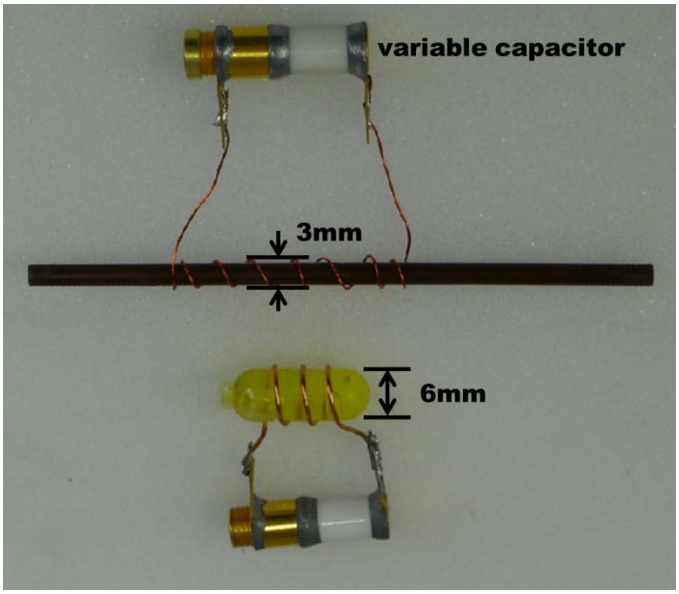

Fig. 7-2: Single Coil LC Circuit with 6mm coil diameter (bottom) and 3mm coil diameter (top)

7.1.2 MRI Results

Tracking of passive fiducials requires careful selection of a pulse sequence to ensure marker contrast. Generally, dual-flip angle gradient echo sequences have been used with a low flip angle for fiducial imaging and a larger excitation for anatomical imaging [45]. All resonant coil images in this thesis were acquired with a fast low angle shot (FLASH) pulse sequence, see Table 7-1 (TE = 4.8ms, TR = 9.2ms, slice thickness 2mm, matrix 2562, pixel space 0.5 x 0.5, pixel size 1.1mm, flip angle 2°, bandwidth 390 Hz/pixel). The layout of resonant coils and control group in the MR scanner are shown in Fig. 7-3 which their axis slice located at the isocentre of main coil.

TABLE 7-1
FAST LOW ANGLE SHOT (FLASH) PULSE SEQUENCE

	FOV	TE	TR	FA	BW	Thickness	Space Between Slices	Size	Pixel Spacing
T1_FAST	--	4.8ms	9.2ms	2º	390	2 mm	1.5mm	80*80	0.5*0.5

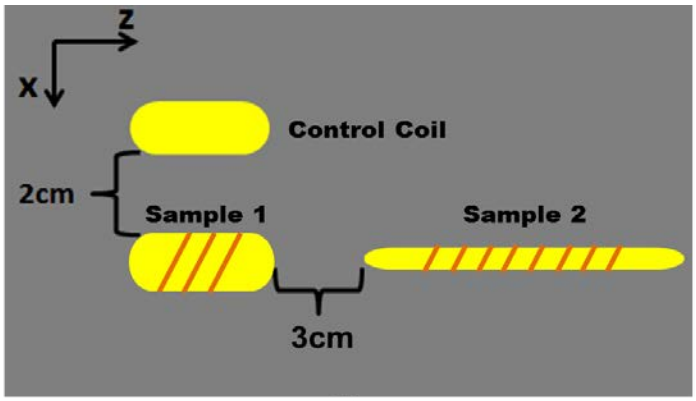

(a)

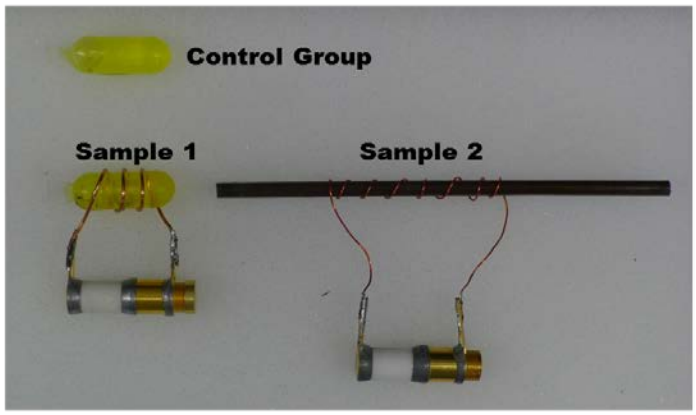

(b)

Fig. 7-3: (a) Diagrammatic drawing for single coil layout in MRI experiment. The top one is control group with no resonant coil, and the bottom left and bottom left are exterior coil and interior coil respectively. (b) Photo of real products in MR scanner.

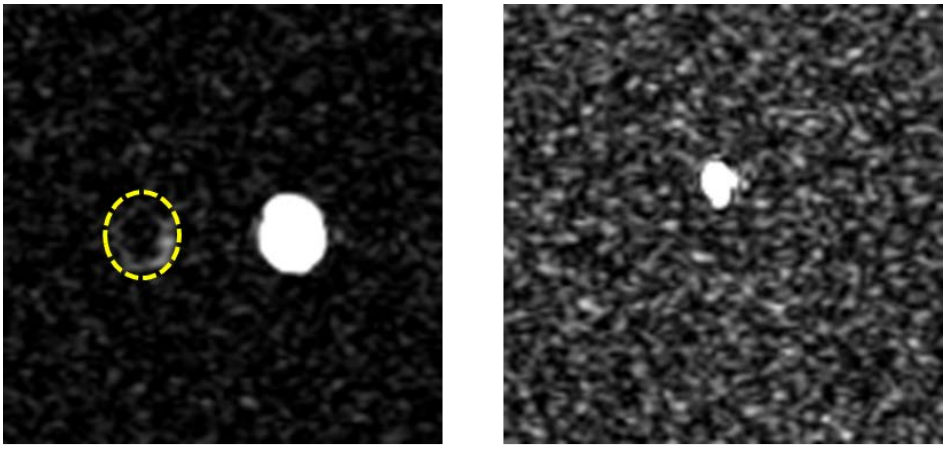

(a) (b)

Fig. 7-4: (a) MR image of control group (yellow circle) and exterior coil. (b) MR image of exterior coil. Their MRI results show the traditional contrast medium is hardly recognized under fast MR imaging, and the one with lager diameter coil wrapping is brighter and has higher SNR than the small diameter one.

From the MRI results in Fig. 7-4 we can know soft tissue or MRI high contrast registration fluid is hardly to see under fast low angle shot (FLASH) pulse sequence using in real time imaging. While both coil wrapped samples appear brightly in the same fast imaging condition. By comparing (a) and (b), it notices us the little imaging spot formed by small coil will drop off the SNR of MR image which adds more disturbance to the image analysis step even though the small diameter coil could be made to a longer size than lager diameter coil since it allows relative more turns under same inductance requirement. So it's important to keep the balance between coil diameter and turns during design to guarantee the SNR of MR images.

Another point in the single coil experiment is several sub-bright artifacts appearing around real spot when we tuned the coil circuit's resonant frequency very close to MR scanner main coil's imaging frequency for getting a brighter imaging spot, see Fig. 7-5. What we figured before is a perfect match resonant frequency would generate the best imaging results, but this unexpected phenomenon told us that the resonant frequency of coil and main coil are not the closer, the better. The high consistent matching of resonant frequency will stimulate artifacts and fake shadow like ringing effect although it does make tacking spots brighter.

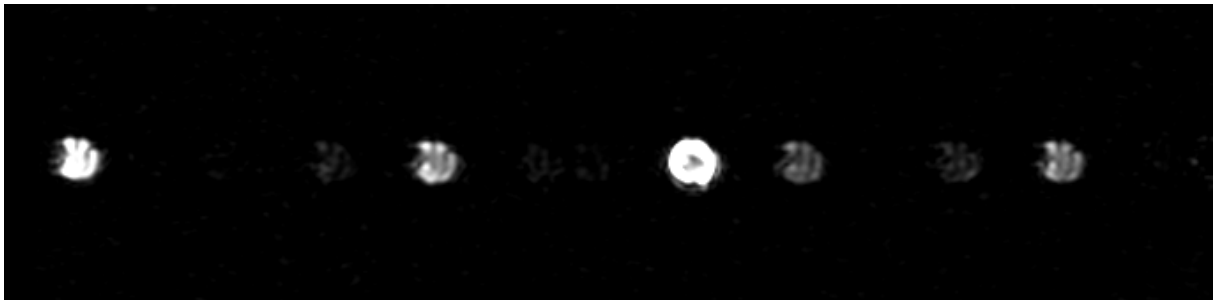

Fig. 7-5: An array of sub-bright artifacts appearing around real spot

7.2 Analysis for Alternative Designs

7.2.1 Double Layers Coil with Reversely Wrapping Proposal

The straightforward thought we proposed at earlier coil design stage is to combines CHIC fiducial frame with coil directly by clockwise warping coil over its cylindrical external surface and

then anticlockwise wrapping back from its internal surface in order to counteract most of magnetic flux so that it would minim the inductance of whole system as Fig. 7-6 shown. But it turned out to be just an idle assumption due to its huge inductance calculating from aforementioned inductance approximate formula. It's impossible to buy a capacitor with such small capacitance to resonate with it around 128MHz.

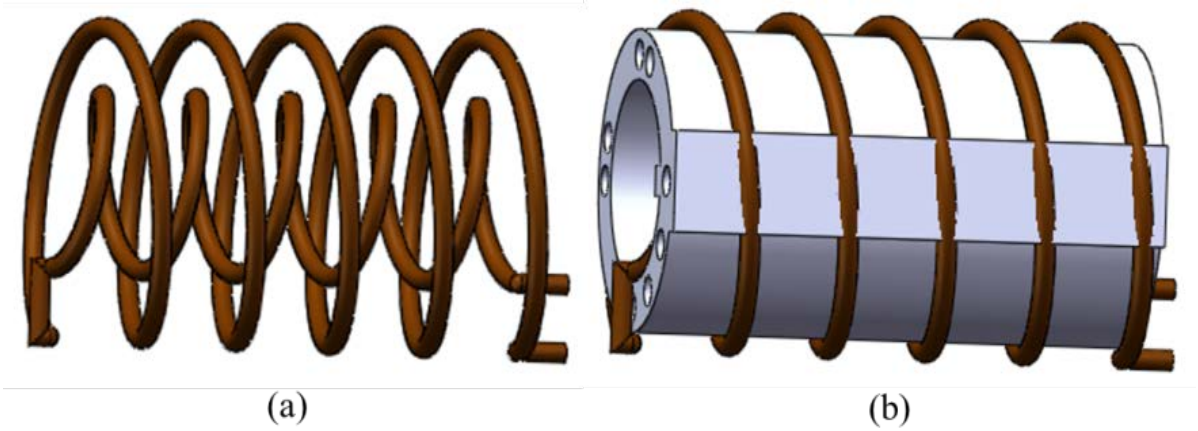

Fig. 7-6: (a) Double layers coil with clockwise exterior warping and anticlockwise interior wrapping. (b) CAD view of CHIC fiducial frame with reversely wrapping double layers coil

7.2.2 Interior Sub-coils Prototype

After impractical plan A, we changed our thought back to small single coil and decided to break the big coil in plan A into a cluster of sub-coils inside the tubular mesh and connect them in parallel, see Fig. 7-7. This design was implemented a complex multi-coil cluster with the uniform distribution of same resonant frequency within the whole system which means every sub-coils should be made almost identically. The formula of identical inductance in parallel, $L = \frac{L_i}{n}$, suggests if we make nine same sub-coils inside CHIC fiducial frame, the inductance of each sub-coil will allow nine times larger than the requested system inductance. In other words, the sub-coils connecting in parallel could be made longer and denser than any single coil. However, two problems lie behind this design that may lead to poor imaging quality: 1) small diameter of coil would lower the SNR of MR image;

2) the space inside tube where should be fully filled by contrast medium will be partly occupied by interior sub-coils result in forming incomplete spots.

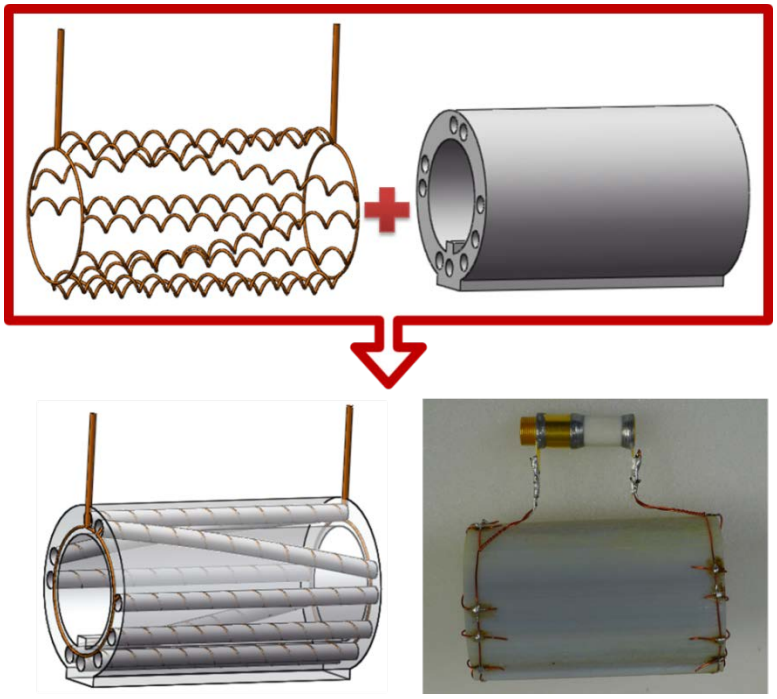

Fig. 7-7: CAD drawing and implementation of interior sub-coils CHIC fiducial frame

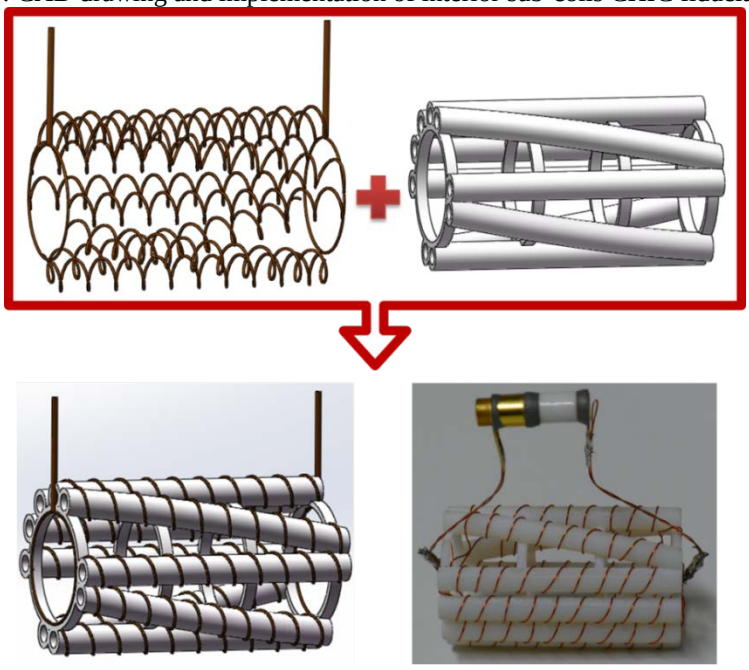

Fig. 7-8: CAD drawing and implementation of exterior sub-coils CHIC fiducial frame

7.2.3 Exterior Sub-cols Prototype

In this design, we manufactured a skeleton for CHIC fiducial frame so that we can wrap a relative large diameter coil outside the tubular mesh without worry about it occupied the interior room of tubes forming crippled spots, see Fig. 7-8. This design has a stability problem: the shape of exterior coil is too ductile to be easily deformed unexpectedly even when it was slightly touched.

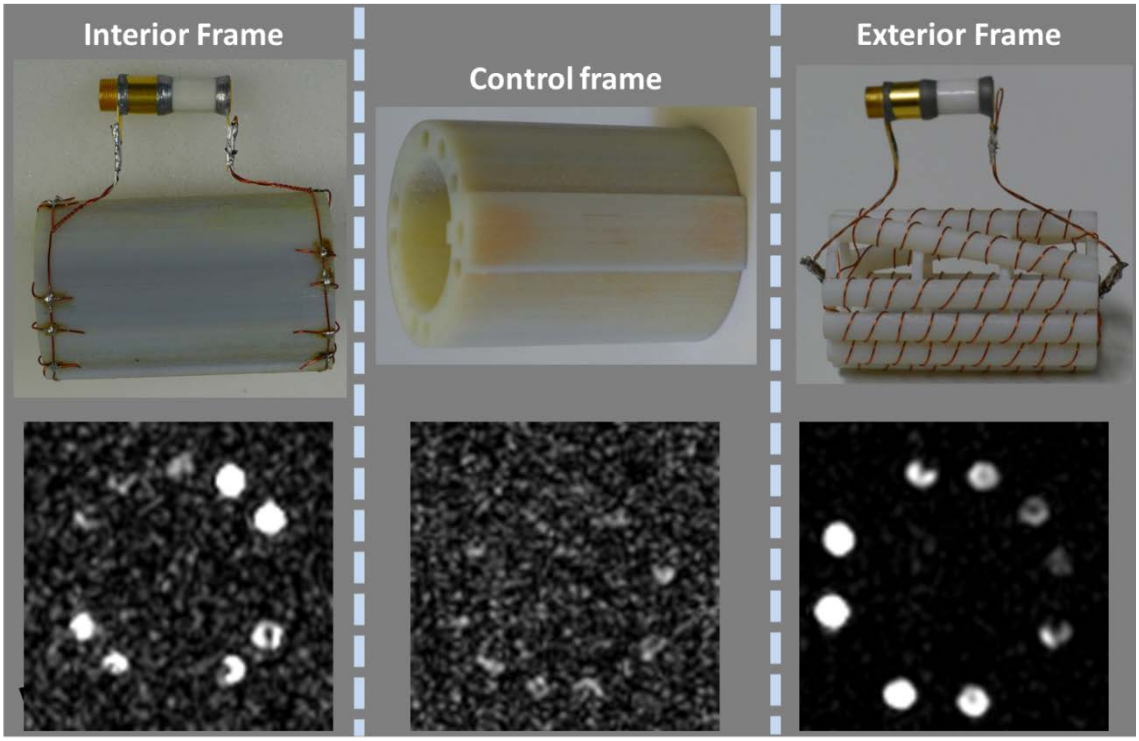

Fig. 7-9: Fast MRI results of interior sub-coils CHIC fiducial frame (left), Non-coil CHIC fiducial frame control group (middle), and Exterior sub-cols CHIC fiducial frame (right)

In order to compare imaging quality between interior frame and exterior frame, we placed them with a non-coil-wrapped CHIC fiducial together to imaging under fast low angle shot (FLASH) pulse sequence by Phillips Achieva 3T MRI scanner, see Fig. 7-9. These results first proved that well-designed resonant sub-coils can be made very long insider or outside the fiducial frame tube for fast MRI imaging. And it also show that exterior is better than interior since it not only doesn't occupy the space of interior tube where is fully filled by gelatin but also imaging a better SNR slice than interior

one. The exterior results also showed a surprising clear images and tiny artifacts in fast imaging which we will give some quantitative analyses later.

But new problems popped up: From the lateral view of both two sub-coil CHIC fiducial frames, see Fig. 7-10, imaging results revealed both coil wrappings were too sparse to forming an inhomogeneous distribution along tubular mesh. And it also demonstrated the tubes far from variable capacitor will present a relative dim imaging than the one close to variable capacitor. So an eccentric capacitor structure and sparse coil turns are the two main reasons why we saw different brightness of each tracking spot in the same cross-sectional image in Fig. 7-9.

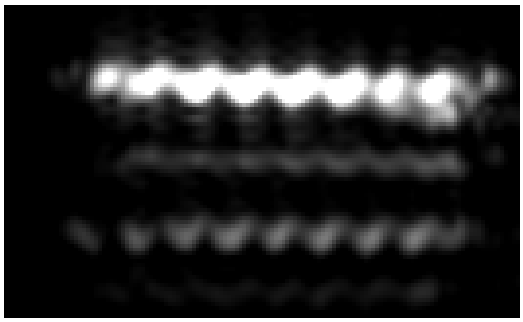

Fig. 7-10: Lateral view of sub-coil CHIC fiducial frame with inhomogeneous distribution along its tubular mesh.

7.3 Final Improved Design

7.3.1 Mechanic Structure

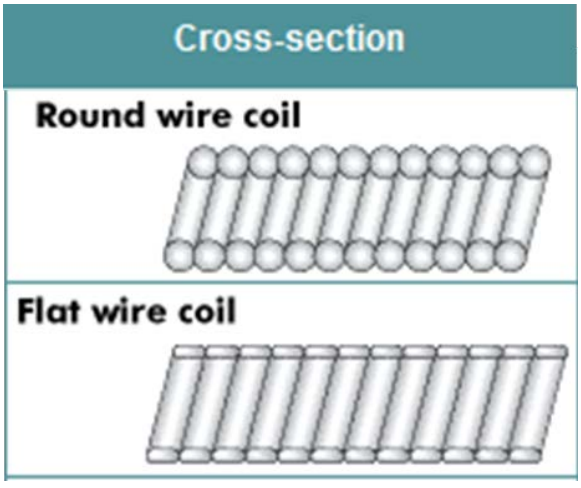

Fig. 7-11: Two Different cross-sections of coil materials

Now that primary MRI results confirmed exterior sub-coils CHIC fiducial frame has preponderant features in fast MR imaging, we managed to solve its three defects: 1) loosing stereo structure; 2) sparse turns; 3) asymmetrical imaging distribution. We abandoned traditional round wire to wrap the coil but turn to adopt flat wire to cover as much surface as coil can under same turns, see Fig. 7-11. Then a 1/8 inch wide flat cooper foil came into our view which has acrylic adhesive on one of its surface so that we can firmly adhere it onto CHIC fiducial skeleton to avoid unexpected coil deform. Besides, the variable capacitor will be connected in the center of CHIC fiducial frame in order to keep all the tubes have relative same distance to it eliminating asymmetric, see Fig. 7-12. The improved CHIC fiducial skeleton will bond tubular mesh only at each end instead of internal bracing in order to allow a dense coil wrapping covering tubes.

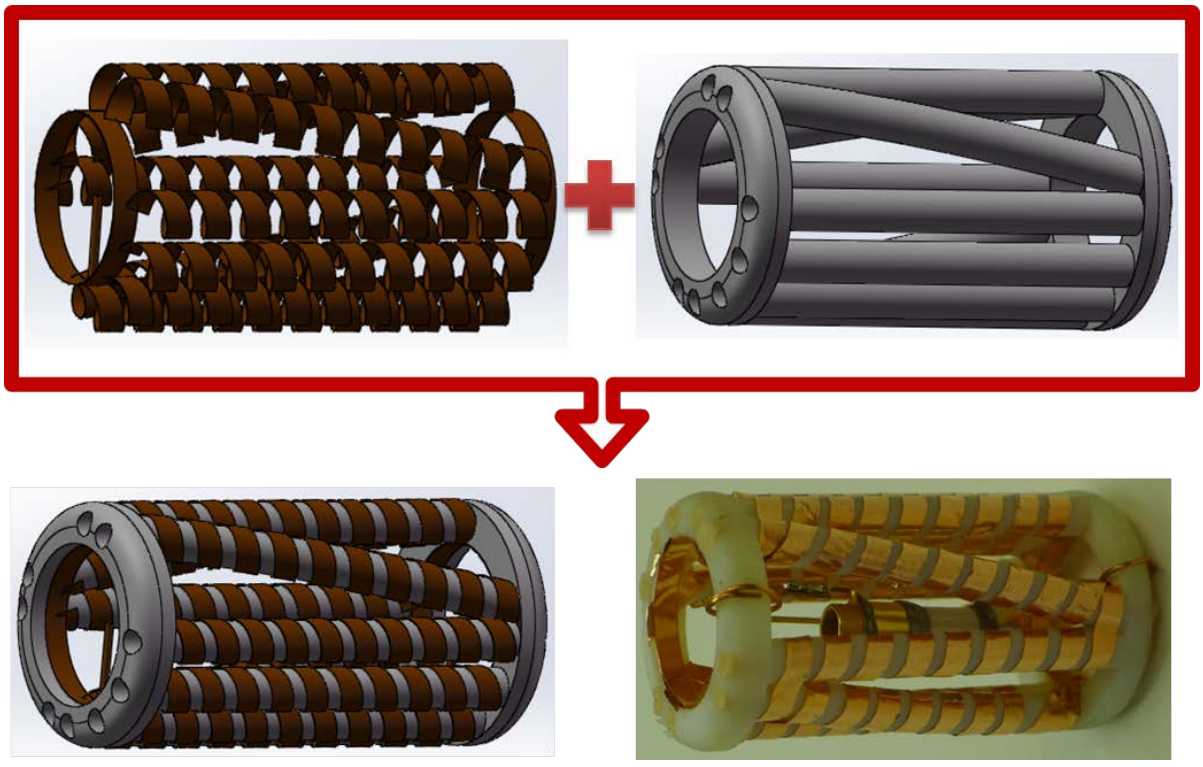

Fig. 7-12: CAD drawing and implementation of improved exterior sub-coils CHIC fiducial frame

7.3.2 MRI Results

The Fig. 7-13 shows the imaging results of exterior sub-coils CHIC fiducial frame under fast low angle shot (FLASH) pulse sequence. From the front view, it verifies sub-coils CHIC fiducial frame can provide plump tracking spots for all tubes with high imaging SNR by placing variable capacitor inside the center of CHIC fiducial frame. On the other hand, the lateral view demonstrates the flat copper foil wrapping make the imaging distribute along tubular mesh more continuously and uniformly than previous one. Also, the adhesive flat copper attached on tubes surface firmly preventing potential deformation caused by outside force.

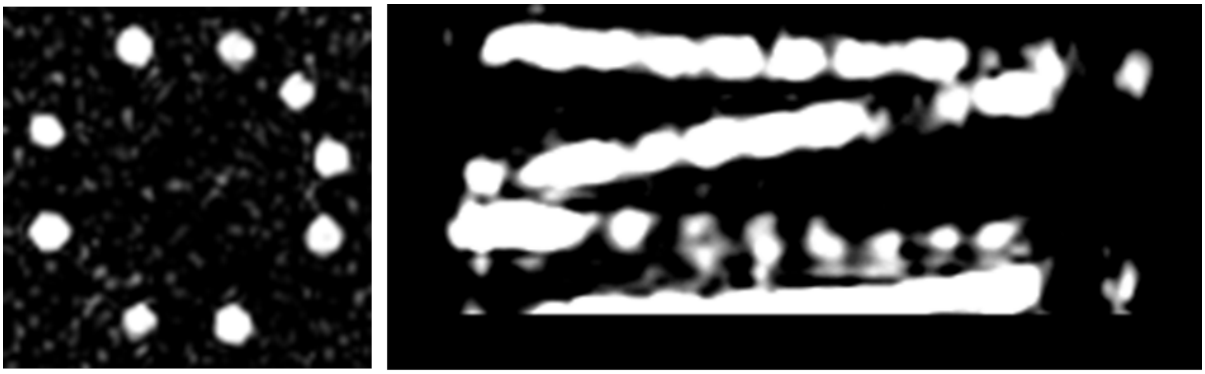

Fig. 7-13: Improved exterior sub-coils CHIC fiducial frame imaging under fast low angle shot (FLASH) pulse sequence. (a) Front view, (b) Lateral view.

The soft tissue could generates dim imaging under fast imaging condition, however, that images can hardly provide the enough information for tracking or anatomical identification due to the lower contrast ratio and poor SNR. To quantitative analysis the imaging difference of the improved exterior sub-coils CHIC fiducial frame with respect to pure contrast medium under fast imaging condition, we place it upon a contrast medium bag which is containing normal saline using in the traditional soft tissue MR imaging, see Fig. 7-14. We got their imaging result in Fig. 7-15(a) and then drawn a red ling which was cross through two tracking spots (one was close to spot center and another one was close to spot border) and contrast medium bag in order to get the plot of pixel intensity distribution along the red line, see Fig. 7-15(b). The peak values of two tracking spots and contrast medium bag demonstrated the imaging intensity of improved exterior sub-coils CHIC

fiducial frame is about 2~4 times better than pure soft tissue that means it will give more detailed information about interested target under fast MR imaging during real-time MIS.

Fig. 7-14: Quantitative analysis experiment for imaging intensity difference between improved exterior sub-coils CHIC fiducial frame and contrast medium bag

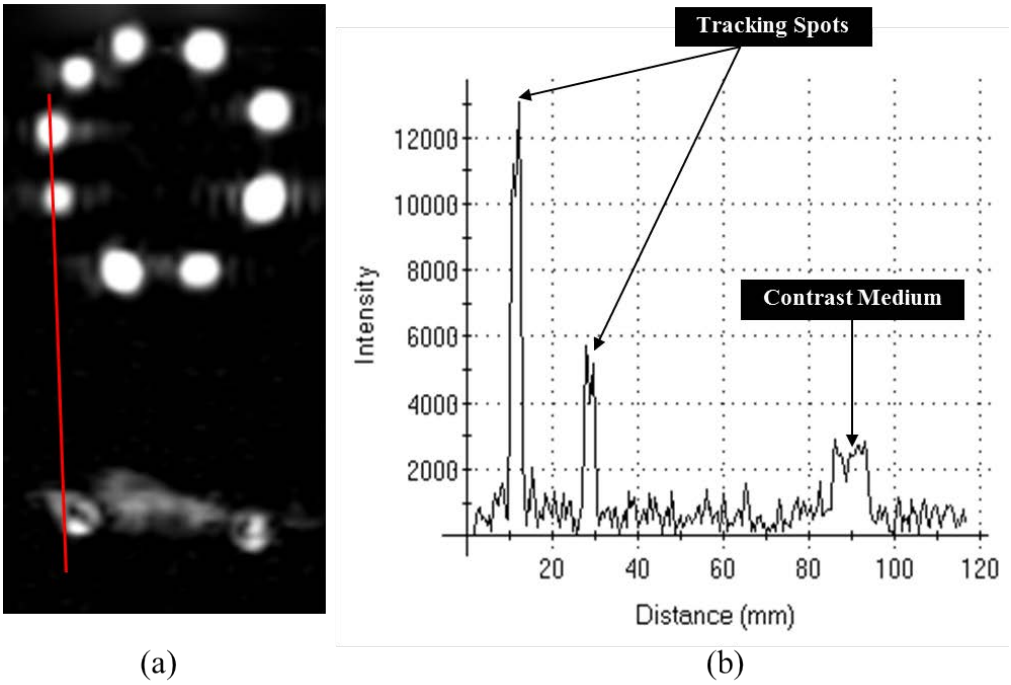

Fig. 7-15: Imaging intensity difference between improved exterior sub-coils CHIC fiducial frame and contrast medium bag. (a) Sampling trajectory along red line, (b) Pixel intensity distribution along red line

Chapter 8

Conclusion

MR imaging and navigation research is a developing area for surgical robotics. The hardware development for MRI-guided robotics has been set largely with a solid foundation while the MRI-guidance is progressing relative slowly. However, more importantly, real-time robot localization, registration and tracking are the key parts to close the image guidance and feedback control loop. Image processing and computer vision would play major role for MRI-guided robotic systems. Right now, the method developed in this thesis got some good outcomes in the image guidance integration and feedback providing for surgical robot under MRI environment.

8.1 Summary of Work and Contributions

8.1.1 Summary

In this thesis, we developed a fast registration and tracking system for real-time closed-loop control of robot in MIS under MRI guidance. Its novel 6-DOF registration and tracking fiducial frame and corresponding algorithm can be used to provide full 6-DOF tracking information for robotic surgery under MRI guidance. The commonly used modular structure makes this registration and tracking system completely feasible to support remote control and multi-platform operating. And we achieved an approach to get real-time imaging and track rapid motion by wrapping an elaborate passive resonation coil outside of fiducial. This method will allow us to get high definition fiducial

images under fast MRI imaging. It breaks the limitation that traditional MRI-guided surgeries are only feasible for slow pace of robotic movement due to relative low imaging speed of soft tissue. The developed mechanism in this thesis is for MRI-guided surgical robot, however, the modular hardware and software support a variety of image-guided MIS. As long as the fiducial frame of registration and tracking system is electromagnetic compatible, it is also suitable for ultrasound or CT guidance.

8.1.2 Impact and Contribution

- **Designing an exclusive CHIC registration fiducial frame**

The elaborate stereotactic structure of compact fiducial frame allows image analysis program to reconstruct each 3D pose from one unique 2D spots pattern MR image. The unique and ample helical imaging pattern inside CHIC frame allows detection of a 6-DOF pose by only using one slice image from its compact cylindrical structure. The interior tubular mesh is filled with high MRI contrast gelatin or gadolinium fluid providing nine tracking spots in the cross-sectional image to guarantee detection accuracy and stability of the image analysis algorithm.

- **Developing an analysis approach to optimize image processing and accuracy**

2D Gaussian distribution model was brought in tracking centroid measurement. It effectively avoids errors caused by dark shadow in certain tracking spots forming from some small bubbles inside of contrast medium. The high efficiency and accuracy of MRI image processing algorithm also guarantee the quality of real-time registration and tracking in MIS.

- **Development of independent and modular communication framework**

The software framework integrated a DICOM server, a portable registration and tracking algorithm with OpenIGTLink network communication protocol, as well as user interface for the physician to coordinate the procedure and control the robot. Besides, it’s a standalone system that achieves registration and tracking without any additional instrument or supports just like MRI experiment setup demonstrated in Chapter 6. The data flows among modules are well-designed to undertake different types of real-time DICOM image flow into two proper ways: unidirectional &

high-throughput direct connection and bidirectional & remote network link. Moreover, the performance of registration and tracking system was rapid enough for real-time MRI-guided MIS.

- **Accuracy evaluation of fiducial frame design and simulation.**

The error results presented outstanding tracking accuracy during detecting full 6-DOF stereo pose by just a single 2D cross-sectional image. Meanwhile, these results also attested that it's doable to utilize single-slice based fiducial detection methods to assist robot motion synchronize with real-time registration and tracking. Each tracking angular error was with ±0.5° for 50 samples except standard deviation of direction angle was 0.609°. The overall angular RMS error was 0.426° with standard deviation of 0.526° for total 150 samples. The depth translation RMS error was 0.271mm with standard deviation of 0.277mm for total 100 samples. But consider the dimension of fiducial frames caliber was 250mm, this defect cannot belittle virtues. However, we have to notice that this accuracy depends upon the pixel size which in our experiment is $\frac{\text{field of viem}}{\text{image dimension}} = 0.5\text{mm}$. This demonstrated the system is completely able to track MRI-guided robot executing real-time surgery in a minimally invasive and accurate manner.

- **Developing and optimizing passive resonant coils for fiducial frame**

The exterior surface of fiducial frame was wrapped with passive tracking coil to reduce MR imaging time by resonating with MR scanner main coil so that it implemented tracking rapid movement and can be extended to freehand involved surgery. Although bringing non-ferromagnetic tracking coil into system may lead to image distortion during MR imaging, we minimized its MRI distortion by applying symmetrical distribution of each sub-coil and choosing an appropriate deviation of coil resonant frequency. The low-angle shot (FLASH) pulse sequence MR fast imaging results in Chapter 7 showed this elaborate non-ferromagnetic tracking coil dramatically shrunk imaging time while generating almost zero image distortion. The high MRI-compatibility of resonant coil generates very tiny artifact or disturbance in MRI images.

8.2 Future Work

8.2.1 User Interface Enrichment

The immediate future work to be done would be developing a better user interface for registration and tracking system to deal with complex conditions. It will allow physician to manipulate automatic movement of robot along pre-marked path coordinating with real time tracking results. The concomitant user interface would display both instrument pose and patient's anatomic image at same visual field so that surgeon could check the relative position of instrument and target. In addition, we will also develop a new mode in user interface for robot calibration. The mode would load and display requested transformation matrix pose and tracked transformation matrix pose continuously at the same time and same visual view in order to reveal the movement error between input and output of robot movement. All these new functions will improve the multi-ability of registration and tracking system to avoid some common tracking faults such as single visual view misconception, soft tissue deformation under force or lack of relative position information [47]. On the other hand, the tracking algorithm needs improvement to raise its accuracy and robustness. And the DICOM sever part also needs some promotion that its basic image data base will be upgraded from Matlab storage library function into high efficiency data structure by calling certain C++ mix-programmed dynamic link library (DLL) files. In the future application, the input and output interfaces: DICOM sever and correction feedback modules, are hoping to be implanted and run steadily in the MRI console computer under different operation system.

8.2.2 Fiducial Frame Size Diversification

Various dimensions of CHIC fiducial frame will be adopted in other MRI-guided surgeries like shown in Fig. 4-11 in Chapter 4 whose image definition is also different so that it needs us to do further work to evaluate the change rule of its accuracy under manifold size and imaging definition before launching it into other applications whose fiducial size are quite different. Another possible question is how much motion can be allowed for reconstruction to be robust enough. If the target moves above this threshold, then there will be a need for a completely new fiducial frame with lager

size. From the sample data, the upper limit on the target motion, above what value they needs to be a reacquisition would be identified. We are still working on testing different fiducial frames with typical size in medical applications. The fiducial frames will be made into a set of typical size and labeled corresponding errors so that we can just by installing anther ready-made and calibrated fiducial frame into robot or instrument when we change to a new type of surgery. It will widely extend the application area of this thesis work to other MRI-guided surgeries.

8.2.3 Tracking Algorithm Platform Transplantation

Furthermore, the registration and tracking system presented in this thesis open up the doors to be application to many other image-guided technologies and their combination for medical robot, such as X-ray computed tomography (XCT), single photon emission computed tomography (SPECT), and positron emission tomography (PET). There is no major technical hurdle for extending our registration and tracking system into other image-guided robotic surgery. In light of their imaging principle are very similar, some mutually compatible contrast agents are adopts in many hybrid image-guided clinic application. The iodine-containing contrast medium is one of commonly used contrast medium for CT, PET and SPECT [48-50]. We could fill the corresponding contrast medium inside the tubular mesh of fiducial frame to easily transplant it working under other image-guided environment.

Bibliography

[1] Y. Sekiguchi, Y. Kobayashi, H. Watanabe, Y. Tomono, T. Noguchi, Y. Takahashi, K. Toyoda, M. Uemura, S. Ieiri, and T. Ohdaira, "In vivo experiments of a surgical robot with vision field control for single port endoscopic surgery," *Engineering in Medicine and Biology Society, EMBC, 2011 Annual International Conference of the IEEE,* pp. 7045–7048, 2011.

[2] A. Gholipour, M. Polak, A. van der Kouwe, E. Nevo, and S. K. Warfield, "Motion-robust MRI through real-time motion tracking and retrospective super-resolution volume reconstruction," *Engineering in Medicine and Biology Society, EMBC, 2011 Annual International Conference of the IEEE,* pp. 5722–5725, 2011.

[3] M. Beck, T. Mittlmeier, P. Gierer, C. Harms, and G. Gradl, "Benefit and accuracy of intraoperative 3d-imaging after pedicle screw placement: a prospective study in stabilizing thoracolumbar fractures," *European Spine Journal*, vol. 18, no. 10, pp. 1469–1477, 2009.

[4] C. R. Grindle, J. M. Curry, M. D. Kang, J. J. Evans, and M. R. Rosen, "Preoperative magnetic resonance imaging protocol for endoscopic cranial base image-guided surgery," *American journal of otolaryngology*, vol. 32, no. 6, pp. 451–454, 2011.

[5] P.A. Starr, C. W. Christine, P.V. Theodosopoulos, N. Lindsey, D. Byrd, A. Mosley, and W. J. Marks, "Implantation of deep brain stimulators into the subthalamic nucleus: technical approach and magnetic resonance imaging-verified lead locations," *J Neurosurg*, vol. 97, pp. 370–387, Aug 2002.

[6] C. Meeuwis, J. Veltman, H. Hall, R. Mus, C. Boetes, J. Barentsz, and R. Mann, "MR-guided breast biopsy compared with vacuum-assisted biopsy," *European radiology*, vol. 22, pp. 341-349, 2012.

[7] Su H, Zervas M, Cole GA, Furlong C, Fischer GS, "Real-time MRI-Guided Needle Placement Robot with Integrated Fiber Optic Force Sensing," International Conference on Robotics and Automation, Shanghai, China, pp. 1583-1588, 2011.

[8] R.G. Watkins IV, A. Gupta, R.G. Watkins III, "Cost-effectiveness of image-guided spine surgery," *Open Orthop J*, vol. 4, pp. 228- 233, 2010.

[9] V. Horsley and R. H. Clarke, "The structure and functions of the cerebellum examined by a new method," *Brain*, vol. 31, no. 1, pp. 45-124, 1908.

[10] K. Cleary and T. M. Peters, "Image-guided interventions: Technology review and clinical applications," *Annual Review of Biomedical Engineering*, vol. 12, no. 1, pp. 119-142, 2010.

[11] T. Guo, K. W. Finnis, A. G. Parrent, and T. M. Peters, "Visualization and navigation system development and application for stereotactic deep-brain neurosurgeries," *Computer Aided Surgery*, vol. 11, no. 5, pp. 231-239, 2006.

[12] G. Cole, J. Pilitsis, and G. S. Fischer, "Design of a robotic system for MRI-guided deep brain stimulation electrode placement," *Proc. IEEE Int. Conf. Robotics and Automation ICRA '09*, pp. 4450-4456, 2009.

[13] G. Cole, K. Harrington, H. Su, A. Camilo, J. Pilitsis, and G. Fischer, "Closed-Loop Actuated Surgical System Utilizing Real-Time In-Situ MRI Guidance," *12th International Symposium on Experimental Robotics - ISER 2010, New Delhi and Agra, India*, Dec 2010.

[14] G. S. Fischer, I. Iordachita, C. Csoma, J. Tokuda, P. W. Mewes, C. M. Tempany, N. Hata, and G. Fichtinger, "Pneumatically operated MRI-compatible needle placement robot for prostate interventions," *Proc. IEEE Int. Conf. Robotics and Automation ICRA 2008*, pp. 2489-2495, 2008.

[15] M. R. van den Bosch, M. R. Moman, M. van Vulpen, J. J. Battermann, E. Duiveman, L. J. van Schelven, H. de Leeuw, J. J. W. Lagendijk, and M. A. Moerland, "MRI-guided robotic system for transperineal prostate interventions: proof of principle," *Physics in Medicine and Biology*, vol. 55, no. 5, pp. N133-40, 2010.

[16] B. Yang, U. Tan, R. Gullapalli, A. McMillan, and J. Desai, "Design and implementation of a pneumatically-actuated robot for breast biopsy under continuous MRI," *IEEE ICRA 2011 International Conference on Robotics and Automation, Shanghai, China*, 2011.

[17] N. Tsekos, A. Khanicheh, E. Christoforou, and C. Mavroidis, "Magnetic resonance compatible robotic and mechatronics systems for image-guided interventions and rehabilitation: a review study," *Annu Rev Biomed Eng*, vol. 9, pp. 351-387, 2007.

[18] A. Melzer, B. Gutmann, T. Remmele, R.Wolf, A. Lukoscheck, M. Bock, H. Bardenheuer, and H. Fischer, "Innomotion for percutaneous image-guided interventions," *Engineering in Medicine and Biology Magazine, IEEE*, vol. 27, no. 3, pp. 66-73, May 2008.

[19] G. R. Sutherland, I. Latour, A. D. Greer, T. Fielding, G. Feil, and P. Newhook, "An image-guided magnetic resonance-compatible surgical robot," *Neurosurgery*, vol. 62, no. 2, pp. 286-292; discussion 292-293, Feb 2008.

[20] M. Rea, D. Mcrobbie, H. Elhawary, Z. T. H. Tse, M. Lamperth, and I. Young, "Sub-pixel localisation of passive micro-coil fiducial markers in interventional MRI," *MAGMA Magn Reson Mater Phys Biol Med*, vol. 13, no. 3, pp.379 -382, 2008.

[21] S. Alt, A. Homagk, R. Umathum, W. Semmler, and M. Bock, "Active microcoil tracking in the lungs using a semisolid rubber as signal source," *Magnetic Resonance in Medicine*, vol. 64, no. 1, pp. 271-279, 2010.

[22] C. Flask, D. Elgort, E. Wong, A. Shankaranarayanan, J. Lewin, M. Wendt, and J. L. Duerk, "A method for fast 3d tracking using tuned fiducial markers and a limited projection reconstruction fisp (LPRFISP) sequence," *Journal of Magnetic Resonance Imaging*, vol. 14, no. 5, pp. 617–627, 2001.

[23] C.M. Hillenbrand, D.R. Elgort, E.Y. Wong, A. Reykowski, F.K. Wacker, J.S. Lewin, and J.L. Duerk. "Active device tracking and high-resolution intravascular MRI using a novel catheter-based, opposed-solenoid phased array coil," *Magn Reson Med*, vol. 51, pp. 668–675, 2004.

[24] R.C. Susil, J.H. Anderson, and R.H. Taylor, "A single image registration method for CT-Guided Interventions," *Proceedings of the second international conference on Medical Image Computing and Computer-Assisted Intervention, Cambridge, UK, 1999: lecture notes in computer science, New York, Springer*, vol. 1679, pp. 798–808, 1999.

[25] S. DiMaio, E. Samset, G.S. Fischer , I Iordachita, G Fichtinger, F Jolesz, and C Tempany, "Dynamic MRI Scan Plane Control for Passive Tracking of Instruments and Devices" *MICCAI, LNCS*, vol. 4792, pp. 50–58, 2007.

[26] A. Lang, D. Stanton, V. Parthasarathy, and A. Jain, "Fast and accurate calibration of an X-ray imager to an electromagnetic tracking system for interventional cardiac procedures," *Proc 33rd Annu Int Conf IEEE Eng Med Biol Soc*, pp.1868 -1873, 2010.

[27] A. Patriciu, D. Petrisor, M. Muntener, D. Mazilu, M. Schär, and D. Stoianovici, "Automatic brachytherapy seed placement under MRI guidance," *IEEE Trans Biomed Eng*, vol. 54, pp. 1499–1506, 2007.

[28] A. K. Jain, T. Mustafa, Y. Zhou, C. Burdette, G.S. Chirikjian, and G. Fichtinger, "FTRACA-robust fluoroscope tracking fiducial," *Med Phys*, vol. 32, pp. 3185-3198, 2005.

[29] F. G. Shellock, "Magnetic resonance safety updates 2002: implants and devices." *J Magn Reson Imaging*, vol. 16, no. 5, pp. 485-496, Nov 2002.

[30] "Standard Test Method for Measurement of Magnetically Induced Displacement Force on Passive Implants in the Magnetic Resonance Environment, F2052," *American Society for Testing and Materials (ASTM)*, vol. 13.01, 2002.

[31] N. E. M. Association, "Determination of signal-to-noise ratio (snr) in diagnostic magnetic resonance imaging," *NEMA Standards Publication MS*, pp. 1–2008, 2008.

[32] N. Tsekos, A. Khanicheh, E. Christoforou, and C. Mavroidis, "Magnetic Resonace-Compatible Robotic and Mechatronics System for Image-Guided Interventions and rehabilitation: A review study," *Annual review of Biomedical Engineering in Medicine and Biology*, vol. 3, pp. 15-22, 2008

[33] http://www.mr-klinikkenskoerping.dk/00088/

[34] J. Tokuda, G. S. Fischer, X. Papademetris, Z. Yaniv, L. Ibanez, P. Cheng, H. Liu, J. Blevins, J. Arata, A. J. Golby, T. Kapur, S. Pieper, E. C. Burdette, G. Fichtinger, C. M. Tempany, and N. Hata, "OpenIGTLink: an open network protocol for image-guided therapy environment," *Int J Med Robot*, vol. 5, no. 4, pp423-34, 2009.

[35] J. Egger, J. Tokuda, L. Chauvin, B. Freisleben, C. Nimsky, T. Kapur, and W. Wells, "Integration of the OpenIGTLink Network Protocol for image-guided therapy with the medical platform," *Int J Med Robot*, vol. 8, no. 4, pp. 282-290, 2012.

[36] Y. Ma, I. Dobrev, W. Shang, H. Su, S. Janga, and G. S. Fischer, “CHIC: Cylindrical Helix Imaging Coordinate Registration Fiducial for MRI-Guided Interventions,” *EMBC, San Diego, USA*, pp. 2808-2812, 2012.

[37] R.C. Susil, , J.H. Anderson, and R.H. Taylor, “A Single Image Registration Method for CT Guided Interventions,” *MICCAI 1999, Cambridge, England, LNCS 1679*, 798-808, 1999.

[38] J. Mireles, A. Adame, D. Espalin, F. Medina, R. Winker, T. Hoppe, B. Zinniel, and R. Wicker, “Analysis of Sealing Methods for FDM-fabricated Parts,” *University Of TEXAS-El PASO*, August 17, 2011.

[39] W. Ji, J.D. Matte, G. Li, Y. Ma, H. Su, W. Shang, G.S. Fischer, “Reconfigurable Fiducial-Integrated Modular Needle Driver for MRI-Guided Percutaneous Interventions,” *Design of Medical Devices Conferences (DMD), Minneapolis, MN*, April 2013.

[40] N. Otsu, “A threshold selection method from gray-level histograms,” *Automatica*, vol. 11, no. 285-296, pp. 23–27, 1975.

[41] W. Shang and G. S. Fischer, “A high accuracy multi-image registration method for tracking MRI-guided robots,” *SPIE Medical Imaging, ,* vol. 8316, pp. 83 161V–1, 2012.

[42] M. Li, A. Kapoor, D. Mazilu, and K. A. Horvath, “Pneumatic actuated robotic assistant system for aortic valve replacement under MRI guidance,” *Biomedical Engineering, IEEE Transactions*, vol. 58, no. 2, pp. 443–451, 2011.

[43] G.A. Coutts, D.J. Gilderdale, M. Chui, L. Kasuboski, N.M. DeSouza, “Integrated and interactive position tracking and imaging of interventional tools and internal devices using small fiducial receiver coils,” *Magn Reson Med*, vol. 40, no. 6, pp. 908–913, 1998.
[44] M. Burl, G. Coutts, I.R. Young, “Tuned fiducialmarkers to identify body locations with minimal perturbation of tissue magnetization,” *Magn Reson Med*, vol. 36, pp. 491–493, 1996.

[45] M. ARea, D.W. McRobbie, H. Elhawary, Z.T. Tse, M. Lampérth, I. Young, “A system for 3D real-time tracking of MRI-compatible devices by image processing,” *ASME-IEEE T Mech*, vol. 13, no. 3, pp. 379–382, 2008.

[46] M. Mahvash, V. Hayward, “Measurement and characterization of soft tissue behavior with surface deformation and force response under large deformations,” *Med Image Anal*, vol. 14, no. 2, pp. 138-148, Apr 2010.

[47] C. Cohade, M. Osman,Y. Nakamoto, L.T. Marshall, J.M. Links, E.K. Fishman, and R.L. Wahl, “Initial experience with oral contrast in PET/CT: phantom and clinical studies,” *J Nucl Med*, vol. 44, pp. 412-416, 2003.

[48] A.A. Moss, H.Y. Kressel, M. Korobkin, H.I. Goldberg, B.M. Rohlfing, R.C. Brasch, “The effect of gastrografin and glucagon on CT scanning of the pancreas: a blind control trial,” *Radiology*, vol. 126, pp. 711–714, 1979.

[49] J.M. Criscione, L.W. Dobrucki, Z.W. Zhuang, X. Papademetris, M. Simons, A.J. Sinusas, T.M. Fahmy, “Development and application of a multimodal contrast agent for SPECT/CT hybrid imaging,” *Bioconjug Chem*, vol. 22, no. 9, pp. 1784-1792, 2011

Curriculum Vita

Yunzhao Ma was born on Oct. 7, 1988 in Kunming, Yunnan, China. He went to high school at No.1 High School of Kunming where he graduated in 2007. Then he received his B.S. degree in Biomedical engineering from Southeast University in Nanjing, China in 2011. He began Biomedical Engineering graduate studies at Worcester Polytechnic Institute in 2011. Since 2012, he has been a graduate research assistant at WPI Automation and Interventional Medicine (AIM) Robotics Research Laboratory. His research interests include registration techniques, image fiducial design and MRI-guided interventions robot.

Publications:

[1] W. Ji, J.D. Matte, G. Li, Y. Ma, H. Su, W. Shang, G.S. Fischer, "Reconfigurable Fiducial-Integrated Modular Needle Driver for MRI-Guided Percutaneous Interventions," *Design of Medical Devices Conferences (DMD), Minneapolis*, MN, Feb. 2013.

[2] Y. Ma, W. Shang, I, Dobrev, H. Su, G.S. Fischer, "Cylindrical Helix Imaging Coordinate Fiducial Registration and Tracking Assistant System for MRI-guided Minimally Invasive Surgical Robots," *IEEE Transactions on Biomedical Engineering (TBME)*, 2013. (In review)

[3] Y. Ma, I. Dobrev, W. Shang, H. Su, S. Janga, G.S. Fischer, "CHIC: Cylindrical Helix Imaging Coordinate Registration Fiducial for MRI-Guided Interventions," *34th Annual International Conference of the IEEE Engineering in Medicine and Biology Society (EMBC)*, San Diego, USA, Aug. 2012.